Heat pumps and latent thermal energy storages at residential heating temperature levels:
A thermodynamic investigation combining theory and experiment for separate and combined systems

Von der Fakultät für Ingenieurwissenschaften,

Abteilung Maschinenbau und Verfahrenstechnik der

Universität Duisburg-Essen

zur Erlangung des akademischen Grades

eines

Doktors der Ingenieurwissenschaften

Dr.-Ing.

genehmigte Dissertation

von

Julian Quenel

aus

Duisburg

Gutachter:

Univ.-Prof. Dr. rer. nat. Burak Atakan, Universität Duisburg-Essen

Univ.-Prof. Dr. Ing. Stephan Kabelac, Leibniz Universität Hannover

Tag der mündlichen Prüfung: 07.06.2024

DuEPublico

Duisburg-Essen Publications online

Acknowledgments

At this point, I would like to thank everyone without whom this work would not have been possible. Even before starting this doctoral study in 2019, I had the opportunity to hear a lot of lectures and write my master thesis at this chair, thus getting deeper into the topic of thermal energy storage and thermodynamic in general. Subsequently, I was given the chance to start this study. For this, I want to thank *Prof. Burak Atakan*. You have not only been a symbol of thermodynamics throughout my entire academic career but also believed in my ability to achieve this graduation. Especially during the difficult phases, you provided me with advice and structuring thoughts. This is not something to be taken for granted in my opinion.

I also want to thank *Prof. Stephan Kabelac*. You authored "Thermodynamik: Grundlagen und technische Anwendungen" which accompanied and impressed me during my whole study time, and now you are the second examiner of my dissertation. I could never have imagined this back then.

I appreciate the support from my colleagues at the chair as well. To permanents like *Ulf Bergmann* for constant assistance in teaching and many laughs, *Stephan Steinbrink* for frequent support in the lab and profound conversations, *Andreas Görnt* for ongoing assistance with everything around, and *Lisa Meiers* for the much-needed support and clarification in bureaucratic matters, no matter how self-explanatory they were.

But also, from those who joined with the same goal: *Charlotte Rudolph, Michael Aps, Dennis Kaczmarek, Alexandra Welp, Christoph Horn, Sascha Lau, Dominik Freund, Yasin Karakaya, Sebastian Grimm, Niklas Tomasik, Simon Schmeing, Ilyas Adaköy, Dennis Roskosch, Valerius Venzik* and *Peter Oketch*. Through you, this time became something special. Professional discussions, discussions about everything *except* the professional, and a lot of fun were always guaranteed. Whether in the less frequently visited Carnot room or elsewhere. Without some of these conversations, I might have lost sight of the path and eventually stopped.

I would also like to express special thanks to my family, especially my wife *Alina Quenel*. Without you going with me through all good and bad times, withstanding challenging phases, frequently relieving me of work, discussing very professional matters with me, or staying up with me in solidarity until late at night when there was much to do, this would simply not have been possible. Thank you very much.

Don't believe in yourself. Believe in ME who believes in you!

Thanks to all of you.

Kurzfassung

Durch den immer weiter ansteigenden Anteil an erneuerbaren Energien am Strommix, stellt ein Wechsel auf vollelektrische Heizmethoden, wie die Wärmepumpe, eine Möglichkeit dar die CO_2-Emissionen im Gebäudesektor zu reduzieren. Für Bestandsbauten liegt der Anteil der Wärmepumpen jedoch, durch Vorbehalte bezüglich des Einsatzes bei geringen Außentemperaturen oder ohne Fußbodenheizung und weitreichende bauliche Investitionen, noch im Bereich weniger Prozent.

Diese Arbeit verfolgt deshalb das Ziel dazu beizutragen, solche bestehenden Bedenken auszuräumen. Mit experimentellen Untersuchungen soll ein tieferes Verständnis über die Zusammenhänge von sowohl internen als auch externen Einflüssen auf die Wärmepumpe bei diesen Temperaturniveaus erreicht und so ein Beitrag zum aktuellen Forschungsstand geleistet werden. Diese Experimente wurden an einer Kompressions-Wärmepumpe mit Temperaturen der Wärmesenke von bis zu 75 °C im Bereich von Gebäudeheizungen in Bestandbauten durchgeführt. Interne Einflüsse wurden durch die Variation eines Isobutan/Propan Gemisches als Kältemittel und externe Einflüsse durch die Änderung des Wärmebedarfs als auch die Variation der Temperatur der Wärmequelle betrachtet.

In Kombination mit Wärmepumpen können latente thermische Speicher verwendet werden, deren eingeschränkte Wärmeübertragung durch verschiedene Methoden, wie Rippen oder höhere treibende Temperaturgradienten, ausgeglichen werden. Die Einordnung, ob der so zunehmende Wärmestrom proportional zu den Parameterveränderungen der Methoden steht, ist ein weiteres Ziel dieser Arbeit. Dazu wird, simulativ als auch experimentell, die Be- und Entladung eines Speichers mit Paraffin als Speichermaterial untersucht und mit der dimensionslosen Wärmestromdichte eine neue Kenngröße für die angestrebte Einordnung eingeführt. Zuletzt werden anhand der Messdaten grundlegende Überlegungen präsentiert, wann der Einsatz eines thermischen Speichers energetisch vorteilhafter als eine notwendige Anpassung der Heizleistung der Wärmepumpe an den Wärmebedarf ist.

Durch die Analysen zeigt sich, dass der Einfluss von zeotropen Kältemittelgemischen auch für höhere Temperaturniveaus in der Praxis geringer als in der Theorie ist. Ungefähr 5 % höhere Leistungszahlen konnten im Vergleich zum reinen Kältemittel beobachtet werden, wobei mit zunehmendem Temperaturniveau die Steigerungen geringer ausfielen. Der Verdichter stellte die wichtigste Komponente des Prozesses mit den höchsten Exergieverlusten dar, dessen Betriebsverhalten andere Einflüsse auf den Prozess überlagert. Aus diesem Grund

wurde nur bei einer Änderung der Betriebsparameter des Verdichters ein Einfluss der Sekundärfluidparameter auf die Leistungszahl beobachtet.

Bei der Untersuchung des latenten thermischen Speichers nahm der steigernde Effekt auf die Wärmestromdichte mit zunehmenden Parametern der Verbesserungsmethoden für die Wärmeübertragung ab. Die Entladung des Speichers bei einem hohen Temperaturniveau stellte eine Ausnahme dar, hier waren höhere treibende Temperaturgradienten vorteilhaft. Für die Kombination von Wärmepumpe und thermischen Speicher ergab sich, dass der auf den Speicher übertragene Wärmestrom schon bei den nicht optimierten Laboranlagen höher als die reduzierte elektrische Leistung des Verdichters für die Anpassung an den geringeren Wärmebedarf ist.

Insgesamt zeigt sich so, dass der Einsatz von Wärmepumpen auf dem Temperaturniveau eines Heizungssystems in Bestandsgebäuden möglich ist und, mit Hilfe des Verständnisses der Einflüsse auf den Prozess oder Optimierungen wie die Kopplung mit thermischen Speichern, die Effizienz eines solchen Systems gesteigert werden kann.

Abstract

Due to the constantly increasing proportion of renewable energies in the electricity mix, switching to all-electric heating methods, such as heat pumps, represents an opportunity to reduce CO_2-emissions in the building sector. For existing buildings, the proportion of heat pumps is still in the range of a few per cent due to reservations regarding their use at low outside temperatures or without floor heating and extensive structural investments.

Therefore, this work aims to contribute overcoming such concerns. Experimental investigations are performed to achieve a deeper understanding of the relationships between both internal and external influences on the heat pump at these temperature levels and thus contribute to the current state of research. These experiments were carried out on a compression heat pump with heat sink temperatures of up to 75 °C, thus in the range of heating systems in existing buildings. Internal influences were considered through the variation of an isobutane/propane mixture as a working fluid and external influences through the change in heat demand as well as the variation of the temperature of the heat source.

In combination with heat pumps, latent thermal stores can be used whose limited heat transfer is compensated for by various methods, such as fins or increasing driving temperature gradients. Another aim of this work is to evaluate whether the increasing heat flux is proportional to the parameter changes of the methods. For this purpose, the charging and discharging of a storage with paraffin as the storage material is investigated both simulatively and experimentally and a new parameter for the intended evaluation is introduced with the dimensionless heat flux. Finally, based on the measurement data, fundamental considerations are presented when the use of a thermal store is more advantageous from an energy point of view than a necessary adjustment of the heat pump process to the heat demand.

The analyses show that the influence of zeotropic working fluid mixtures is lower in practice than in theory, even at higher temperature levels. Approximately 5 % higher *COP*s were observed compared to the pure fluid, whereby the increases were decreasing with raising temperature levels. The compressor was the most important component of the process with the highest exergy destruction, and its operating behaviour superimposes other influences on the process. For this reason, an effect of the secondary fluid parameters on the *COP* was only observed when the operating parameters of the compressor were changed.

In the investigation of the latent thermal store, the increasing effect on the heat flux decreased with increasing parameters of the improvement methods for heat transfer.

Discharging the storage at a high temperature level was an exception; here, higher driving temperature gradients were favourable. For the combination of heat pump and thermal storage, it was found that even in the non-optimized laboratory systems the heat flow rate transferred to the storage was higher than the reduced electrical power of the compressor for adaptation to the lower heat demand.

Overall, this shows that the use of heat pumps at the temperature level of a heating system in existing buildings is possible and that the efficiency of such a system can be increased by understanding the influences on the process or through optimisations such as coupling with thermal storages.

Table of contents

CHAPTER 1

CHAPTER 2

CHAPTER 3

List of figures

Chapter 4

Chapter 5

List of tables

Chapter 1

Introduction

The issues associated with climate change pose increasingly significant challenges, accelerating substantial engagement from the research community in this field over the last decades. But, beyond academia, the topic has also never been more prevalent within the whole society than these days. There are numerous reports, documentaries, and demonstrations [1–6] generating awareness and consequently leading to political action. Recent examples in Germany and the EU would be the German government's climate protection plan up to 2050 [7], the building energy act [8], the EU strategy on adaptation to climate change [9], and the law on the restoration of nature [10]. The building sector often occupies a central position in the perception of society and reports due to the everydayness to everyone, but overall, it also constitutes a considerable portion of the total CO_2-emissions. For instance, 15 % of the 760 million tons of CO_2-equivalents in Germany in 2021 were attributed to the building sector [11].

A widely adopted approach to reduce these emissions is to switch to full electric house heating methods, as the global aim is to provide electricity from renewable energy sources in a climate-neutral manner. Among these methods, the air-to-water heat pump is the most well-known, with its usage quickly gaining more and more significance in new buildings in recent years. In 2022, the share of heat pumps in new constructions was 57 %, compared to only 31.4 % in 2015 [12]. In contrast, their usage in existing buildings is significantly lower, with a share of only 3 % compared to a 50 % share of gas heating systems in 2022 [13]. One reason for this difference are the necessary investment costs to switch to a new heating system. Additionally, concerns towards the use of heat pumps in existing buildings persists among the press and the general public [14–16]. Frequently, comparisons are drawn with gas heating systems, which have lower investment costs and often are believed to be cheaper than heat pumps in operation due to current electricity prices being higher than those of gas (per kWh) [17]. Moreover, the required temperature level for heating systems without floor heating is seen critically and operation without major modifications (like insulating the whole house) is considered as unfeasible.

However, many scientific studies come to the opposite conclusion. While there are still difficulties and uncertainties to be researched, fundamentally, they agree that heat pumps represent a pathway to heat transition [18–25] due to efficiencies high enough that the overall

operation costs are already lower than for conventional systems. Despite that the cost savings over time highly depend on the specific system, experienced companies in that business field expect the amortization time for old unrenovated houses to be around 10 to 15 years [26,27]. Thus, higher expected efficiencies would lead to even more reduced operating costs and amortization times. This, alongside the benefits for the environment and climate, would create a broader incentive for transitioning to a heat pump system.

For this reason, it is crucial to further intensify the research on heat pumps at this residential temperature level, to enhance understanding, anticipate influences better, and achieve optimizations in performance. Through investigations on a compression heat pump at laboratory scale, the present work contributes to gain these necessary insights.

Heat pumps at residential temperature level

One of the key aspects for the wider adoption of heat pumps in existing buildings is to disprove the bias that heat pumps would not be usable at higher temperatures and without floor heating due to low efficiencies. Typical inlet temperatures for older heating systems reach up to 70 °C, while the return temperature often is 10 to 15 °C lower. Potential heat sources in this context may include the ground with a nearly constant temperature of 7 °C (at a depth of 2 meters) or the ambient air, which is subject to greater fluctuations. These temperatures for the heat demand and source represent the necessary temperature lift of the process. Thus, compared to floor heating systems that operate at around 35 °C, utilizing the same heat sources results in a higher temperature lift for older heating systems. This results in a decreasing coefficient of performance (*COP*) of the heat pump, that is the ratio between the electrical power input and the heat flow rate output. However, this does not necessarily imply that economic operation is unfeasible, because if an annual *COP* of at least 3 is achieved, the heat pump heating system is generally considered as economically viable. For the floor heating, these *COP* values are easily achievable due to the low temperature lift; however, sufficient studies demonstrate that such efficiencies are also feasible for higher temperature levels [28–34]. Nonetheless, there remains a need for further research in this area, as various reviews indicate [28,31,35]. Particularly, experimental work is important for testing and comparing simplified theoretical considerations in practical applications.

An example for this are zeotropic working fluid mixtures of hydrocarbons, that are frequently investigated, as indicated by review articles [35–38]. In those heat pumps with zeotropic working fluid occurs a temperature glide in the heat exchangers due to the different

vapour pressures of the working fluids. Therefore, the composition of the vapour and liquid phase vary during the heat transfer, which results in a non-isothermal phase change. Thus, a better match between the temperature changes of the working fluid and secondary fluid in the heat exchangers can be achieved. This leads to lower temperature differences between both fluids. Consequently, exergy losses decrease and result in efficiency improvements [39–43], whereby exergy represents the share of energy that could perform useful work and is strongly dependent on the temperature level. However, it is observed that in practice the *COP* enhancements are lower than expected from theory for lower temperature levels [39,40,44]. Here, this circumstance was primarily contributed to the compressor that superimposed the benefit of the temperature glide in the heat exchangers, leading to the conclusion that it is a key component. Overall, there are still open research questions regarding the higher temperature level that must be addressed; for example, how the zeotropic mixtures or the changing heat demand and source affect the compressor, the *COP* and the process itself.

Apart from this, two operation methods for heat pumps in heating systems are currently focused. Firstly, the On-Off method [45–49], in which the compressor operates at a fixed speed and the system is turned on and off to adapt to the heat demand. This On-Off operation, also referred to as cycling, results in energy losses and inefficiencies due to frequent starts and shutdowns of the system which, for example, lead to working fluid migration and equalization of the pressures within the system [45,46]. Secondly, the modulating method [34,50–53], where the compressor speed and thus the thermal output is varied. Some studies also compare these two methods [33,54,55], concluding that there is no clear favourite between these two methods and it depends on the conditions whether the one or the other is favourable. However, the operating time of an On-Off system correlates with the performance over the year [48]. Overall, an adequate sizing and longer run times are advantageous for On-Off Operations, as well as less regulation for modulating systems with variable compressor speeds. An approach to increase the performance of the system in these ways is the combination of the heat pump with a thermal storage system that could be charged when the heat demand is low.

Heat pumps with thermal energy storages

Many studies prove that thermal energy storages can increase the performance of house heating systems when they are combined with a heat pump [23,56–60]. In practice, buffer storages like water tanks indeed are commonly used but too often they are not optimized for the application. They are frequently oversized, not specifically designed for the heating system or only water is

considered as storage material. Nevertheless, instead of those sensible energy storages, latent ones are an option for heat pumps as reviews show [23,57,61]. By using the high phase transition enthalpy of phase change materials (PCMs) like paraffins, latent storages offer the advantages of high energy densities and a roughly isothermal operation near the phase change temperature of the PCM. This can lead to e.g. space savings compared to sensible ones, which can be economically attractive in regions and applications where space is expensive [23]. However, an issue with most PCMs is their low thermal conductivity, resulting in lower heat transfer and reduced practical applicability.

To overcome this disadvantage, several research investigate the performance enhancement of such latent storage systems [62–65]. These include the use of fins in the storage system [66–70], addition of highly thermally conductive material into the PCM [71–75], composites [76–80], or encapsulation of the PCM [81–85]. However, such improvement methods may entail drawbacks, for example, reduced storage capacity due to occupied volume from fins or exergy losses from lower discharge temperatures. Overall, there is a trade-off between this and the increasing performance to make certain processes feasible or economical, which implies the question whether the increase is proportional or not. This is particularly important for the combination of a heat pump with a thermal storage, as it has a lot of dependencies and dynamics, and thus potential for optimization.

All in all, it becomes evident that heat pumps, thermal storage systems, as well as their combination, require further experimental investigation at residential temperature levels. Thus, the studies need to get closer to practical applications, thereby recognizing as well as utilizing optimization potential more effectively, to increase the distribution of full electric space heating in existing buildings and accelerate the decarbonization of the building sector.

Aim and motivation of this work

The present cumulative thesis aims to address the challenges of operating heat pumps at the higher temperature level of residential heating systems and to support the understanding of the influences on heat pump systems in this use case by analysing experimental data from a lab-scale test system. Furthermore, latent thermal energy storage systems are investigated here in simulations and experiments to contribute to the clarification of their advantages and limitations, whether standing alone or by combining them with heat pumps.

To achieve this, a compression heat pump, previously examined at lower condenser temperatures for floor heating around 35 °C [40], got modified and was operated at higher

temperatures up to 75 °C. Building upon this prior work and the literature review, the hydrocarbons isobutane and propane were selected, as their zeotropic working fluid mixture had previously demonstrated improvements in *COP* due to temperature glide effects. Thus, their influence is investigated here at the higher temperature level by varying the mixture composition to identify the primary factors and components. To consider external influences on the heat pump occurring in practical scenarios, e.g. fluctuating temperatures of the heat source and the heat demand of the heating system, variations of the secondary fluid parameters are applied to the test setup.

For the combination of thermal energy storage and heat pumps, it is important to examine the limited and time-dependent heat transfer of latent storages. Here, investigations were performed for a latent thermal energy storage considering fins, increasing thermal conductivity of the PCM, or raising the driving temperature gradient as heat transfer enhancement methods. To explore the trade-off for an increasing use of these methods, the influence on the heat flux is quantified and subsequently discussed regarding the proportionality of the increase. For this purpose, paraffins with melting points of 44, 47 and 60 °C as PCM are examined in simulations and experiments to consider different temperature levels of thermal energy storages in heating systems. For most applications, higher temperature levels are preferred as the stored energy here is more valuable in practical and exergetic terms. Therefore, the combination of the heat pump and latent thermal storage is exemplarily discussed for experimental data at 60 °C to investigate whether adjusting the heat pump load or charging the storage with resulting excess energy at full load is energetically more valuable for a decreasing heat demand.

In conclusion, the investigated research questions of this thesis can be summarized as follows:

Research questions for the heat pump:

1) Can previous insights and *COP* improvements for varying zeotropic working fluid mixtures from around 35 °C be observed at higher temperature levels up to 75 °C? How are the components affected by the zeotropic mixture at those higher temperatures?

2) What impact does the variation of external influences from secondary fluid parameters have on the process at the higher temperature level? Which parameters of the process are mainly affected by higher temperature levels and how do they change the performance?

Research questions for the latent thermal energy storage:

3) How does the heat flux decrease within the operation time and increase for different heat transfer enhancement methods? Is this improved heat flux proportional to the parameter change of those methods?

4) Does this apply to the experiment and at different temperature levels?

Research questions for the combined system of heat pump and storage:

5) When is it energetically more valuable to charge an energy storage with excess energy than to adjust the heat pump load to a decreasing heat demand?

These questions will be addressed in the following chapters, corresponding to publications in peer-reviewed journals for chapters 2 to 4. Chapter 2 investigates research question 1 experimentally by varying the working fluid mixture of isobutane and propane for condenser temperatures of 40 and 60 °C to examine the influence of the mixture composition on the process.

Research question 2 is discussed in chapter 3, wherein the best performing working fluid composition from chapter 2 is used to determine the effects from changing external influences by varying the heat demand and heat source temperature of the secondary fluid.

Chapter 4 examines research question 3 by performing a simulation-based investigation of the time-dependent discharge heat flux for different fins, PCM thermal conductivities and driving temperature gradients, introducing a dimensionless parameter to characterize the proportionality of the increased heat flux.

Finally, chapter 5 presents an investigation of research questions 4 and 5, wherein a latent storage with the dimensions of the modelled system in chapter 4 is used to examine PCMs with melting points of 47 and 60 °C. Thus, the simulation results are validated and experiments at both temperature levels are compared. For research question 5, exemplary experimental data is discussed whether the combination of the used test systems is energetically valuable despite that they are non-optimized.

Note

To make this thesis more consistent, the following studies, published in various journals, have been slightly adjusted in the overall formatting as well as the numbering of the figures, tables and equations. Additionally, small changes have been made at a few passages or figures for correction purposes which are indicated with footnotes.

Chapter 2

Propane-isobutane mixtures in heat pumps with higher temperature lift: an experimental investigation

The content of this chapter was published in [86]:

J. Quenel, M. Anders and B. Atakan. Propane-isobutane mixtures in heat pumps with higher temperature lift: an experimental investigation. *Thermal Science and Engineering Progress Volume 42, 101907, (2023).* DOI: *10.1016/j.tsep.2023.101907*.

Table 2.1 Author contributions for the paper following the CRediT author statement methodology [87].

Category	Quenel	Anders	Atakan
Conceptualization	X		X
Methodology	X	X	
Software	X	X	
Validation	X	X	
Formal analysis	X	X	
Investigation	X	X	
Resources			X
Data Curation	X	X	
Writing - Original Draft	X		
Writing - Review & Editing	X		X
Visualization	X		
Supervision	X		X
Project administration			X
Funding acquisition			X

Author contributions to this paper

The experiments that provided the data for this paper were carried out by Maurits Anders as a part of his master thesis. My contribution was to help supervising the thesis and analysing the results used for the paper. Further, I did the visualization and wrote the manuscript. Burak Atakan supervised the thesis and reviewed the manuscript.

Introduction and key results of the first paper

Within the aim to investigate heat pump processes at the higher temperature levels, there is a high demand of experimental data as reviews like Ostermann et al. observed [23]. Especially for zeotropic mixtures should be more investigations done [36] and also other reviews, for example Bamigbetan et al. [37], reported challenges of the compressor with hydrocarbons at higher temperatures. A previous thesis [40] at the chair examined these challenges at the temperature level of floor heating for zeotropic mixtures and provided experimental data. Consequently, this system can be used well to transfer investigations to higher temperatures by considering the influence of a hydrocarbon mixture on the process and the compressor operation behaviour.

For this purpose, the work uses the mentioned compression heat pump and operated it at the targeted higher heat sink temperature level up to 70 °C. Isobutane and propane were used here in varying mole fractions, because they showed a good performance in other studies [35]. Thus, the influence of the composition on the performance of the process is evaluated, considering the different components and how they are affected. This is achieved through an exergy analysis for all components and the in-depth analysis of the compressor operation behaviour.

Overall, some contributions of this work to the mentioned challenges can be shortly summarized as follows:

- Experimental data for zeotropic working fluids is provided with varying isobutane/propane mixtures for secondary fluid condenser outlet temperatures of 50 and 70 °C (a temperature lift of 33 and 53 °C between heat source and sink).
- The *COP* for higher temperature lift was around 2 and depends on the isobutane mole fraction and working fluid evaporator inlet temperature.
- Like in previous work, the compressor was the most influencing component of the process with the highest contribution to the total exergy destruction.
- For a reduced compressor speed, an increasing *COP* is observed for the lower temperature lift and a decreasing one for the higher lift, due to changing compressor efficiencies.
- The maximum *COP* was found for an isobutane mole fraction of 0.267, despite the highest temperature glide occurred for a mole fraction of 0.527.
- The electro-mechanical compressor efficiency was the most influential, strongly affected by the pressure ratio and causing the before mentioned *COP* observations.

2.1   Abstract

The shift towards renewable energies leads to an increased interest in heat pumps, not only for floor heating at temperatures around 40 °C, but also for providing hot water at higher temperatures (> 60 °C). To reach the goal of a climate neutral process, it is important to use working fluids with low global warming potential (GWP). Zeotropic mixtures are discussed to potentially increase the coefficient of performance (*COP*) of a heat pump compared to pure fluids. The present work experimentally analyses a compression heat pump process of such fluids; five mixtures of propane (R290) and isobutane (R600a) are investigated here. The influence of composition, compressor frequency, inlet temperature of the working fluid into the evaporator and the inlet temperature of the secondary fluid water into the condenser are researched. Besides the *COP*, the destroyed exergy in the components are evaluated, to find the most relevant losses. It is shown that the *COP* for a temperature lift of 33 K are above 3 for the mixtures, while at a higher temperature lift of 53 K the *COP* is around 2. Furthermore, a strong impact of the compressor efficiency on the process was found. The results show that the advantage of the zeotropic mixture within the heat exchangers is limited by their low contribution to the total specific exergy destruction compared to the compressor. The compressor efficiency changes with the composition, due to composition dependant pressure and density variations. The often-neglected changes in electro-mechanical losses get important, when the pressure ratios are changing with composition, as shown experimentally.

2.2   Introduction

Heat pumps gain more and more in importance, due to their efficiency and possibility to be driven by , because the world energy increasingly stems from renewable sources. At the same time, fluorocarbons have to be replaced as working fluids, due to their global warming potential (GWP) [88]. Natural refrigerants like hydrocarbons are an option to replace them and were investigated within several cycles [35,89–92], due to their low GWP and their good accessibility. Further, zeotropic refrigerant mixtures are a good way to achieve lower exergetic losses in heat exchangers when sensible heat sources and sinks are used, because the temperature difference between the working fluid and the secondary fluid throughout the heat exchange is reduced. While heat pumps are mainly used for low temperature lifts, the interest in higher temperature heat pumps (HTHP) rises [28,89,91,93,94], which provide secondary fluid exit temperatures of 50 °C to 100 °C using heat sources around 5 – 20 °C. Possible

applications for HTHPs are the warm water distribution with a needed temperature of around 60 °C or conventional house heating systems with entering heat flows at 50 to 70 °C; they could replace natural gas heaters. High exergetic efficiencies and low CO_2 emissions can be reached, if the electrical energy is provided from renewables. In the field of water heating, Zhang et al. [95] evaluated the *COP* of a process depending on the pipe length of the heat exchangers and the refrigerant amount. They used ambient air as the heat source and R22 as the refrigerant. The temperature of the secondary fluid was increased to 55 °C and the *COP* strongly depended on the temperature of the ambient air and the charge of the system.

Chaichana et al. [96] compared the hydrocarbons propane, propene, isobutane, and n-butane as refrigerants for a solar-powered heat pump for the provision of hot water, varying the temperatures of evaporation and condensation. The mass flow rates, operating pressures, compressor inlet temperatures and *COP* were compared. Propane and propene showed good performance in their study for condensing temperatures of up to 70 °C.

Chang et al. [97] also compared the pure fluids isobutane, n-butane, propane and propene. They considered the zeotropic mixtures of isobutane/propane and n-butane/propane. The substances were compared in a test plant at low secondary fluid temperatures of 21.1 °C in the condenser and 8.3 °C in the evaporator. The mixture isobutane/propane (mass ratio 50/50) led to a 7 % higher coefficient of performance compared to the reference case with R22. The mixture of n-butane/propane (mass ratio 75/25) increased the *COP* by about 11 %.

Park et al. [98] investigated propane and propene as pure refrigerants as well as the mixture of these two substances, also as an alternative to R22. In addition, a ternary mixture of propane/propene/DME was measured. They found an increase in the *COP* compared to R22 for all used refrigerant except for pure propene, with the ternary mixture showing the highest increase of 5.7 %.

Bamigbetan et al. [29] investigated a cascade heat pump that can provide energy at 115 °C using residual heat. This cascade heat pump with a heating capacity of 20 kW was operated with propane and butane. They concluded that this system with an average *COP* of 3.1 in the temperature range of 58 to 72 °C is the better alternative to electrical heaters or gas boilers.

There are also several theoretical studies available, investigating zeotropic mixtures in heat pumps. For example, Guo et al. [94] evaluated recuperative high-temperature heat pump cycles with subcritical zeotropic mixtures. The performance analysis for hot water supply from 15 °C to 99 °C with an air heat source was investigated for fluids like hexane, R431 0mee,

propane, propene and R32 as refrigerant and studied the effect of pressures and mixture compositions on cycle *COP* and exergy utilisation. Higher *COP*s of 5.063 and 5.011 were reached for n-hexane/propene and R431 0mee/R32 with a reduction of exergy destruction due to a good temperature match between working fluid and heat sink. Also, the results were compared to CO_2 heat pump cycles and showed an increase in *COP* by up to 8.88 % with operation pressures below 2 MPa.

Mota-Babiloni et al. [99] simulated and optimised high-temperature heat pump cascades with internal heat exchangers. They used low GWP working fluids like pentane, isobutane, propane, HCFO-1233zd(E), HCFO-1224yd(Z) and HFO-1336mzz(Z) as working fluids and optimised the *COP* of the cascade with an algorithm. They found the maximum *COP* of 3.15 for pentane/butane mixtures. An option with low flammability was a cascade with HFO-1366mzz(Z)/HFO-1234ze(E) which showed a good performance. In this study the low stage internal heat exchanger had a low impact on the high stage discharge temperature.

Zühlsdorf et al. [100] investigated the increase of the performance of a booster heat pump that heats a district heating water stream from 40 °C to 60 °C. They screened 18 possible fluids like propane, pentane, propylene, isobutane or R1234yf and considered the pure fluids as well as the possible mixtures of them. The mixture with 50 % isobutane and 50 % pentane showed the best performance with an *COP* of 9.01. By analysing the complete system of low temperature district heating, they found the overall system *COP* increasing from 13 % to 22 % when using working fluid mixtures in the central and booster heat pump units.

In a further study, Zühlsdorf et al. [41] demonstrated the optimization of a heat pump regarding the temperature glide. They investigated the temperature glide matching for 14 natural refrigerants and their mixtures. It was found that the *COP* increases by up to 27 %, when there is a large temperature change in the heat source along heat transfer. Furthermore, they concluded that a good temperature match in the heat sink and source improve the *COP*, but an optimal match does not necessarily lead to an optimal *COP*.

The reviewed theoretical studies show that *COP*s can be increased significantly by using zeotropic mixtures when the temperature glides match the temperature change in the heat transfer fluids. Roskosch et al. [39] investigated the reason, why theoretical studies often predicting a high increase in *COP* for zeotropic mixtures, while they were often not found in experiments. They found that the change in composition also changes the compressor efficiency, which in modelling studies most often is set constant, leading to the observed discrepancies. It was concluded that a zeotropic mixture is most beneficial for the performance

when the compressor efficiency is nearly constant over the composition and when the temperature glide matches the temperature change in the heat transfer fluids. As mentioned in the reviews [28,35], the experimental study of HTHP especially with hydrocarbons was not carried out often, but is promising as seen from the brief literature review. Thus, the present experimental investigation evaluates propane (R290) /isobutane (R600a) mixtures as working fluids, using heat from water at environmental conditions and delivering secondary fluid enthalpy flows at 40 °C or 60 °C, aiming to determine *COP*s and the exergy destruction in the different components as a function of mixture composition.

2.3 *Experimental*

The used simple compression heat pump system consists of a compressor, an evaporator, a condenser, an expansion valve, and a working fluid reservoir. The simplified system is shown in Fig. 2.1.
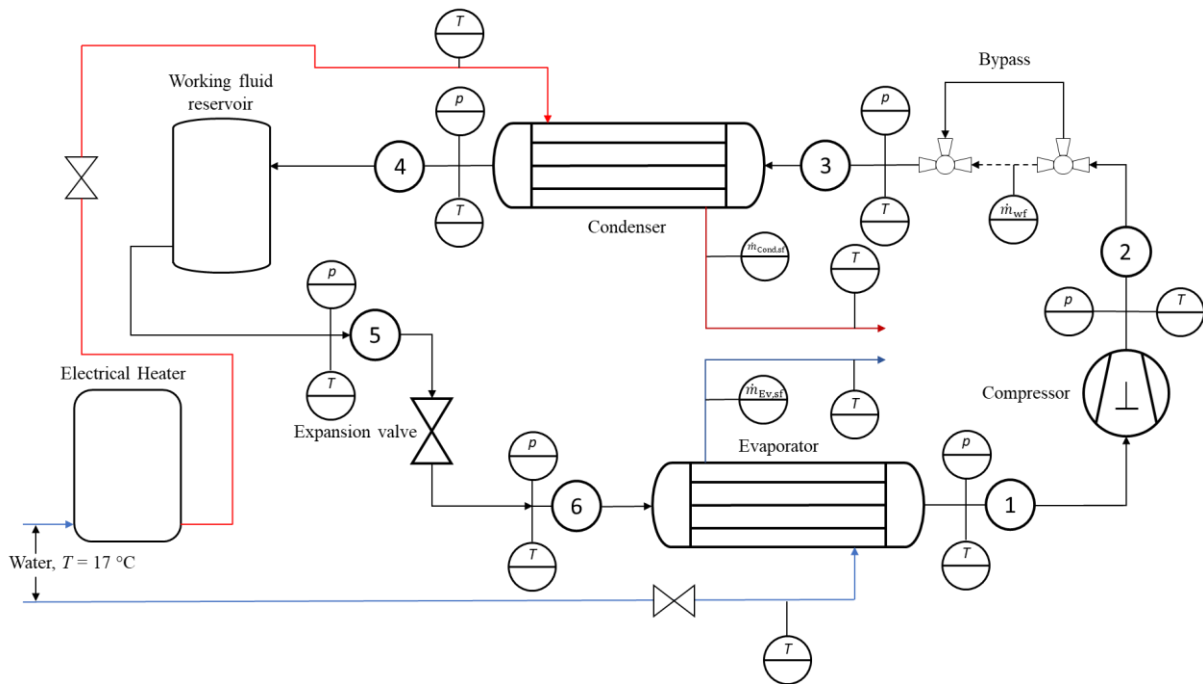
Fig. 2.1 Schematic View of the used compression heat pump.

A semi-hermetic piston compressor (GEA Bock HGHC12P) increases the pressure between states 1 and 2. It has two cylinders, two pole pairs and a maximum power consumption of 2.2 kW. With a frequency inverter, the rotation speed can be varied continuously between 35 and 70 Hz. The actual frequency of the compressor is the AC frequency divided by the pole pair number of two. Thus, an AC frequency of 50 Hz leads to an RPM of 1500 min^{-1}. In the

reference case, the frequency is 1500 min^{-1} and is varied down to 1050 min^{-1}. The stroke volume V_{stroke} of the compressor is 61.74 dm^{-3}, which is needed for the calculation of the theoretical volumetric flow rate. The electrical power consumption of the compressor is measured at the outlet clamps of the inverter. A minimum superheating of the working fluid of 3 °C at the suction side is needed to protect the compressor. The maximum outlet temperature of the compressor is 120 °C due to the limit of the PTFE outlet seal. Reniso Synth 68 from Fuchs is used as machine oil with the thermophysical properties given in Table 2.2.

Table 2.2 Thermophysical properties of Synth 68.

Property	Value
Density at 15 °C	835 kg/m^3
Flash point (Cleveland)	260 °C
Kinematic viscosity at 40 °C	68 mm^2/s
Kinematic viscosity at 100 °C	10.5 mm^2/s
Pourpoint	-57 °C

Water was used as the secondary fluid in both basically counter-flow tube-in-tube heat exchangers, its entrance temperature can be raised to 60 °C with an electric heater; this was varied in the experiments. In the evaporator, water with an inlet temperature of 17 °C and a mass flow rate of around 7 kg/min was used throughout. With this mass flow rate, an evaporator outlet temperature of the working fluid of nearly 17 °C is reached for all operation points. The throttling is realised with the help of a needle valve. The fine adjustment of the needle valve ensures the investigation of a wide range of operating points and allows to control the temperature at the evaporator inlet. The evaporator has an inner tube diameter of 10 mm (wall thickness: 1 mm) and an inner diameter of the outer tube of 16 mm. This results in an annular gap of 2 mm in which the water flows. The evaporator has a length of 14 m. The condenser has an annular gap of 2 mm and an inner tube diameter of the outer tube of 19 mm. The condenser has a total length of 22 m. To compensate the different needed working fluid mass loads at different operation points, a refrigerant reservoir is installed before the needle valve. In this way the system must not be refilled for operation point changes.

The water mass flow rates were measured with an Optiflux 4050 flow meter from KROHNE. Furthermore, the flow rate of the working fluid can be measured with a Coriolis flow meter MFS3081 K 1.5 E from KROHNE for calibration purposes. The use of the Coriolis

flow meter causes heat losses and high pressure drops; thus, we followed the procedure from our previous work on the same system and determined the flow rates from the energy balance in the evaporator, the difference was determined there to be around 2 % [40]. Thus, the bypass shown in Fig. 2.1 was used for all the measurements presented here.

For monitoring and evaluating the processes, 6 pressure sensors and a total of 38 temperature sensors are installed in the system. The pressure sensors are located at the inlet and the outlet of the main components of the system (point 1 - 6 in Fig. 2.1). A temperature sensor is also installed at each of these points. The water temperatures at the inlets and outlets of the heat exchangers are also recorded. These pressure and temperature measurement points are shown in Fig. 2.1. The remaining temperature sensors are installed in the heat exchangers. Thus, the temperature profile inside the heat exchangers can be recorded and evaluated but are not discussed here. The information about the used pressure and temperature sensors within the system including their ranges and accuracies are summarized in Table 2.3.

Table 2.3 Used sensors with manufacturer, type, measuring ranges and accuracies.

Sensor	Manufacturer	Type	Range	Accuracy
Temperature	Sensor Electric	PT-1000 type AA	-5 - 120 °C	$0.1 + 0.005 \cdot T$ [°C]
Pressure	ICS Schneider Messtechnik	IMP331	Position 1 and 5: 0 - 10 bar (absolute) Others: 0 - 25 bar (absolute)	0.1 % [of full span output][1]

The influence of the mixture composition of propane and isobutane, the evaporator inlet temperature, the compressor frequency, and the condenser inlet temperature of water on the heat pump performance was investigated here and were varied. Since only some of the parameters can be selected independently, it was decided to control both temperatures at the evaporator inlet together with the mass flow rate of the secondary fluid, allowing a straight-forward analysis of the exergy destruction in the evaporator. Also, the entrance temperature and the temperature difference of the water in the condenser were kept constant, because these are typical design variables of heat pumps. By keeping these values constant, the outlet

---

[1] This bracket was added and is, thus, deviating from the published manuscript.

temperature of the water in the evaporator, and the secondary fluid mass flow rate in the condenser differ for every operation point and are used for the evaluations. Furthermore, the minimum superheating was met for every data point, while the superheating value varied overall throughout the study since it was controlled for the actual evaporator inlet temperature. Also, the working fluid is subcooled at the outlet of the condenser for the presented work. The process values set in this way are shown in Table 2.4.

Table 2.4 Investigated process boundary conditions.

Parameter	Used values
Mole fraction isobutane, x_{C4H10}	0, 0.25, 0.5, 0.75, 1
Compressor frequency, n_{comp}	1500 min^{-1}, 1050 min^{-1}
Working fluid inlet temperature evaporator, $T_{evap, in}$	0 °C, 4 °C, 8 °C
Secondary fluid inlet temperature evaporator, $T_{evap, sf, in}$	17 °C
Secondary fluid inlet temperature condenser, $T_{cond, sf, in}$	40 °C, 60 °C
Secondary fluid temperature difference condenser, $\Delta T_{cond, sf}$	10 °C
Temperature lift, T_{lift}	33 K, 53 K

The temperature lift is defined as the effective total temperature difference achieved between the evaporator inlet and the condenser outlet temperature of the secondary fluid. Thus, the temperature lifts are 33 K and 53 K.

The target mole fractions of 0.25, 0.5 and 0.75 that are filled into the system, did not correspond to the mixtures circulating during operation. These differed somewhat because the more volatile propane accumulated in the gas phase of some parts of the system, such as the refrigerant reservoir. So, the circulating mixture contains a slightly higher amount of isobutane. The composition of the circulating mixture was determined with the help of the assumption that the expansion valve is isenthalpic, and thus, the mole fractions could be calculated iteratively with the data from RefProp [101], until the enthalpy of a composition before and after the expansion valve were the same. This method was proposed and used by different authors before [102,103]. It was found that the range of the difference to the target mole fractions is from 0.011 to 0.045.

There are several potential sources of error in this experimental work. At first there are systematic errors. For example, oil from the compressor transported with the working fluid, fluctuations in the values while logging the data at an operation point or heat losses throughout

the system. There were different approaches to prevent those errors and minimize the uncertainties. Before logging in the data, a steady operation point was reached for all values. To reduce the statistical error in the fluctuation of the values while operating the system, the data logging was carried out for 5 min (the values are captured every second) and afterwards the mean values were used for the calculations. Furthermore, the measurements were repeated two times. Heat losses are reduced by using polyurethane insulation (thickness: 20 mm) for the whole system, with an additional stone wool insulation (thickness: 30 mm) for the heat exchangers. Besides the approaches to reduce the systematic error, the statistical errors due to the uncertainties of the sensors (See Table 2.3) were analysed for this system in previous work [40]. From error propagation it was shown that the uncertainty is in a range between 0.18 and 3.51 % for the various derived values. For example, the calculated error of the compressor power consumption is 0.36 %, for the *COP* 2.22 % and for the specific exergy loss in the condenser 3.51 %. The error increases for the parameters with a higher contribution of the secondary fluid values to the calculation, due to the temperature sensitivity of the enthalpy and entropy of water. Overall, the repetition measurements showed the same range of error for the present work. Another mentionable source of error is the uncertainty of the equations of state that are used by RefProp [101] for calculating the mixture properties. The authors of the equations for isobutane and propane used within RefProp indicated their uncertainty to be within 1 – 3 % [104, p. 190]. Finally, the reproducibility of the measured data at different days was within 2.5 %.

2.4   *Calculation*

In the following, the most important equations necessary for the evaluation of the experimental data will be introduced and discussed. The *COP* is defined as the ratio of the determined net heat flow rate transferred to the secondary fluid (sf) in the condenser to the consumed compressor power:

$$COP \; = \; \frac{\left| \dot{Q}_{\text{H,sf}} \right|}{P_{\text{comp,el}}} \tag{Eq. 2.1}$$

To analyse the process details, the exergy destruction in different parts are examined. These are generally determined by the difference between entering and exiting exergy flows $\dot{E}$. The exergies, when the contributions of kinetic and potential energy changes are neglected, are given by:

$$\dot{E}_i = \dot{m}_i \cdot ((h_i - h_u) - T_u \cdot (s_i - s_u)) \qquad \text{(Eq. 2.2)}$$

In this equation $\dot{m}_i, T, h, s$ are mass flow rate, temperature, specific enthalpy, and specific entropy, respectively. An ambient (subscript: u) temperature of 25 °C and an ambient pressure of 1 bar were used in this work as dead state. Using Eq. 2.2, the incoming and outgoing exergy flows can be determined for each component and the difference can be calculated as exergy destruction.

Various efficiencies can be defined for the compressor to characterise it. In the present work, the electro-mechanical (subscript: em) compressor efficiency is used with:

$$\eta_{comp,em} = \frac{P_{comp,wf}}{P_{comp,el}} = \frac{\dot{m}_{wf} \cdot (h_{comp,out} - h_{comp,in})}{P_{comp,el}} \qquad \text{(Eq. 2.3)}$$

It represents the ratio of the power delivered to the working fluid (subscript: wf) $P_{comp,wf}$ and the electrical power consumed by the compressor $P_{comp,el}$ and takes the electro-mechanical losses in the compressor into account.

The isentropic efficiency is defined as the ratio of the isentropic compressor power and the power delivered to the fluid:

$$\eta_{comp,is} = \frac{P_{comp,is}}{P_{comp,wf}} = \frac{w_{comp,is}}{w_{comp,wf}} \qquad \text{(Eq. 2.4)}$$

With the inlet state of the working fluid and RefProp [101], the isentropic enthalpy (h) at the outlet of the compressor was calculated and used to determine the isentropic compressor work per mass flow of working fluid $w_{comp,is}$:

$$w_{comp,is} = h_{comp,out,is} - h_{comp,in} \qquad \text{(Eq. 2.5)}$$

The real outlet state of the compressor was used to calculate the specific work delivered to the fluid $w_{comp,wf}$ from the measured data, assuming an adiabatic compressor:

$$w_{comp,wf} = h_{comp,out} - h_{comp,in} \qquad \text{(Eq. 2.6)}$$

The volumetric efficiency is defined as the quotient of the effective volumetric flow rate ($\dot{V}$) into the compressor, as calculated from the density $\rho_{comp,in}$ and the mass flow rate $\dot{m}_{wf}$ and the geometrically highest possible volumetric flow rate:

$$\lambda_{comp} = \frac{\dot{V}_{comp,in}}{\dot{V}_{theoretical}} = \frac{\dot{m}_{wf}}{\rho_{comp,in} \cdot n_{comp} \cdot V_{stroke}} \qquad \text{(Eq. 2.7)}$$

The latter is calculated from the compressor frequency n_{comp} and stroke volume V_{stroke}. The working fluid mass flow rate was determined from the energy balance across the evaporator, which was assumed to be adiabatic, because of the small temperature difference to the environment [40]. Thus, the mass flow rate can be calculated from:

$$\dot{m}_{wf} = \dot{m}_{evap,sf} \cdot \frac{\left(h_{evap,sf,in} - h_{evap,sf,out}\right)}{\left(h_{evap,wf,in} - h_{evap,wf,out}\right)} \qquad \text{(Eq. 2.8)}$$

By using the working fluid mass flow rate and the specific work delivered to the fluid (Eq. 2.6), $P_{comp,wf}$ is determined from the obtained data from the system.

2.5   *Discussion and results*

In the following, first, the *COP* change with mixture composition and further parameters are presented, before going through the different devices aiming to get some insights into the reasons for the found dependencies. The influence of the mixture composition, the compressor frequency and the temperature lift on the *COP* is shown for different operating points in Fig. 2.2. The *COP* is plotted as a function of the isobutane mole fraction for all combinations of compressor frequency and temperature lift and the different evaporator inlet temperatures.
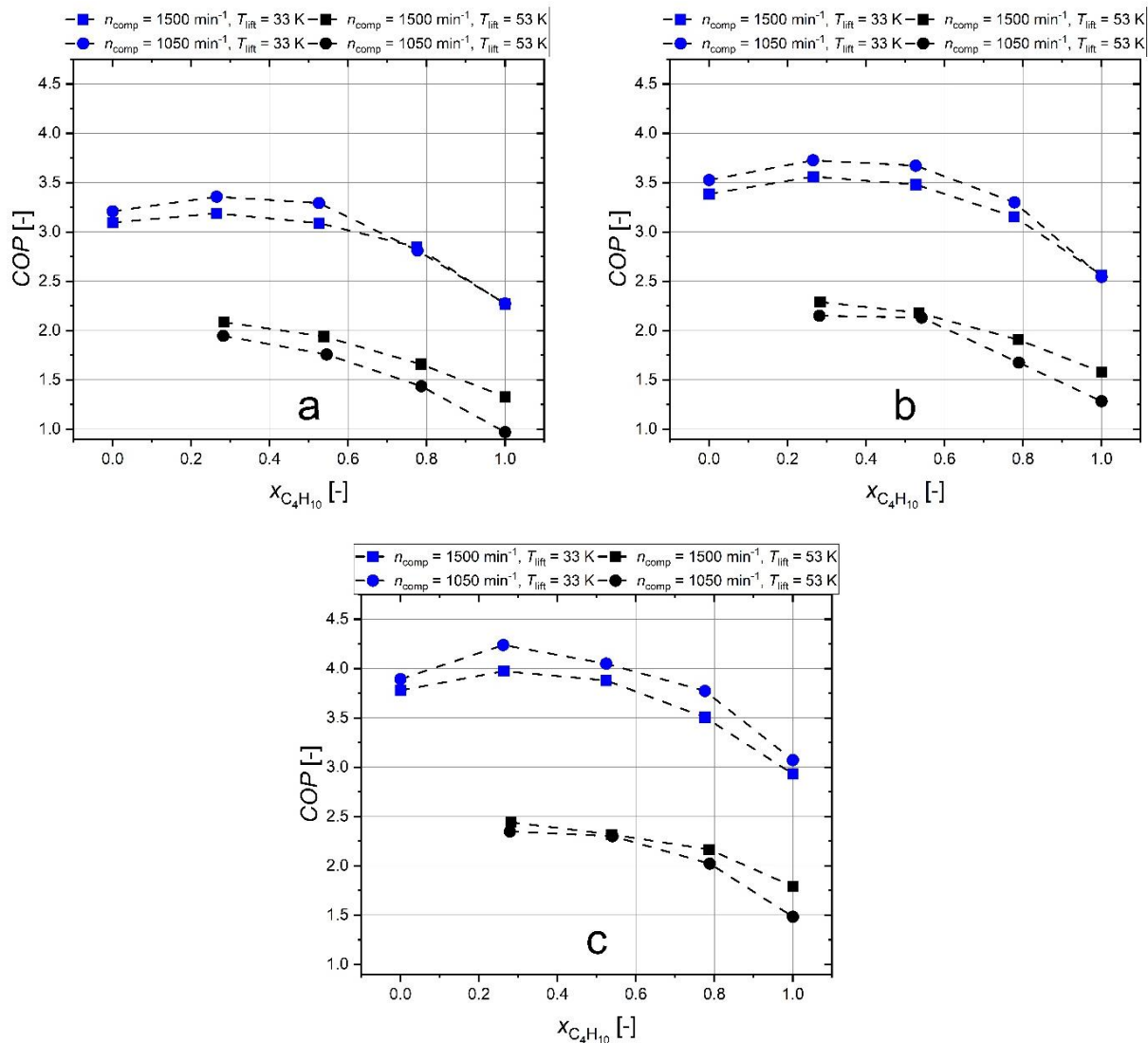
Fig. 2.2 *COP* depending on the mole fraction of isobutane for a) $T_{evap,\,in} = 0\ °C$,
b) $T_{evap,\,in} = 4\ °C$ and c) $T_{evap,\,in} = 8\ °C$.

The values for pure propane (mole fraction of 0) could not be recorded for a temperature lift of 53 K, because the maximum pressure in the system would exceed the limit of 20 bar. The lowest measured *COP* here is 0.97 (below 1, due to experimental uncertainties) for 0 °C, 1050 min^{-1} and a temperature lift of 53 K at an isobutane mole fraction of 1. The highest measured *COP* is 4.24 for 8 °C, 1050 min^{-1} and a temperature lift of 33 K at an isobutane mole fraction of 0.262. Overall, it can be seen that the *COP* increases, as expected from the reversible (Carnot) limit, with increasing evaporator inlet temperature. The trends of the *COP* dependencies are similar for the different temperatures, therefore, the results for the evaporator inlet temperature of 4 °C are discussed in more detail.

COPs between 2.54 and 3.73 are found for the lower temperature lift of 33 K, as seen in Fig. 2.2 (b), which are higher than those for the higher temperature lift, where values between 1.28 and 2.29 are observed. Within a composition-variation series, pure isobutane leads throughout to the lowest *COP*s; the highest *COP*s are found for isobutane mole fraction of 0.25, but the increase of the *COP* from pure propane to the maximum is only around 5 %. As mentioned before, the circulating mole fraction differed from 0.25 and was determined to be 0.267. The *COP* for pure propane as refrigerant is higher than for pure isobutane, the latter *COP*s always being the lowest of each series.

The optimal zeotropic mixture increases the *COP* compared to the pure refrigerants. This can be attributed to the temperature glide that occurs for mixtures, leading to a better matching between working fluid temperatures and secondary fluid temperatures and reduces the exergy losses in the heat exchangers, as will be discussed later. With the rising temperature glide, the temperature difference between working fluid and secondary fluid is lower and, in addition, the pressure ratio in the compressor decreases. As an example, the measured temperature glides in the condenser are plotted in Fig. 2.3 as a function of the isobutane mole fraction for a compressor frequency of 1500 min^{-1} and an evaporator inlet temperature of 4 °C.
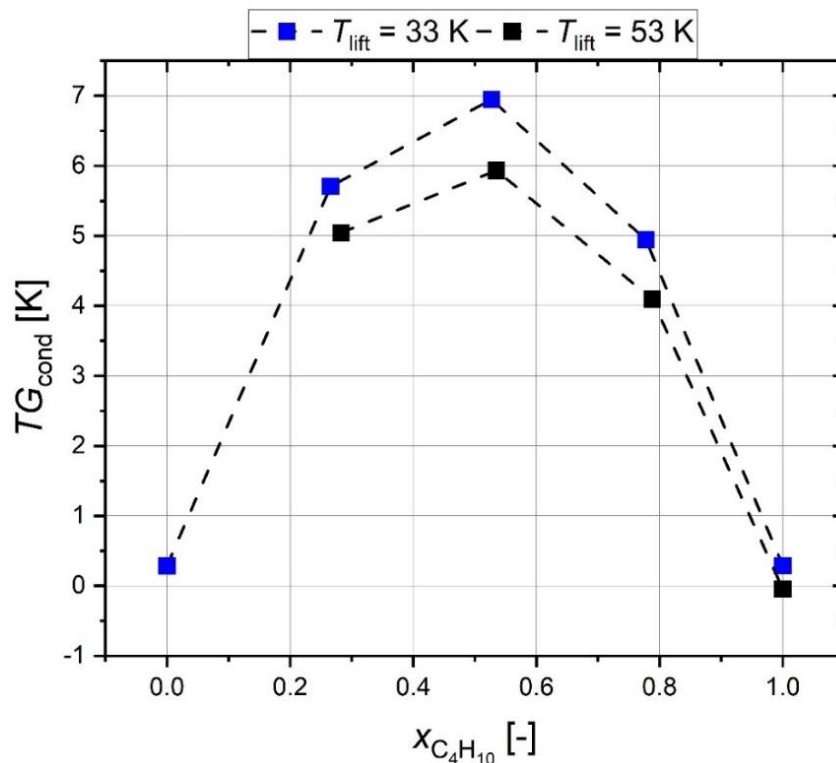
Fig. 2.3 Temperature glide in condenser depending on isobutane mole fraction at $T_{evap, in} = 4$ °C and $n_{comp} = 1500$ min^{-1} for both temperature lifts.

For ideal mixtures, the largest temperature glide is expected at a mole fraction of 0.5, here the highest temperature glide is found at a fraction of 0.527 and is 5.94 K for a temperature lift of 53 K and 6.95 K for 33 K. The small, but not vanishing temperature glide for the pure fluids is caused by the pressure drop in the condenser. In general, the temperature glide is larger at lower temperature lifts of the heat pump (33 K here), because the condensation pressure is lower, and thus, the difference between boiling point and dew point is increased. The larger temperature glide approaches the temperature change of 10 K of the secondary fluid, and this better temperature matching in the heat exchanger leads to a lower exergy destruction. By comparing Figs. 2.3 and 2.2, it is noticed that the operating point with the highest *COP* is not found for the mixture with the highest temperature glide, but at a mole fraction of 0.267. Thus, the positive effect of the temperature glide must be superimposed by another dependency. From previous work, the variation in compressor efficiency with composition was suspected, which may be a direct or an indirect effect, as discussed next.

To examine the influence of the compressor, the change of the *COP* with the compressor frequency can be considered first by regarding Fig. 2.2 once more. It is seen that the influence of the compressor frequency is changing between the low and the high temperature lift. For a high temperature lift the *COP* is lower for the lower frequency, while for the 33 K lift, the opposite behaviour is observed, and the *COP* is higher at 1050 min^{-1}. The increase of the *COP* for the lower temperature lift can be explained by a reduction of the compressor losses, due to lower friction losses as also discussed in previous work [105]. The inverse finding is astonishing and justifies a closer look at this opposing behaviour. For the nominal isobutane mole fraction of 0.25, Table 2.5 compares the three compressor efficiencies, the isentropic, the electro-mechanical, and the volumetric efficiency, as a function of frequency and temperature lift, all for an evaporator inlet temperature of 4 °C.

Table 2.5 *COP*, isentropic and electro-mechanical efficiency and volumetric efficiency for $T_{\text{evap, in}} = 4$ °C and a target mole fraction of 0.25 depending on the compressor frequency and temperature lift.

	1500 min^{-1} 33 K	1050 min^{-1} 33 K	1500 min^{-1} 53 K	1050 min^{-1} 53 K
COP (-)	3.56	3.73	2.29	2.15
$\eta_{\text{comp, is}}$ (-)	0.619	0.631	0.637	0.642
$\eta_{\text{comp,em}}$ (-)	0.951	0.975	0.920	0.890
λ_{comp} (-)	0.731	0.725	0.640	0.608

The *COP* increases for the lower temperature lift from 3.56 to 3.73 with decreasing compressor frequency, while the *COP* increases from 2.15 to 2.29 with frequency for the higher temperature lift. The isentropic efficiency is increasing with frequency reduction for both, but for the lower temperature lift, the increase is higher with 1.94 % compared to 0.78 % for the higher lift. Only for the electro-mechanical efficiency, an opposing behaviour as for the *COP* is noticed, it increases by 2.52 % for the 33 K lift and decreases 3.26 % for the 53 K lift. The volumetric efficiency is increasing with frequency for both temperature lifts but for the lower lift the decrease is only 0.82 %, while for the higher lift 5 %.

The finding that a higher compressor frequency is beneficial for a high temperature lift but disadvantageous for a low frequency regarding the *COP* can be rationalized from these numbers: if $P_{comp,el}$ from Eq. 2.1 is expressed with the electro-mechanical and the isentropic compressor efficiency, the influence of the latter gets obvious:

$$COP = \eta_{comp,is} \cdot \eta_{comp,em} \cdot \frac{\dot{Q}_{H,sf}}{\dot{m}_{wf} \cdot \left(h_{comp,out} - h_{comp,in}\right)} \qquad \text{(Eq. 2.9)}$$

But also, the composition influences further operating conditions. To examine this, the mass flow rate, the density at the inlet of the compressor, the volumetric efficiency and the pressure ratio of the compressor (outlet pressure divided by the inlet pressure) for a temperature lift of 33 K are given in Table 2.6.

Table 2.6 Isobutane mole fraction dependence of the density at the compressor inlet, working fluid mass flow rate, the volumetric efficiency and the pressure ratio; all for $n_{comp} = 1500 \text{ min}^{-1}$ and $T_{lift} = 33$ K.

x_{C4H10} (-)	$\rho_{comp,\,in}$ (kg/m^3)	$\dot{m}_{wf}$ (kg/s)	λ_{comp} (-)	π_{comp} (-)
0	9.75	0.0110	0.7299	3.457
0.267	8.09	0.0092	0.7312	3.417
0.527	6.59	0.0074	0.7225	3.509
0.778	5.26	0.0057	0.6979	3.695
1	4.15	0.0044	0.6763	4.078

With increasing isobutane mole fraction, the density of the mixture entering the compressor, as well as the working fluid mass flow rate, decrease almost linearly. The volumetric efficiency dependence of the compressor is non-linear; a maximum of 0.7312 for an isobutane fraction of 0.267 is observed and it decreases slightly towards pure propane and stronger towards pure

isobutane. A high volumetric efficiency means a better utilisation of the compressor (see Eq. 2.7). Also, the pressure ratio is lowest for the isobutane mole fraction of 0.267 and the highest for pure isobutane, the trend resembles the one of the volumetric efficiency. The combination of the highest volumetric efficiency, the lowest pressure ratio, and the high working fluid mass flow rate, at a mole fraction of 0.267, leads to a high total compressor efficiency and a high *COP*.

Furthermore, the mixture composition influences the heat transfer to the secondary fluid and thus the *COP*. To underline this, the composition-dependence of the heat transferred per mass-unit of fluid (*q*) in the condenser is shown in Fig. 2.4.
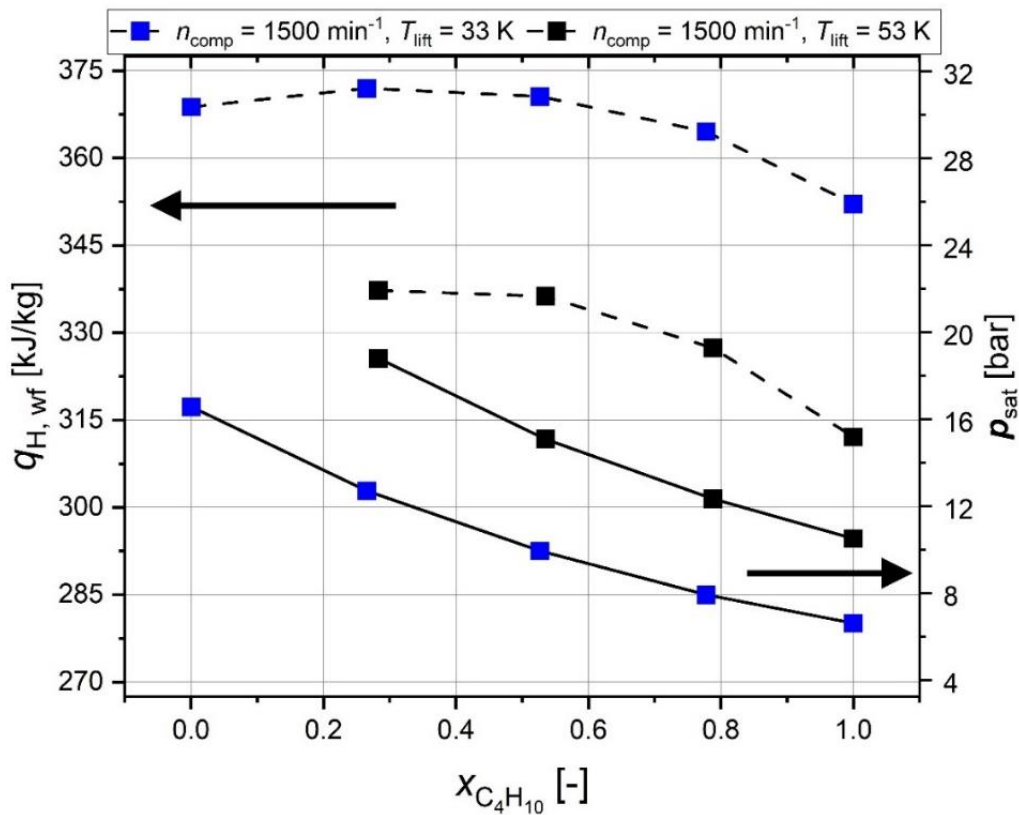
Fig. 2.4 Heat transferred per mass-unit (dashed line) and saturation pressure in the condenser depending on the isobutane mole fraction at n_{comp} = 1500 min^{-1} and $T_{evap, in}$ = 4 °C for both temperature lifts.

The composition dependence of the heat transferred per mass-unit in the condenser is similar to the course at the same conditions in Fig. 2.2 for both temperature lifts with a maximum at an isobutane mole fraction of 0.267. This behaviour is mainly due to the composition dependence of the condensation enthalpy, which makes up the largest part of the heat transferred to the secondary fluid in the condenser. The condensation enthalpies associated with the temperature

glides (shown in Fig. 2.3), and the heat transfer rates in the condenser (related to the working fluid) are listed in Table 2.7. The boundary conditions are the same as in Fig. 2.4.

Table 2.7 Specific condensation enthalpies, condenser heat flow rates, and temperature glide in the condenser for isobutane mole fractions at $n_{comp} = 1500$ min^{-1}, $T_{lift} = 33$ K and $T_{evap, in} = 4$ °C.

x_{C4H10} (-)	Δh_{cond} (kJ/kg)	$\dot{Q}_{H,wf}$ (kW)	TG (K)
0	288.55	4.06	0.286
0.267	310.15	3.41	5.706
0.527	315.92	2.73	6.947
0.778	312.29	2.07	4.946
1	300.94	1.53	0.290

From Table 2.7 it is seen that the condensation enthalpy increases with rising temperature glide up to the maximum of 315.92 kJ/kg at an isobutane mole fraction of 0.527, while the enthalpy of 310.15 kJ/kg for a mole fraction of 0.267, however, is not far below and much higher than the propane enthalpy of evaporation of 288.55 kJ/kg. The heat flow rate in the condenser decreases with increasing isobutane mole fraction due to the decreasing mass flow rate (see Table 2.6), with the maximum heat flow rate for pure propane. Thus, for pure propane, the heat flow rate does not rise sufficiently to compensate for the larger mass flow rate obtained, resulting in a small decrease of the heat flow rate compared to the one determined with a mole fraction of 0.267. For a mole fraction of 0.527, the condensation enthalpy and the temperature glide are both maximal, but the mass flow rate is low, due to the lower density of the mixture. The result is that for the mixture with an isobutane fraction of 0.267 the condenser heat flow rate is the highest and the ratio of $\dot{Q}_{H,sf}$ and $\dot{m}_{wf}$ is maximal.

Finally, the fluid dependent specific exergy destruction of all components are shown to analyse their influence on the system performance and the *COP*. The specific exergy destruction depending on the isobutane mole fraction for a compressor frequency of 1500 min^{-1}, a temperature lift of 33 K (a) and 53 K (b) with an evaporator inlet temperature of 4 °C are shown in Fig. 2.5.
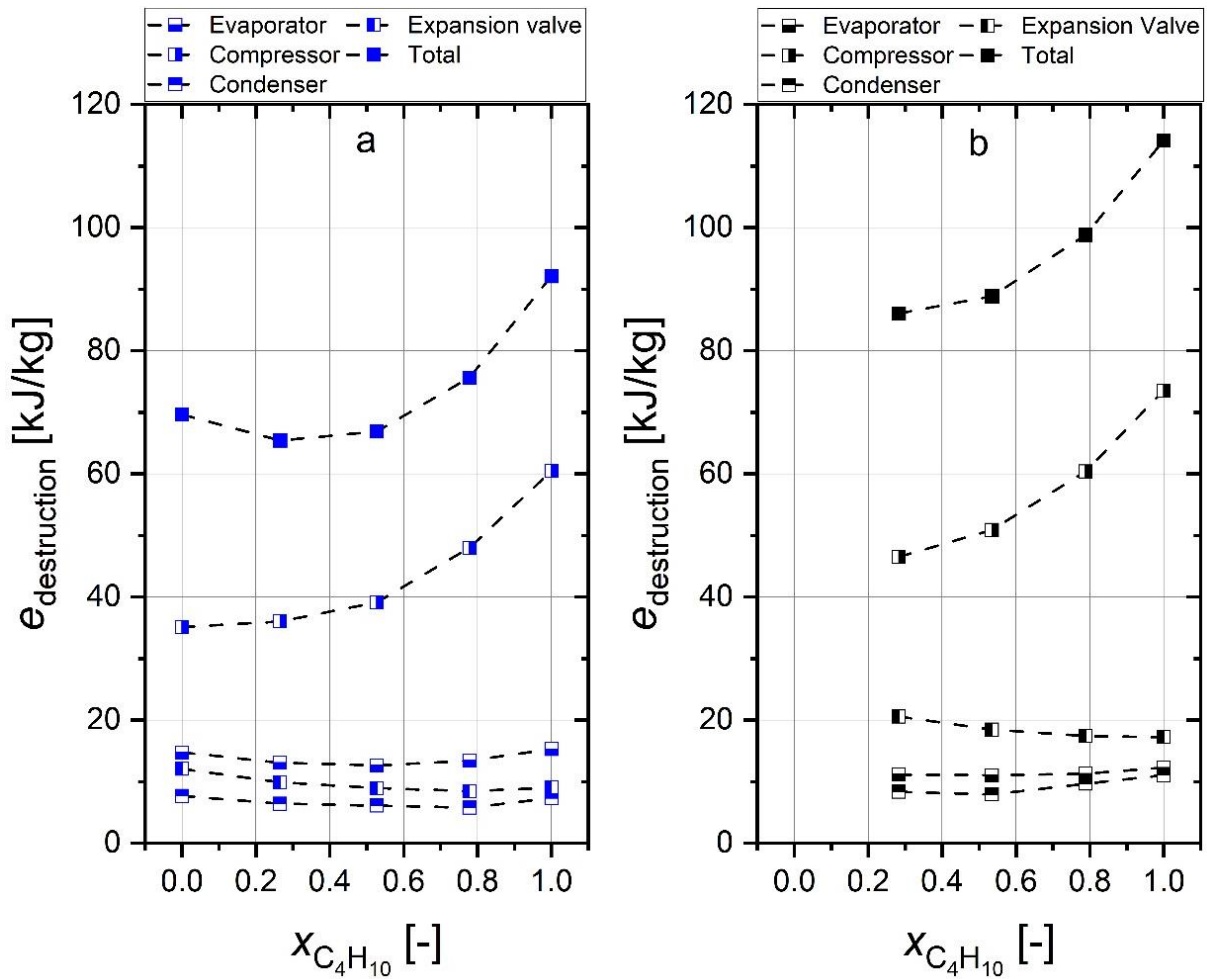
Fig. 2.5 Specific exergy destruction depending on the isobutane mole fraction at n_{comp} = 1500 min^{-1} for $T_{evap,\,in}$ = 4 °C and (a) T_{lift} = 33 K (b) T_{lift} = 53 K.

For T_{lift} of 33 K it is seen that the total specific exergy losses are in the range between 65 kJ/kg and 92 kJ/kg. The lowest exergy destruction is found for a mole fraction of 0.267 and the highest for pure isobutane. The losses with pure propane and with a mole fraction of 0.5 are only slightly above the minimum. The exergy destruction in the condenser is lowest, with values between 5.8 kJ/kg and 7.7 kJ/kg. The component with the next highest irreversibilities is the expansion valve (8.5 kJ/kg - 12.1 kJ/kg). The evaporator leads to slightly higher destruction of 12.6 kJ/kg to 15.3 kJ/kg, while the compressor shows the largest irreversibilities between 35 kJ/kg and 60 kJ/kg. As expected for a temperature glide, the specific exergy destruction in the condenser is highest for the pure refrigerants. The observed low increase of around 5 % of the maximum *COP* for mixtures compared to pure propane can be explained here too. The contribution of both heat exchangers to the total exergy loss is only around 25 % for 33 K. Thus, the possibility to reduce the exergy destruction with increasing the temperature glide is limited

by the low share of the heat exchangers on the losses. With increasing temperature lift (53 K in b) the contribution of the heat exchangers to the total exergy destruction decreases to around 21 %, so that the reduction potential gets even lower with higher temperature lifts. Because of this, the *COP* range from minimum to maximum for different mixture compositions decreases from 1.19 for 33 K to 1.01 for 53 K (see Fig. 2.2).

In comparison to the heat exchangers, the compressor has a very high share of the total exergy destruction. It contributes between 50.4 % and 65.67 % and the courses of the total exergy destruction follows the one of the compressor so that it can be concluded that the compressor is the most important component for the total exergy destruction of the process and has a main influence on the *COP* too. To address this further, a closer look shall be taken at the electrical and isentropic specific work of the compressor for a temperature lift of 53 K in Fig. 2.6.
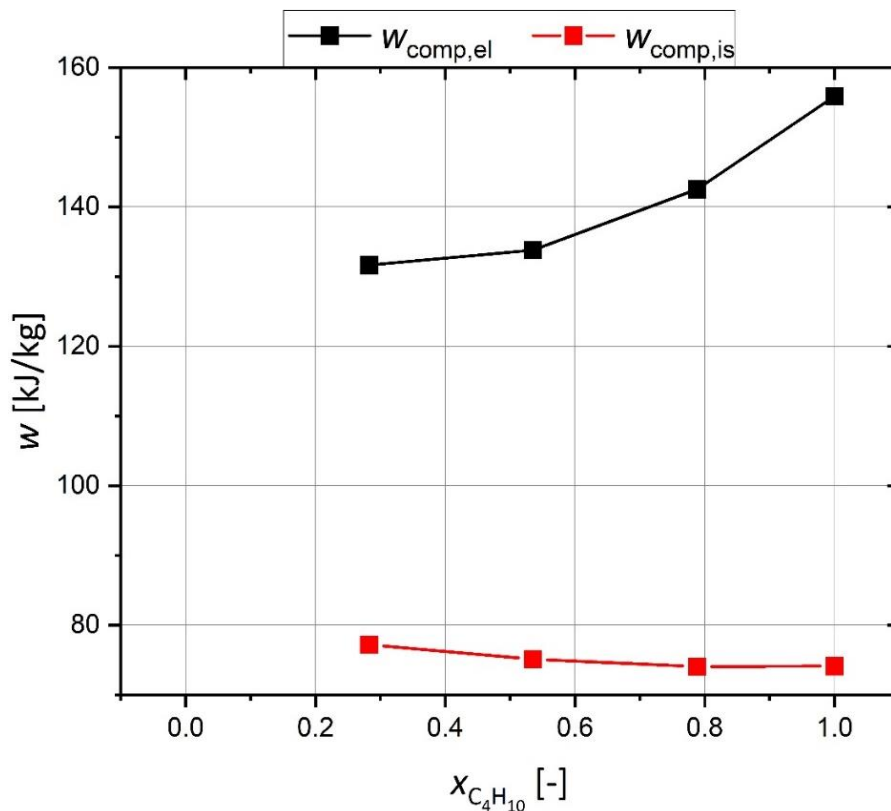
Fig. 2.6 Specific electrical and isentropic compressor work depending on the isobutane mole fraction at $n_{comp} = 1500$ min^{-1}, $T_{lift} = 53$ K and $T_{evap, in} = 4$ °C.

In Fig. 2.6 it is seen that the specific electrical work ($w_{el} = P_{comp,el}/\dot{m}_{wf}$) of the compressor (black line) increases with the amount of isobutane in the mixture, similar to the behaviour of the exergy destruction in the compressor, while the needed isentropic work is slightly falling

with isobutane content. Eq. 2.10 combines Eq. 2.3 and Eq. 2.4, and the electrical specific work can be divided into three parts: the specific isentropic work and the electro-mechanical and isentropic compressor efficiencies:

$$w_{\text{comp,el}} \; = \; w_{\text{comp,is}} \; \cdot \; \frac{1}{\eta_{\text{comp,em}} \cdot \eta_{\text{comp,is}}} \qquad \text{(Eq. 2.10)}$$

As the isentropic compressor work only decreases slightly with the isobutane mole fraction, as seen in Fig. 2.6 (red line), the change in the electro-mechanical and isentropic compressor efficiency is the reason for the increase of the electrical compressor work. To show this, the compressor efficiencies, the pressure ratio and the volumetric efficiency are shown in Fig. 2.7 as a function of the isobutane mole fraction.
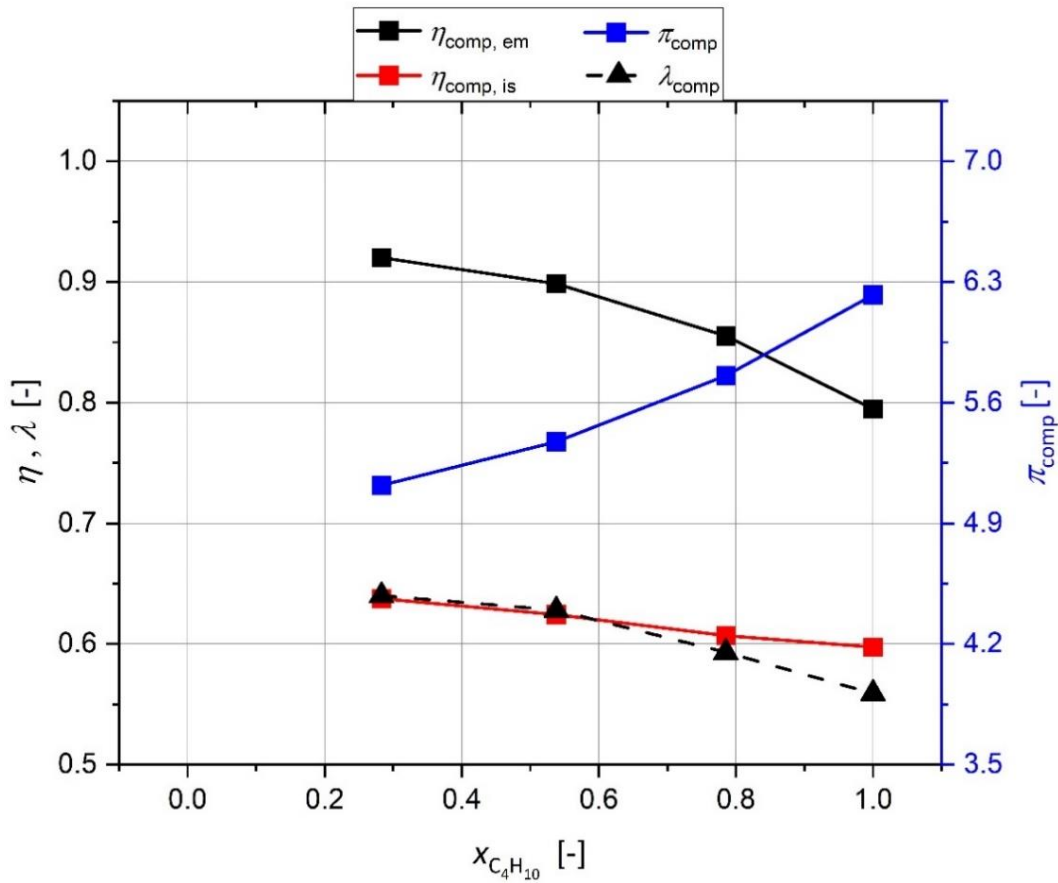
Fig. 2.7 Internal compressor efficiency $\eta_{\text{comp, em}}$, isentropic efficiency $\eta_{\text{comp, is}}$, volumetric efficiency λ_{comp} and the pressure ratio π as a function of the isobutane mole fraction at $n_{\text{comp}} = 1500 \text{ min}^{-1}$, $T_{\text{lift}} = 53 \text{ K}$ and $T_{\text{evap, in}} = 4 \text{ °C}$.

Interestingly, the electro-mechanical efficiency drops with the isobutane mole fraction. Because the electro-mechanics has not any direct relation to the working fluid, this must be due to the

change in the mechanical variables, the pressure levels along the volume change. Therefore, the pressure ratio of the compressor is shown in blue in Fig. 2.7, which increases from 5.12 at $x_{C_4H_{10}} = 0.267$ to 6.22 for pure isobutane. This increase of the pressure ratio also leads to the decrease of the volumetric efficiency (dashed line) with the isobutane mole fractions. As a result of this, it is seen that both compressor efficiencies decrease with the isobutane mole fractions, but for $\eta_{\text{comp, em}}$ (black line) the reduction by 13.65 % is higher than for $\eta_{\text{comp, is}}$ (red line) which falls by 6.3 %. The courses of λ_{comp} and $\eta_{\text{comp, em}}$ are similar, λ_{comp} falls by 12.65 %. Thus, the utilisation of the compressor drops with isobutane mole fractions due to the pressure ratio and the volumetric efficiency, resulting in lower compressor efficiencies, causing the increase in the needed specific electrical work (Eq. 2.10 and Fig. 2.6). This altogether leads to the highest *COP* at a mole fraction of 0.267 within the investigated operation points.

2.6   Conclusion

Experimental results for the fluid dependence of the performance of a water-water compression heat pump system with a propane-isobutane mixture and higher temperature levels are presented. The temperature level for the secondary fluid water, which acts as heat source, was 17 °C. The rejected heat was used to heat water to 50 °C and 70 °C, respectively, both with a 10 °C temperature increase within the condenser. These temperature lifts of 33 K and 53 K are typical for a sustainable system providing hot water. The performance was investigated as a function of the evaporator inlet temperature, compressor frequency and isobutane mole fraction in a propane/isobutane working fluid mixture. Although, the use of this zeotropic mixture has a positive effect on the process due to the temperature glide and the associated higher condensation enthalpy, both effects on the *COP* are limited, because the mixture density varies monotonically and leads to lower working fluid mass flow rates with increasing isobutane mole fraction. The temperature glide reduces the heat-transfer exergy destruction and therefore tends to increase the *COP*, but due to the low contribution of both heat exchangers to the total irreversibility of 21 − 25 %, this effect is limited and gets even smaller with higher temperature lifts. Compared to this, the compressor accounts for a high share of the total exergy destruction between 50 % and 66.67 %. It has a large influence on the process and especially the *COP*. The largest temperature glide is observed at an isobutane mole fraction of 0.527, but the highest *COP* is at 0.267. At this composition, the lowest specific compressor work is found, and it was shown that the higher compressor efficiencies are the reason for this. The efficiencies decrease with higher amounts of isobutane mainly through the

reduction of the internal compressor efficiency that is caused by the decreasing volumetric efficiency and increasing pressure ratio of the compressor. Therefore, it can be concluded that the heat exchangers and with them the moderate temperature glide has a smaller influence than expected, while the change in working conditions lead to indirect effects, which influence the important compressor efficiency, leading to the found shift in the highest *COP* to a mole fraction of 0.267. From this it gets clear that using constant compressor efficiencies in cycle calculations for different fluid mixtures will not lead to reliable results. In this context, the often-neglected electro-mechanical efficiency-changes have to be characterized carefully. Finally, the advantage of zeotropic mixtures should gain in importance for mixtures with larger temperature glides used to heat secondary fluids with adapted temperature changes. This may be worth future investigations.

Chapter 3

An experimental investigation of secondary fluid parameters on heat pumps with higher temperature lift and zeotropic working fluid

The content of this chapter is submitted to the International Journal of Refrigeration:
J. Quenel and B. Atakan. Propane-isobutane mixtures in heat pumps with higher temperature lift: an experimental investigation.

Table 3.1 Author contributions for the paper following the CRediT author statement methodology [87].

Category	Quenel	Atakan
Conceptualization	X	X
Methodology	X	
Software	X	
Validation	X	
Formal analysis	X	
Investigation	X	
Resources		X
Data Curation	X	
Writing - Original Draft	X	
Writing - Review & Editing	X	X
Visualization	X	
Supervision		X
Project administration		X
Funding acquisition		X

Author contributions to this paper

My contribution embraced developing the concept, carrying out the experiments, conducting the data analysis, visualization and writing the manuscript. Burak Atakan developed concepts and reviewed the results as well as the manuscript.

Introduction and key results of the second paper

In the last chapter, the influence of an isobutane/propane mixture as a working fluid was explored for the higher temperature level, wherein the temperature glide affects the temperature change match from the working fluid perspective. On the other hand, this match can also be influenced by changing secondary fluid parameters, which frequently occur in practice due to variations in heat demand or the temperature of the heat source. Consequently, it is crucial for investigations to also consider this impact and given the practical significance of these external condition changes, such a study supports overcoming biases against the use of heat pumps in existing buildings.

Therefore, the work in this chapter retained the higher temperature level and the best-performing working fluid mixture with an isobutane mole fraction of 0.25 from the previous research for further investigation. The heat demand of a heating system is connected to user requirements and directly affects both the mass flow rate and the return temperature of water to the heat pump. For this reason, this study varied both parameters to examine their influence on the process. Additionally, altering the water inlet temperatures into the evaporator represented the potential variations in the heat source, particularly pertinent for widely used air-to-water heat pumps.

The resulting main contributions of this work to the state of the art can be shortly summarized as follows:

- Experimental data is provided for an isobutane/propane (0.25/0.75) working fluid mixture with sink temperature levels of 60 to 75 °C and source levels of 8 to 29 °C.
- The compressor proves to be the component with the highest exergy destruction also at this temperature level.
- The relation between throttling, mass flow rate and pressure drop in the expansion valve is responsible for varying temperature and pressure levels in the two-phase regime of the evaporator. Especially the resulting pressure level strongly affects the process by changing the compressor pressure ratio.
- A lower pressure ratio leads to higher shares of power transferred to the fluid, superimposed at low working fluid mass flow rates by the needed base power to drive the compressor.
- A high compressor load is preferrable for the performance of the process due to the more efficient compressor, even when the *COP* would decrease in theory.

3.1   Abstract

Heat pumps are also discussed for replacing conventional house heating systems at higher temperatures. Their performance also depends on the heat demand, heating system return temperature, as well as the heat source temperature, which determine the reversibly achievable coefficient of performance (*COP*). To approach reversibility in the heat exchangers, zeotropic mixtures are often investigated, but the mean temperature difference in the heat exchangers is also varies with secondary fluid parameters and heat load. Thus, this study experimentally investigates the impact of secondary fluid parameters on the performance of a water-water compression heat pump system with sink temperature levels of 60 to 75 °C and source levels of 8 to 29 °C. The heat pump operates with a piston compressor and a 0.25:0.75 isobutane-propane working fluid mixture. The system performance is analysed as a function of heat demand; the cycle is adapted by variable throttling. *COPs* and exergy destruction rates of the individual components are evaluated, revealing the influence of secondary fluid parameters on the process, especially via the influence on the cycle mass flow rate and the compressor efficiency. The *COP* rises by 63.4 %, if the heat flow demand rises from 1.17 to 3.17 kW. The variation in the working fluid throttling for matching the heat demand, influences pressure levels, mass flow rates, pressure ratios, and compressor efficiencies, often neglected in simple cycle calculations. Varying the evaporator water inlet temperature showed no significant change in *COP*, because of the counteracting of variations in compressor efficiency and evaporator exergy destruction.

3.2   Introduction

Heat pumps can contribute to climate-neutral heating systems and are currently being discussed as a widely used replacement for conventional heating systems, because the electrification increases with higher amounts of energy from renewable sources.

For this reason, studies with possible climate friendly working fluids [36,106,107], optimisations for systems using heat pumps [99,108–110] or investigations focussing for example on compressors [30,39,92,105,111,112] or heat exchangers [113,114] exchangers are carried out.

A lot of studies consider natural working fluids like hydrocarbons as an option to replace environmentally harmful ones like fluorocarbons. Hydrocarbons were investigated in several cycles [35,89,93,94,115,116], due to their low GWP and their good thermodynamic properties.

Zeotropic working fluid mixtures can achieve lower exergetic losses in heat exchangers in combination with sensible heat sources and sinks [41,44,90,91], because of the temperature glide that occurs during phase change on working fluid side. It reduces the temperature difference between the working fluid and the secondary fluid throughout the heat exchange. Heat pumps are often considered for low temperature lifts, but the interest in higher temperature heat pumps (HTHP) increases [28,31,32,117–119]. They provide secondary fluid exit temperatures T_h of 50 to 120 °C for the condenser with heat sources around 5 to 50 °C or even higher and could be used for example for warm water distribution or for conventional house heating systems. Due to the temperature lift (ΔT) dependency of heat pumps, seen from the limiting reversible coefficient of performance ($COP_{rev} = T_h / \Delta T)^2$, those temperature ranges for the secondary fluid have an impact on the performance.

For domestic hot water production, Cui et al. [30] investigated the influence of the compressor control strategy on the performance of a CO_2 heat pump experimentally. For the secondary fluid side, the condenser inlet temperature was varied between 20 to 30 °C and heated up to 65 °C as well as the heat source inlet temperature was set between 15 and 25 °C. They considered for example the *COP,* the heat flow rate in the condenser and the compressor power and aimed for control strategies to maintain the heating performance for those different variations. It was concluded that higher compressor rotating speeds increase the heat flow rate while slightly decreasing the *COP*. Furthermore, they found the rotation speed to be a good control variable, maintaining the heating performance, while the temperatures of the secondary fluids are changing.

Bamigbetan et al. [29] evaluated a cascade heat pump that can provide energy up to 115 °C using residual heat at 25 to 35 °C experimentally. It had a heating capacity of 20 kW with propane in the low temperature and butane in the high temperature cycle. The influence of compressor speed as well as the inlet and outlet temperatures of the heat sink and source were investigated. For the considered temperature lift range of 58 to 72 °C they found an average *COP* of 3.1, while the highest at 58 °C was nearly 3.6. This was obviously superior to electrical heaters or gas boilers for their boundary conditions.

Cao et al. [110] carried out a theoretical optimisation of an ejector enhanced heat pump system with an butane/R143a mixture by using a multi-objective non-dominated sorting

---

[2] Calculated with thermodynamic mean values.

algorithm. They aimed to analyse the performance of the system and compared it to conventional ones. Furthermore, a thermo-economic and exergy analysis was conducted, and the mass fraction of butane, along with the condensation and evaporation temperatures were varied. They stated that with increasing condensation temperatures, the unit cost of product and *COP* decrease, while the heating load, exergetic efficiency and net consumed power increase. Also, rising evaporation temperatures led to increasing total product costs, exergetic efficiencies and *COP*s.

For industrial waste heat recovery, Mateu-Royo et al. [89] theoretically examined the energetic, economic and environmental performance of high temperature heat pump configurations using various low GWP working fluids. To simulate different waste heat sources, two variations for the heat source inlet were used with 30 to 50 °C as well as 70 to 90 °C. Besides that, the heat sink outlet temperature ranged between 100 and 150 °C. Ten different working fluids were investigated for these conditions. Amongst others, they concluded that single stage compression configurations are more suitable for temperature lifts below 50 °C and two-stage concepts should be used for temperature lifts over 60 °C. Furthermore, a significant potential of two-stage booster cycles for industrial waste heat recovery was identified.

Zhao et al. [120] optimised the working fluid and temperature matching of a geothermal cascade consisting a heat pump. The thermodynamic, economic and environmental performance of the system was taken into account, while investigating 4 different hydrocarbons as working fluid. With the help of a model, the optimal temperature matchings in the heat exchangers of the whole system were calculated for all working fluids. They found butane to have the largest *COP* and generally the optimal minimum approach temperatures in the heat exchangers should be minimal, like 3 °C. By performing a sensitivity analysis, they saw that all temperatures and temperature differences had an impact on the *COP*, but the injection temperature back into the ground had the highest influence.

Ganesan et al. [32] theoretically analysed a cascade HTHP providing water from 100 to 118 °C. Mixtures of CO_2 with butane and pentane were used as working fluid. The working fluid mixtures and the heat source inlet temperature (10-50 °C) were varied to examine the performance of the system analysing the *COP*, condenser outlet temperature, and heating capacity. They drew the conclusion that the heat source temperature has a great influence on the performance of the system, because the *COP* rose with increasing temperatures. With the

CO_2 fraction, the hot water temperature increased up to 118 °C for 8 % CO_2, while the highest *COP* of 4.5 was found for 2 %.

The publications reviewed show that secondary fluid parameters are often fixed in heat pump investigations while work on the impact of their variations is scarce. While zeotropic mixtures are investigated often to reduce the mean temperature difference in the heat exchangers, and thus reducing entropy production, the mean temperature is also influenced by the not often studied secondary fluid parameters. Their influence on heat pump heating systems with zeotropic mixtures is unclear and is addressed in the present work, because they vary with heat demand and the surrounding or heat source temperature. The variations in heating demand, specifically the heat flow in the condenser, are explored by adjusting mass flow rates and introducing temperature variations in the condenser for the secondary fluid. Furthermore, diverse external conditions during heating are considered by varying the secondary fluid's inlet temperatures in the evaporator. This approach aims to systematically elucidate the influence of secondary fluid parameters on the overall process and its individual components.

3.3   *Experimental*

The used compression heat pump system was mainly the same as in the previous study [86] and consists of a compressor, an evaporator, a condenser, an expansion valve, and a working fluid reservoir. Now, an electrical heater is also used to vary the water inlet temperature in the evaporator. The secondary fluid was water in the evaporator and in the condenser, respectively. The system is shown in Fig. 3.1.
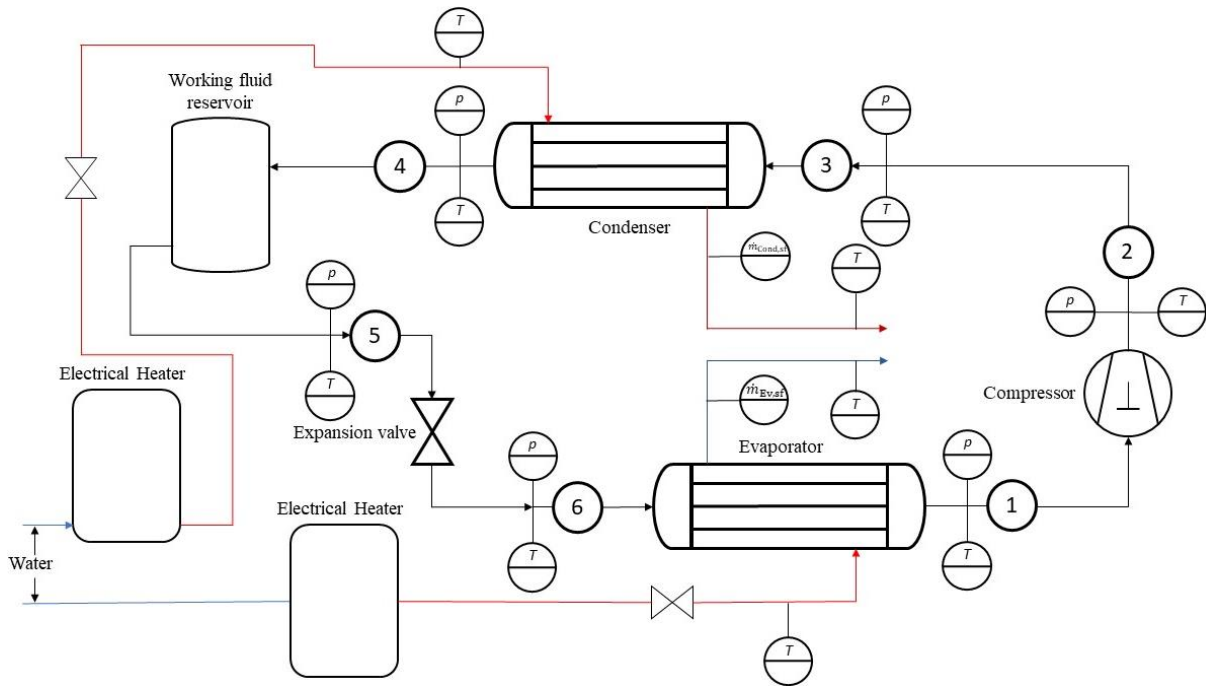
Fig. 3.1 Schematic View of the used compression heat pump.

The semi-hermetic piston compressor (GEA Bock, HGHC12 running with machine oil Reniso Synth 68 from Fuchs) increases the pressure between states 1 and 2. The compressor has a maximum power consumption of 2.2 kW, it has two pole pairs, and two cylinders; the rotation speed is kept constant at 1500 min^{-1}. At the outlet clamps of a frequency inverter, the electrical power consumption of the compressor is measured. A minimum superheating of the working fluid of 3 °C at the suction side is targeted for all operation points to protect the compressor.

The mass flow rate, the temperature change of the water in the condenser, and the water inlet temperature of the evaporator were varied in the present work. The evaporator inlet temperature of the water into the tube-in-tube heat exchangers was varied between 8 and 29 °C. Throughout, the water mass flow rate in the evaporator was set to around 0.15 kg/s to ensure a high heat transfer. Here, it was not attempted to control the temperature change of the water. The evaporator has an inner tube diameter of 10 mm (wall thickness: 1 mm) and an inner diameter of the outer tube of 16 mm. This results in an annular gap of 2 mm in which the water flows. The evaporator has a length of 14 m. The condenser has an annular gap of 2 mm and an inner tube diameter of the outer tube of 19 mm. The condenser has a total length of 22 m. A needle valve is used for throttling in a wide range of operation points. A working fluid reservoir between the condenser and the needle valve compensates the different needed working fluid mass loads at different operation points, so the system must not be refilled for operation point changes.

A flow meter (Krohne, Optiflux 4050) measures the water mass flows in the secondary fluid cycles. The working fluid mass flow rate was determined from the energy balance in the evaporator like in previous studies on that system [40,86], which agreed within 2 % with direct flow measurements, but avoided additional pressure losses [40].

Pressure and temperature sensors provide the state information along the cycle and for the secondary fluids (1-6 in Fig. 3.1) to evaluate the process. The manufacturers, ranges and accuracies of the used pressure and temperature sensors are summarized in Table 3.2.

Table 3.2 Used sensors with manufacturer, type, measuring ranges and accuracies.

Sensor	Manufacturer	Type	Range	Accuracy
Temperature	Sensor Electric	PT-1000 type AA	-5 – 120 °C	$0.1 + 0.005 \cdot T$ [°C]
Pressure	ICS Schneider Messtechnik	IMP331	Position 1 and 5: 0 - 10 bar (absolute) Others: 0 - 25 bar (absolute)	0.1 % [of full span output][3]

The circulating working fluid mixture deviated from the targeted propane-isobutane mixture of 0.75:0.25 (molar)[4]. A method to determine the actual composition was used, which was proposed and used by different authors before [102,103]. Assuming that the expansion valve is isenthalpic, the mole fractions can be calculated iteratively until the enthalpy of the composition before and after the expansion valve is the same; fluid properties were evaluated using RefProp [101]. The variation of the secondary fluid parameters leads to a slightly varying distribution of the working fluid mixture between cycle and reservoir. Thus, for every operation point the composition was evaluated and used further, whereby the calculated mole fraction of isobutane was found to be 0.002 to 0.0353 higher than targeted. Care was taken to ensure superheating at the compressor inlet and subcooling at the condenser outlet. The secondary fluid parameter (subscript: sf) value ranges used in the experiments are shown in Table 3.3.

---

[3] This bracket was added and is, thus, deviating from the submitted manuscript.

[4] This bracket was added and is, thus, deviating from the submitted manuscript.

Table 3.3 Investigated secondary fluid parameters.

Parameter	Used values
Secondary fluid mass flow rate condenser, $\dot{m}_{\text{cond,sf}}$	1.5 – 6 kg/min
Secondary fluid temperature difference condenser, $\Delta T_{\text{cond, sf}}$	5 – 20 °C
Secondary fluid inlet temperature evaporator, $T_{\text{evap, sf, in}}$	8 – 29 °C

The highest investigated evaporator inlet temperatures are unrealistic for house heating, while hot water is also needed in summer; here it allows to vary the temperature lift between heat sink and source temperature in a wide range.

An error analysis was carried out previously for this system [86], and shall only be summarized, and some taken measures explained. Before logging in the data, it was waited until a steady operation point was reached. Furthermore, the statistical uncertainty in the fluctuating values was reduced by logging the data with 1 Hz for 10 min and using the averaged values for further evaluation. To reduce the heat losses, a polyurethane insulation of 20 mm thickness was used for the whole system. An additional stone wool insulation of 30 mm thickness was used for both heat exchangers. In addition, the statistical errors due to the uncertainties of the sensors (see Table 3.2) were analysed previously [40]. There it was shown from error propagation that the uncertainties for the various derived values are in a range between 0.18 and 3.51 %. For example, the calculated uncertainty of the compressor power consumption is 0.36 %, for the *COP* it is 2.22 % and for the specific exergy loss in the condenser it is 3.51 %. Overall, repetition measurements showed that the errors are in the same range for the present work

3.4   *Data evaluation*

The evaluation of the experimental data and the used equations shall briefly be introduced and discussed here. From the measured data and the iteratively determined mixture composition at every operation point, properties like enthalpy and entropy were directly calculated with RefProp [101].

With the known secondary fluid (subscript: sf) mass flow rate $\dot{m}_{\text{cond,sf}}$ and temperature change $\Delta T_{\text{cond,sf}}$ in the condenser (subscript: cond), the transferred heat flow rate $\dot{Q}_{\text{cond,sf}}$ can be calculated, representing the heat demand:

$$\dot{Q}_{\text{cond,sf}} = \dot{m}_{\text{cond,sf}} \cdot \Delta T_{\text{cond,sf}} \qquad \text{(Eq. 3.1)}$$

The *COP* is defined as the ratio of the determined net heat flow rate transferred to the secondary fluid in the condenser to the measured compressor (subscript: comp) power $P_{\text{comp,el}}$:

$$COP_{\text{sf}} = \frac{\left|\dot{Q}_{\text{cond,sf}}\right|}{P_{\text{comp,el}}} \qquad \text{(Eq. 3.2)}^{[5]}$$

To analyse the process details, the exergy destruction in all components is examined. These are generally determined by the difference between entering and exiting exergy flows $\dot{E}$. The exergy flow rates, when the contributions of kinetic and potential energy changes are neglected, are given by:

$$\dot{E}_i = \dot{m}_i \cdot ((h_i - h_{\text{amb}}) - T_{\text{amb}} \cdot (s_i - s_{\text{amb}})) \qquad \text{(Eq. 3.3)}$$

In this equation $\dot{m}, T, h, s$ are mass flow rate, temperature, specific enthalpy, and specific entropy, respectively. An ambient (subscript: amb) temperature of 25 °C and pressure of 1 bar were used in this work as dead state. Using Eq. 3.3, all entering and exiting exergy flows are calculated for each component and their difference is the exergy destruction.

The mass flow rate of the working fluid (subscript: wf) was determined from the energy balance across the evaporator (subscript: evap), which was assumed to be adiabatic, because of the small temperature difference to the environment [40]. Thus, the mass flow rate can be calculated from:

$$\dot{m}_{\text{wf}} = \dot{m}_{\text{evap,sf}} \cdot \frac{\left(h_{\text{evap,sf,in}} - h_{\text{evap,sf,out}}\right)}{\left(h_{\text{evap,wf,in}} - h_{\text{evap,wf,out}}\right)} \qquad \text{(Eq. 3.4)}$$

The outlet state of the compressor was used to calculate the specific work delivered to the fluid $w_{\text{comp,wf}}$ from the measured data, assuming an adiabatic compressor:

$$w_{\text{comp,wf}} = h_{\text{comp,out}} - h_{\text{comp,in}} \qquad \text{(Eq. 3.5)}$$

By using $\dot{m}_{\text{wf}}$ and $w_{\text{comp,wf}}$, $P_{\text{comp,wf}}$ was determined. Also, the specific electrical work of the compressor can be calculated by dividing $P_{\text{comp,el}}$ through the working fluid mass flow rate.

The pressure ratio π_{comp} is defined as the quotient of the outlet pressure $p_{\text{comp,out}}$ and the inlet pressure $p_{\text{comp,in}}$ of the compressor as measured in the process:

$$\pi_{\text{comp}} = \frac{p_{\text{comp,out}}}{p_{\text{comp,in}}} \qquad \text{(Eq. 3.6)}$$

---

[5] The indice of *COP* was added and is, thus, deviating from the submitted manuscript.

Various efficiencies can be defined for the compressor to characterise it. In the present work, the electro-mechanical (subscript: em) compressor efficiency $\eta_{comp,em}$ is used with:

$$\eta_{comp,em} = \frac{P_{comp,wf}}{P_{comp,el}} = \frac{\dot{m}_{wf}\left(h_{comp,out} - h_{comp,in}\right)}{P_{comp,el}} \qquad \text{(Eq. 3.7)}$$

It represents the ratio of the power delivered to the working fluid $P_{comp,wf}$ and $P_{comp,el}$, thus considering the electro-mechanical losses in the compressor.

The isentropic efficiency (subscript: is) is defined as the ratio of the isentropic compressor power $P_{comp,is}$ and $P_{comp,el}$:

$$\eta_{comp,is} = \frac{P_{comp,is}}{P_{comp,wf}} = \frac{w_{comp,is}}{w_{comp,wf}} \qquad \text{(Eq. 3.8)}$$

The specific isentropic work $w_{comp,is}$ is calculated using the isentropic enthalpy $h_{comp,out,is}$ for the outlet enthalpy in Eq. 3.5. With $\eta_{comp,em}$ and $\eta_{comp,is}$, the total efficiency $\eta_{comp,total}$ is calculated:

$$\eta_{comp,total} = \eta_{comp,em} \cdot \eta_{comp,is} \qquad \text{(Eq. 3.9)}$$

3.5   *Discussion and results*

Heat demands in buildings vary, which in turn leads to varying heat flows to the water in the condenser. According to Eq. 3.1. the adjustment of the heat flow could either be achieved by adapting the circulating water mass flow rate or by a different temperature change (or both). In the following, the case of varying the mass flow rate between 2 and 4.5 kg/min will be considered first, while the temperature change $\Delta T_{cond, sf}$ was held constant at 10 °C with an inlet temperature of 60 °C. Also, the evaporator water inlet temperature $T_{evap,sf,in}$ was constant at 20 °C.

3.5.1 Variation of the mass flow rate in the condenser

First, two strongly differing conditions shall be discussed along their temperature vs. enthalpy flow rate diagrams. In Fig. 3.2 the resulting states for $\dot{m}_{cond,sf}$ of 2 and 4.5 kg/min are shown.
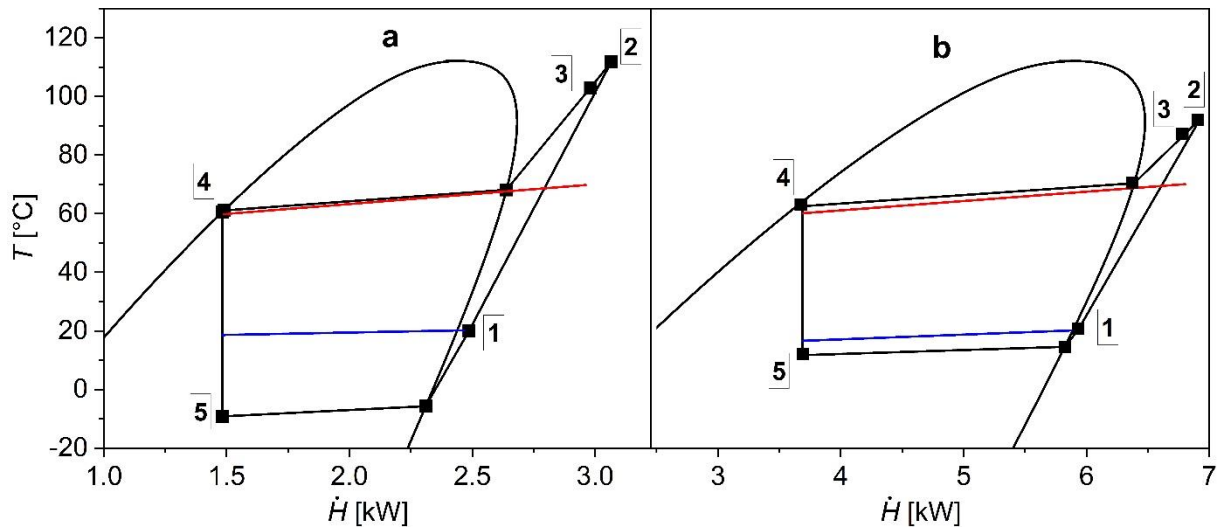
Fig. 3.2 *T-$\dot{H}$* diagrams for a) $\dot{m}_{cond,sf}$ = 2 kg/min and b) $\dot{m}_{cond,sf}$ = 4.5 kg/min with condenser water inlet temperature 60 °C, $\Delta T_{cond,\,sf}$ = 10 °C and $T_{evap,sf,in}$ = 20 °C.

The cycle is plotted in black, the evaporator water states are shown in blue, and the prescribed water states in the condenser are plotted in red. The numbered states between the main components (see Fig. 3.1) are marked with black dots.

      The changes in mass flow rate lead to heat flow rates of 1.4 kW and 3.14 kW, thus, quite different heat loads, as seen from the diagram. The cycle has to be adapted to the different loads, here by changing the throttling valve opening, and thus, the working fluid mass flow rate.

      Comparing the two diagrams shows that the temperature difference between the secondary fluid and working fluid in the evaporator for the higher mass flow rate (3.2-b) is significantly lower than for the low mass flow rate case, although the boundary conditions for the water in the evaporator were the same for both. This results in a lower superheating of the working fluid at state 1 for 3.2-b. Additionally, the temperature at the compressor exit (state 2) is lower, 92.51 °C for 2-b compared to 111.76 °C for 3.2-a. Some heat loss (below 90 W) occurs between the compressor exit and the condenser entrance of the working fluid (state 3). At first sight, one could think that the overall heat transfer coefficient dropped strongly in the evaporaor. But since state 4 is unchanged between both cases, and especially the enthalpy and temperature are identical for state 1, it is clear that the heat transfer is not limiting: the secondary inlet temperature is nearly reached by the exiting working fluid. Instead, the relation between throttling, mass flow rate, and pressure drop is responsible for the difference. This large mean temperature difference directly leads to larger exergy losses. The same holds for the

superheating, which leads to larger exergy losses at low mass flow rates. The quantitive evaluation will follow.

To further examine this difference, the energy flow rates in the evaporator $\dot{Q}_{\text{evap}}$, condenser $\dot{Q}_{\text{cond,sf}}$, and compressor $P_{\text{comp,el}}$, along with the working fluid mass flow rate $\dot{m}_{\text{wf}}$, are plotted in Fig. 3.3.
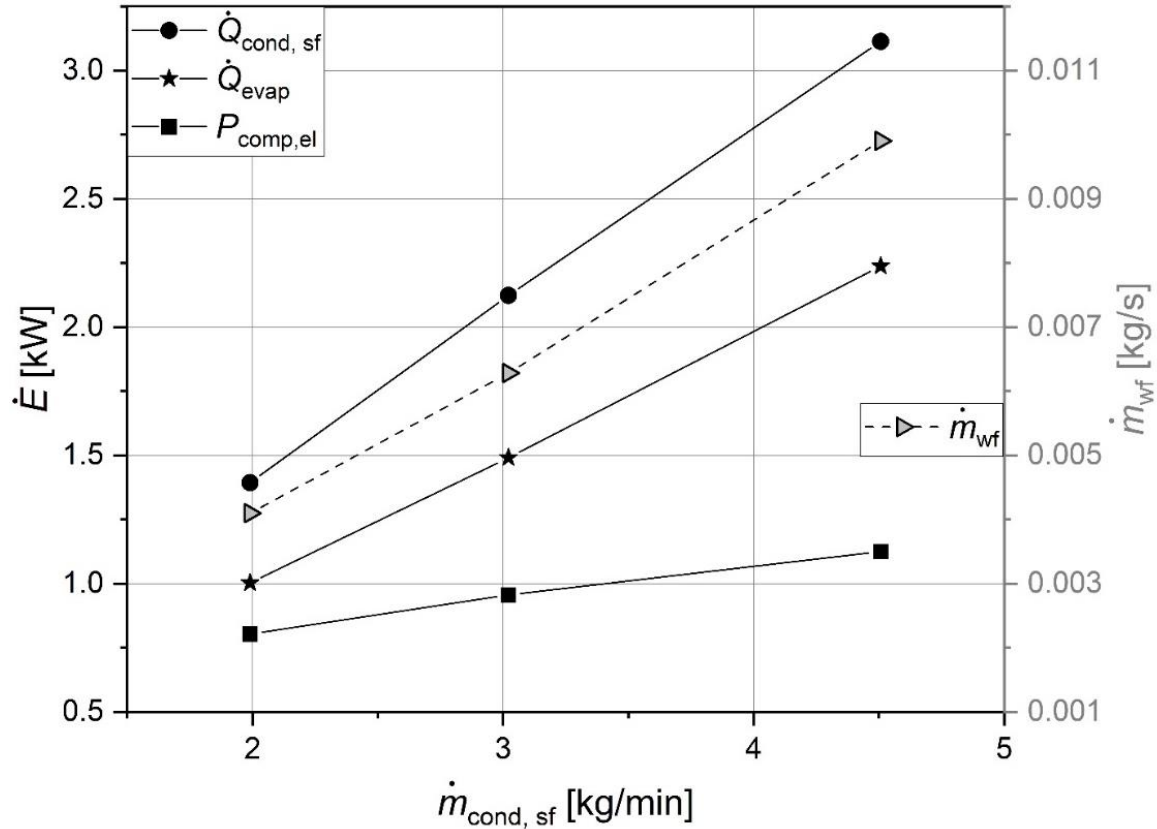
Fig. 3.3 Energy flow rates for secondary fluid in the condenser $\dot{Q}_{\text{cond,sf}}$, for evaporator $\dot{Q}_{\text{evap}}$ and the compressor $P_{\text{comp,el}}$ on left y-axis as a function of $\dot{m}_{\text{cond,sf}}$. Working fluid mass flow rate $\dot{m}_{\text{wf}}$ on right y-axis. Condenser water inlet temperature 60 °C, $\Delta T_{\text{cond, sf}} = 10$ °C and $T_{\text{evap,sf,in}} = 20$ °C.

In Fig. 3.3, the left y-axis displays the heat flow rates onto the secondary fluid in the condenser (circles) and in the evaporator (stars), as well as the electrical compressor power (squares). The right y-axis represents the working fluid mass flow rate (triangles). As $\dot{m}_{\text{cond,sf}}$ increases, all energy flow rates, as well as $\dot{m}_{\text{wf}}$, increase. The heat flow rates and $\dot{m}_{\text{wf}}$ exhibit an approximately proportional increase with $\dot{m}_{\text{cond,sf}}$, while $P_{\text{comp,el}}$ increases less steeply. The latter indicates that the specific enthalpy change in the compressor gets smaller with the mass

flow rate (or the load), as is deduced from Eq. 3.7 $\left(\left(h_{comp,out} - h_{comp,in}\right) = \frac{P_{comp,el}}{\eta_{comp,em} \cdot \dot{m}_{wf}}\right)$ leading to lower exit temperatures for the same inlet enthalpy with larger mass flow rates.

A reason for this lower increase of $P_{comp,el}$ with load is due to the throttling relation between $\dot{m}_{wf}$, pressure, and load. Low mass flow rates lead to larger pressure drops in the expansion valve (15.6 compared to 14 bar), while the entrance pressure is only slightly increasing (18.1 to 19 bar), leading to lower temperatures in the two-phase regime for the low mass flow rate. This can also be observed in the different temperature difference between states 4 and 5 (before and after the expansion valve) in Fig. 3.2 when comparing (a) and (b). The pressures levels at the compressor inlet $p_{comp,in}$ and outlet $p_{comp,out}$ are plotted in Fig. 3.4 on the left axis, together with the pressure ratio π_{comp} on the right axis.
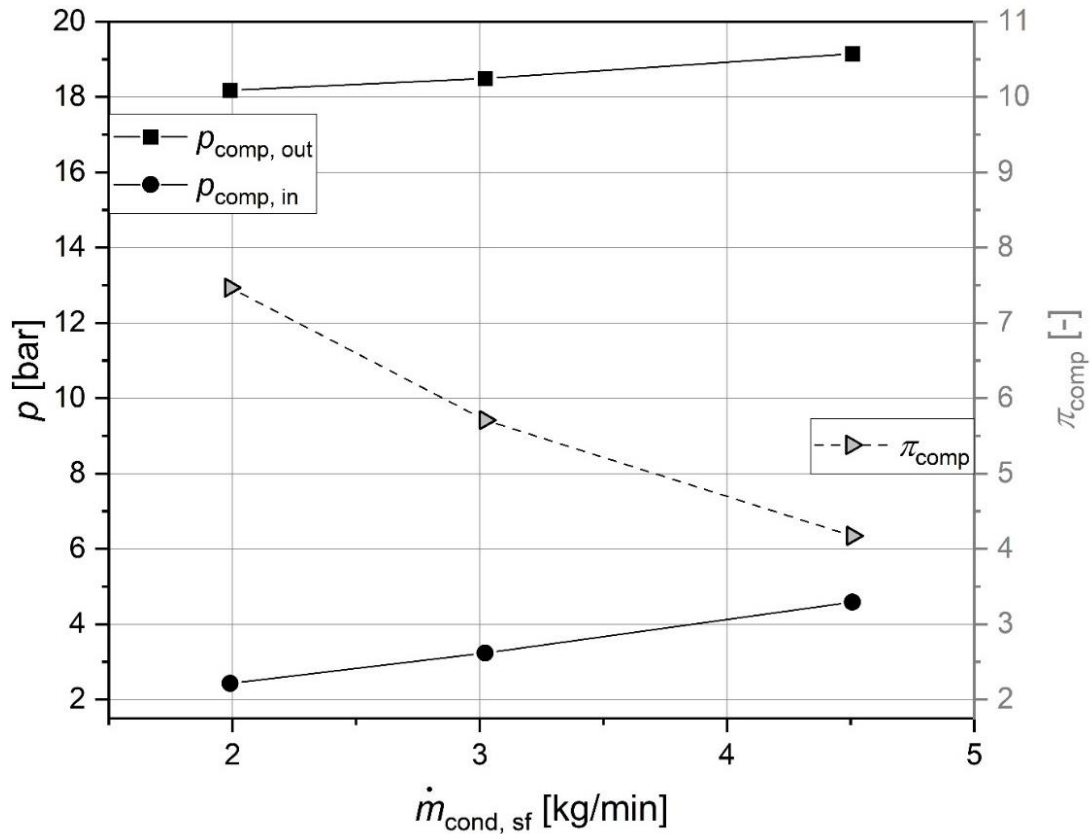
Fig. 3.4 Pressure before ($p_{comp,in}$, state 1) and after ($p_{comp,out}$, state 2) the compressor on left y-axis, pressure ratio π_{comp} on right y-axis; both as a function of $\dot{m}_{cond,sf}$. Condenser water inlet temperature 60 °C, $\Delta T_{cond,sf} = 10$ °C and $T_{evap,sf,in} = 20$ °C.

The inlet pressure increases by 88.9 %, while the outlet pressure increases only by 5.3 % between 2 and 4.5 kg/min water mass flow rate, and π_{comp} decreases by 79.1 % in the considered range. Lower pressure ratios reduce the forces in the compressor, leading to higher

amounts of power transferred to the fluid ($P_{comp,wf}$). It is shown in Fig. 3.5 as stars along with the electrical power $P_{comp,el}$ (circles) and the power needed for an isentropic compression $P_{comp,is}$ (dots).
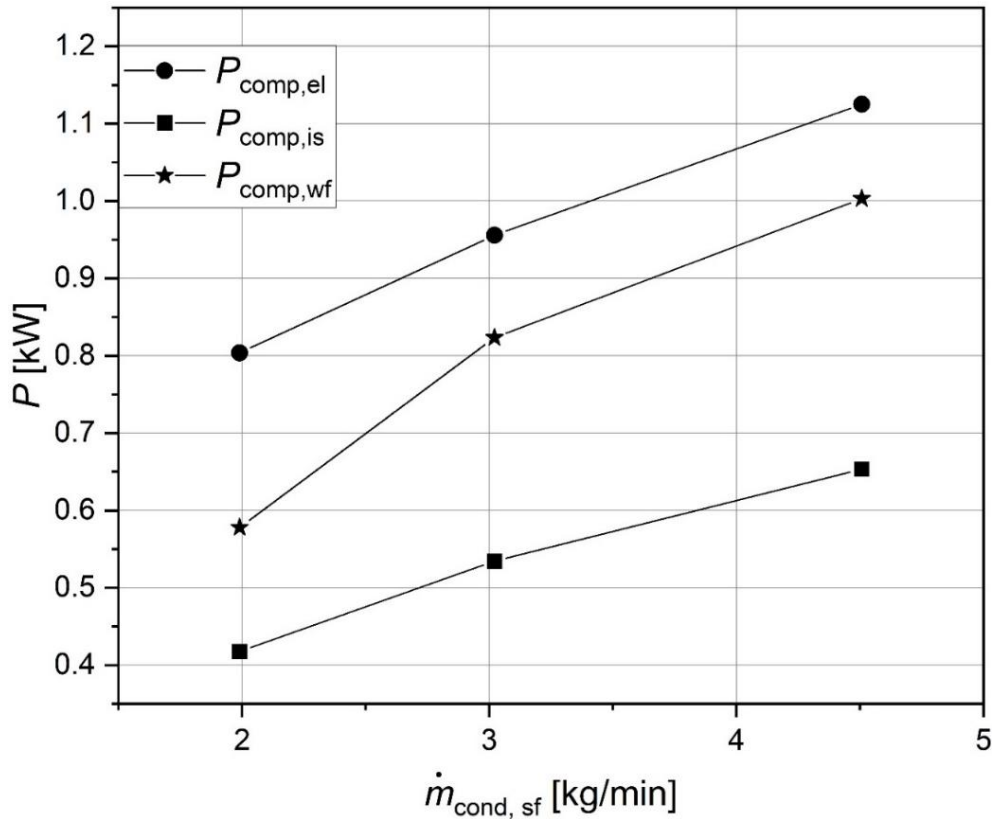
Fig. 3.5 Electrical compressor power $P_{comp,el}$, power delivered to the working fluid $P_{comp,wf}$ and isentropic power $P_{comp,is}$ as a function of $\dot{m}_{cond,sf}$. Condenser water inlet temperature 60 °C, $\Delta T_{cond,\,sf} = 10$ °C and $T_{evap,sf,in} = 20$ °C.

Most noticeable is the increase in $P_{comp,wf}$ from 0.578 to 0.823 kW when increasing the mass flow rate from 2 to 3 kg/min, representing a 42.4 % higher power. The electrical power only increases by 19.1 % from 0.803 to 0.956 kW. The stronger increase of $P_{comp,wf}$ indicates an improving efficiency of the compressor. Obviously, some power is needed to drive the compressor, even for small or nearly negligible loads, leading to an offset, which is unfavourable for small mass flow rates. In contrast, the power for an isentropic compressor increases moderately by 28 %.

To illustrate this effect on compressor efficiencies, Fig. 3.6 shows the total $\eta_{comp,total}$ (square), electro-mechanical $\eta_{comp,em}$ (circle), and isentropic efficiency $\eta_{comp,is}$ (star) of the compressor.
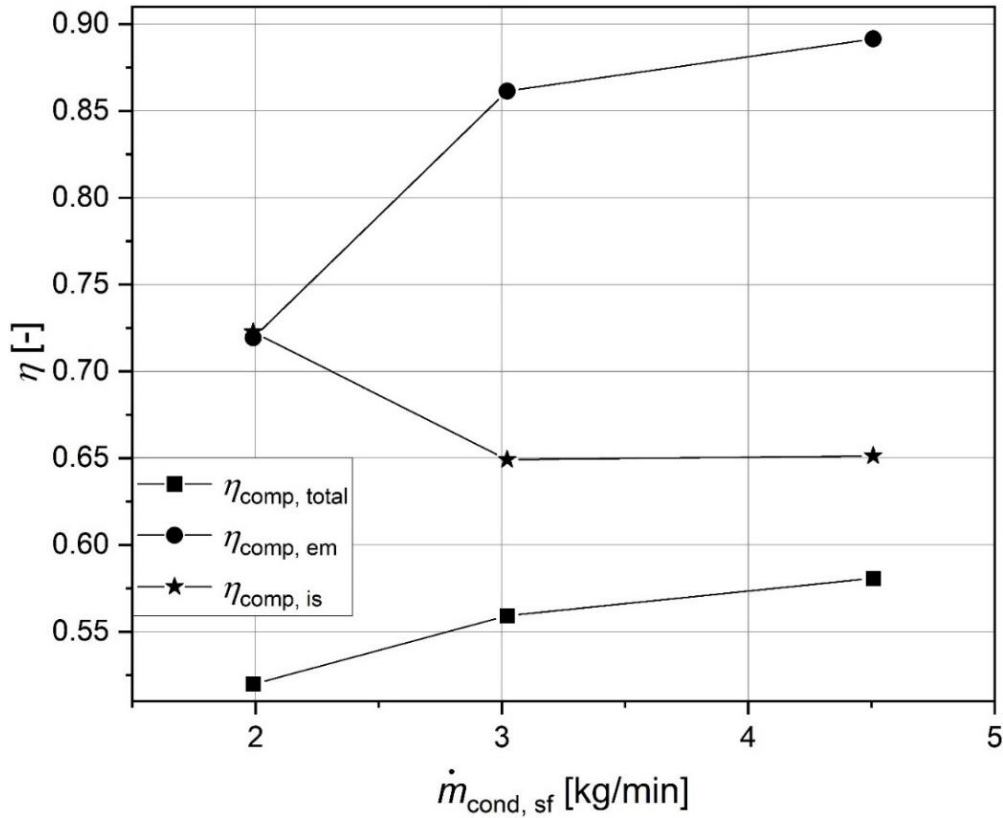
Fig. 3.6 Total ($\eta_{comp,total}$), electro-mechanical ($\eta_{comp,em}$) and isentropic ($\eta_{comp,is}$) compressor efficiencies as a function of $\dot{m}_{cond,sf}$. Condenser water inlet temperature 60 °C, $\Delta T_{cond,\,sf} = 10$ °C and $T_{evap,sf,in} = 20$ °C.

Over the investigated range, there is a 24.06 % increase in the electromechanical efficiency $\eta_{comp,em}$, from 0.719 to 0.892 with a larger increase between the first points due to the marked higher proportion of $P_{comp,wf}$ (Fig. 3.5.). In contrast, there is a slight decrease of 9.46 % in the isentropic efficiency $\eta_{comp,is}$. At last, resulting from the electro-mechanical and isentropic efficiency in Eq. 3.9 ($\eta_{comp,total} = \eta_{comp,em} \cdot \eta_{comp,is}$), an increase in total efficiency from 0.519 to 0.581 (11.89 %) with mass flow rate is measured overall.

Fig. 3.7 shows the fate of the specific exergy (per mass of working fluid) entering the heat pump, basically from the electrical work transferred to the compressor $w_{comp,el}$. This specific exergy is either transferred to the condenser water $e_{cond,sf}$ or destructed in the main components; their distribution is enlightening.
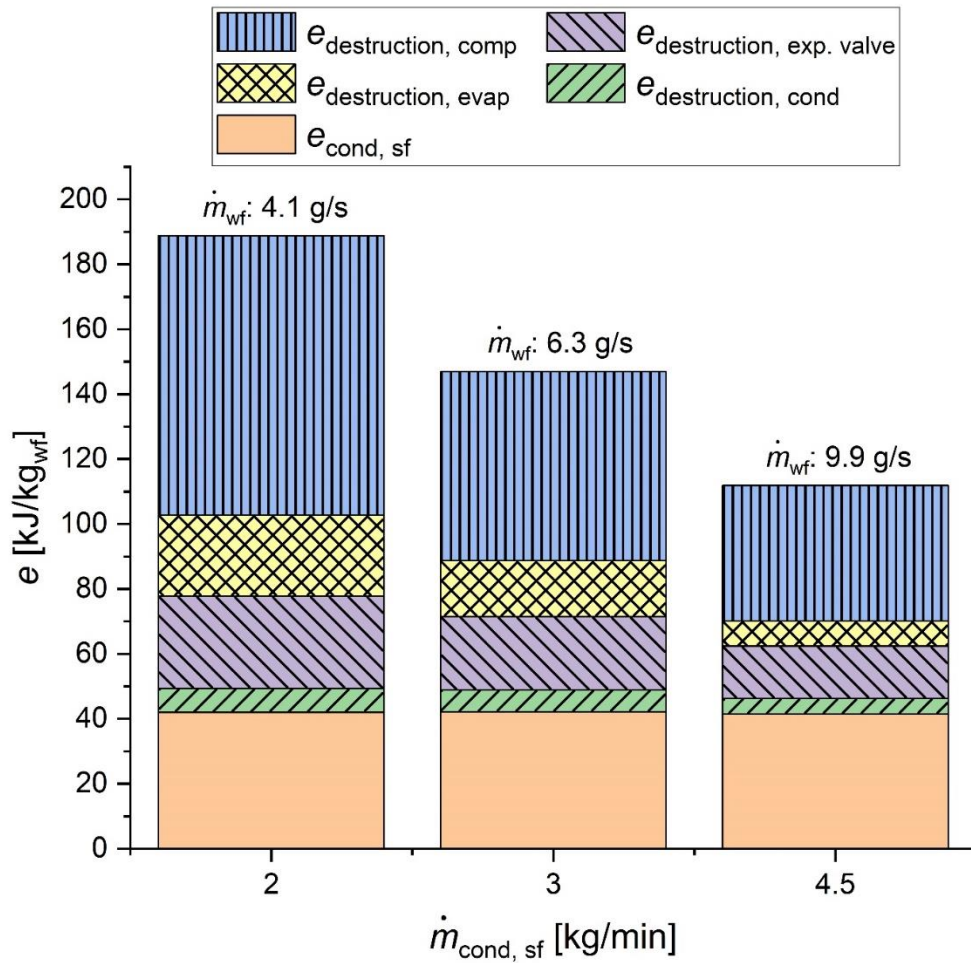
Fig. 3.7 Specific working fluid exergy added to the system and its fate as a function of secondary fluid flow rate. The specific exergy transferred in the condenser and the specific exergy destruction in the compressor, expansion valve, evaporator, and condenser are shown as a function of $\dot{m}_{cond,sf}$. Condenser water inlet temperature 60 °C, $\Delta T_{cond,\,sf} = 10$ °C and $T_{evap,sf,in} = 20$ °C.

The exergy transferred to the heat sink per mass of working fluid in orange $e_{cond,sf}$ is nearly constant with 42 kJ/kg, due to the constant conditions in the condenser, while the remaining exergy added to the working fluid is destructed, with the amount reduced from 146 to 70 kJ/kg with increasing heat loads as seen from the hatched parts.

As seen previously [39,40,86,105] the compressor proves to be the component with the highest individual exergy destruction, accounting for 43.3 % of the destruction of the entering exergy at 2 kg/min and reduced to 34.4 % at 4.5 kg/min. It is followed by the expansion valve and the evaporator, all decreasing with the mass flow rate. In the evaporator, the exergetic losses decrease by 68.94 % from 24.95 to 7.75 kJ/kg, due to the decreasing temperature difference

between working and secondary fluid resulting from a rising evaporation temperature and decreasing superheating. The throttling at low mass flow rates ends at high vapor qualities, which is reduced with increasing mass flow rates, leading to lower losses. The condenser contributes around 6 % to the total exergy destruction and remains nearly constant, due to the maintained temperature levels for the secondary fluid, resulting in minimal changes in the temperature difference between the fluids (see Fig. 3.2). This decrease of losses in almost all components leads to the noticeable reduction in total exergy destruction and $w_{\text{comp,el}}$.

As a result, the COP increases with the mass flow rate, as shown in Fig. 3.8, while the COP_{carnot} ($COP_{\text{carnot}} = T_{\text{cond,sf,out}} / T_{\text{lift}})^6$ for a reversible process would stay constant (plotted as squares in the diagram).
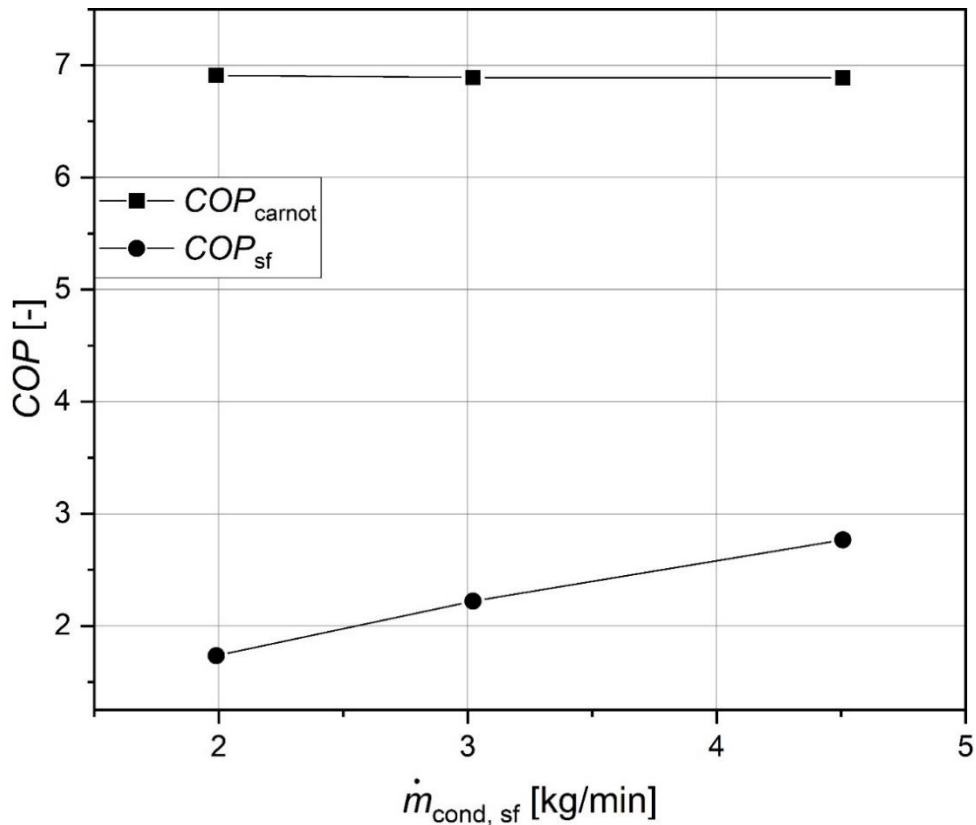
Fig. 3.8 Ideal and experimentally measured *COP* as a function of $\dot{m}_{\text{cond,sf}}$ for a condenser water inlet temperature 60 °C, $\Delta T_{\text{cond, sf}} = 10$ °C and $T_{\text{evap,sf,in}} = 20$ °C.

The reversible *COP* of 6.9 does not depend on the load while the COP_{sf} values significantly increase by 63.4 % from 1.73 (2 kg/min) to 2.77 (4.5 kg/min). The measured COP_{sf} is 25.1 %

---

[6] This bracket was added and is, thus, deviating from the submitted manuscript

of the ideally achievable value at 2 kg/min, while it is 40.2 % at 4.5 kg/min. Thus, higher loads are preferrable if mass flow rates are changed for adaptation.

3.5.2 Variation of the condenser water temperature change

From Eq. 3.2 it is clear that $\Delta T_{\mathrm{cond,sf}}$ can also be adapted to adjust the heat demand $\dot{Q}_{\mathrm{cond,sf}}$ at constant secondary fluid mass flow rates, being an alternative to a variation of $\dot{m}_{\mathrm{cond,sf}}$. This variation should be addressed next, by varying $\Delta T_{\mathrm{cond,sf}}$ between approximately 5 and 15 °C with an inlet temperature of 60 °C, while keeping $\dot{m}_{\mathrm{cond,sf}}$ constant at 3 kg/min and $T_{\mathrm{evap,sf,in}}$ at 20 °C. The experimental values for $\Delta T_{\mathrm{cond,sf}}$ are not exactly 5 °C, 10 °C and 15 °C, but will be called so in the following discussion for simplicity.

As above, the working fluid mass flow rate increases with the heat demand, which is accomplished by reduced throttling, which in turn leads to an increased compressor efficiency, as discussed before. To show this, Table 3.4 summarizes several values for 5 °C, 10 °C and 15 °C.

Table 3.4 Condenser heat flow $\dot{Q}_{\mathrm{cond,sf}}$, electrical compressor power $P_{\mathrm{comp,el}}$, the COP_{sf}, working fluid mass flow rate $\dot{m}_{\mathrm{wf}}$, inlet $p_{\mathrm{comp,in}}$ and outlet $p_{\mathrm{comp,out}}$ pressure of the compressor, pressure ratio π_{comp} and the compressor efficiencies η_{comp} for $\Delta T_{\mathrm{cond,sf}}$ of 5 °C, 10 °C and 15 °C. Condenser water inlet temperature 60 °C, $\dot{m}_{\mathrm{cond,sf}}$ = 3 kg/min and $T_{\mathrm{evap,sf,in}}$ = 20 °C.

Parameter	Unit	5 °C	10 °C	15 °C
$\dot{Q}_{\mathrm{cond,sf}}$	[kW]	1.17	2.17	3.27
$P_{\mathit{comp,el}}$	[kW]	0.75	0.99	1.23
COP_{sf}	[-]	1.55	2.20	2.66
$\dot{m}_{\mathrm{wf}}$	[kg/s]	0.00357	0.00686	0.01159
$p_{\mathrm{comp,in}}$	[bar]	2.23	3.42	5.26
$p_{\mathrm{comp,out}}$	[bar]	17.19	18.48	20.73
π_{comp}	[-]	7.70	5.40	3.94
$\eta_{\mathrm{comp,em}}$	[-]	0.697	0.830	0.849
$\eta_{\mathrm{comp,is}}$	[-]	0.716	0.687	0.695
$\eta_{\mathrm{comp,total}}$	[-]	0.499	0.571	0.590

With the increase of $\Delta T_{\mathrm{cond,sf}}$ from 5 to 15 °C, the heat flow $\dot{Q}_{\mathrm{cond,sf}}$ increases by a factor of 2.8, while the compressor power only increases by 64 %, which leads to an COP_{sf} increase by

71.6 %. Also, with the higher mass flow rate, the pressure levels before and after the compressor increase, due to reduced throttling. Although the pressure difference remains constant, the increased pressure levels lead to a significant variation in the pressure ratio π_{comp}. It halves from 7.58 to 3.88 and contributes to the higher $\eta_{comp,em}$. Altogether, this results in lower exergetic losses in the compressor and higher COP_{sf}, which are shown in Fig. 3.9 together with the COP_{carnot} for the reversible process.
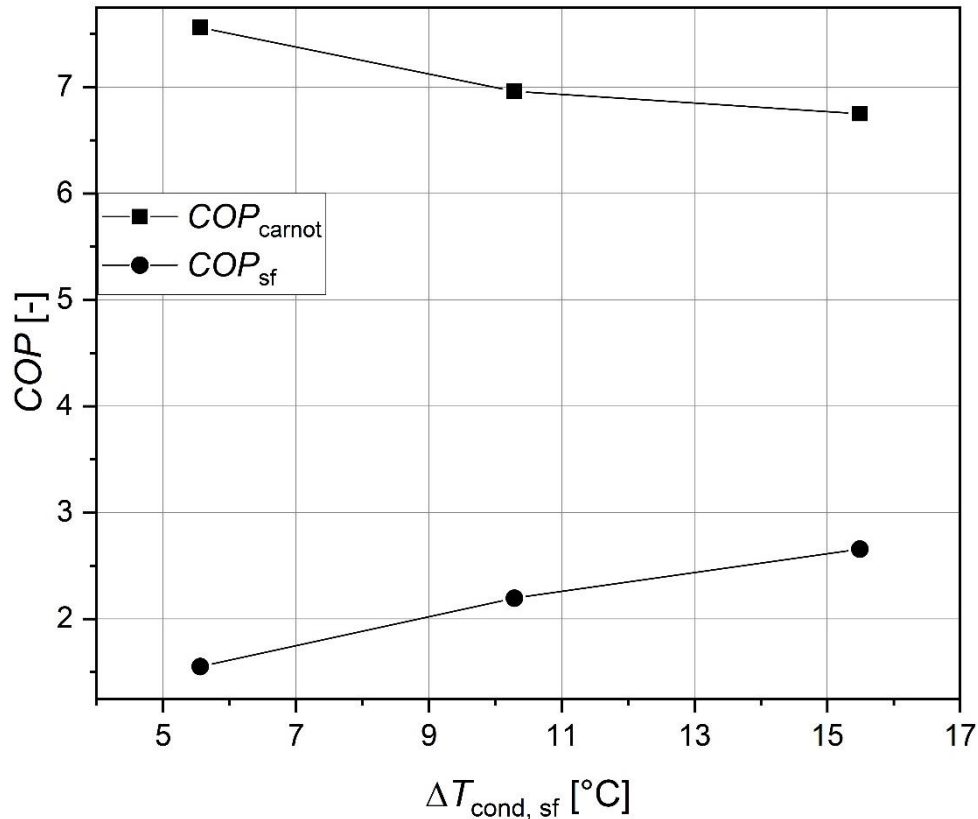
Fig. 3.9[7] Ideal and experimentally measured COP as a function of $\Delta T_{cond,sf}$ with condenser water inlet temperature 60 °C, $\dot{m}_{cond,sf} = 3$ kg/min and $T_{evap,sf,in} = 20$ °C.

The reversible COP_{carnot} decreases by 10.7 % with $\Delta T_{cond,sf}$ from 5 to 15 °C, because the mean temperature of the secondary fluid also increases, while the experimental COP_{sf} increases with $\Delta T_{cond,sf}$ from 1.55 to 2.66, corresponding to an increase of 71.6 %. Thus, COP_{sf} achieves 20.5 % at 5 °C and 39.4 % at 15 °C of the reversible COP_{carnot}. Consequently, the higher heat load with increasing $\Delta T_{cond,sf}$ is preferrable as for the variation of $\dot{m}_{cond,sf}$.

Sections 4.1 and 4.2 can be summarized as follows: The variation in $\dot{Q}_{cond,sf}$ primarily influences the working fluid mass flow rate. Since this is mainly achieved by changing the

---

[7] The legend of this diagram was corrected and is, thus, deviating from the submitted manuscript.

throttling, the process pressure levels are affected, altering the operational behaviour of the crucial component, the compressor. The comparison of ideal and measured *COPs* shows that the influence of the secondary fluid parameters outweighs the expected change in *COP* from theory.

3.5.3 Variation of the evaporator water inlet temperature

After analysing the secondary fluid influence in the condenser, the evaporator is investigated now. The most significant variable here is the heat source temperature, which, in practice, corresponds to a change in the outside or source temperature.

Here, evaporator inlet temperatures ranging from 8 to 29 °C were investigated, whereby the highest temperatures are not of interest for domestic house heating, but e.g. for warm water production. For this temperature range, $\dot{Q}_{cond,sf}$, $P_{comp,el}$ and $\dot{m}_{wf}$ are plotted in Fig. 3.10, with a constant condenser water inlet temperature of 50 °C and $\Delta T_{cond,sf}$ of 15 °C. To maintain the boundary condition of $\Delta T_{cond,sf}$ of 15 °C in this variation and to achieve working fluid superheating at the compressor inlet, $\dot{m}_{cond,sf}$ had to be reduced to 2.7 kg/min (11 and 14 °C) and 2.4 kg/min (8 °C), due to the fixed evaporator heat transfer area.
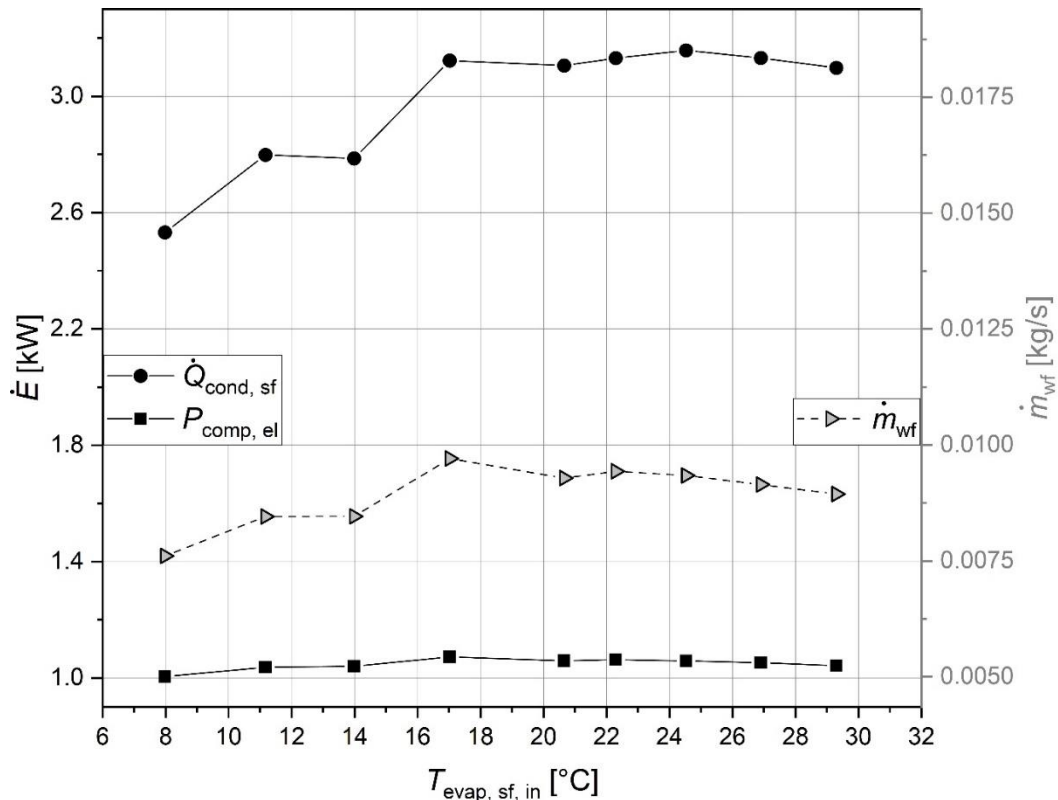
Fig. 3.10 Heat flow rate $\dot{Q}_{cond,sf}$ and electrical compressor power $P_{comp,el}$ on left y-axis as a function of $T_{evap,sf,in}$. Working fluid mass flow rate $\dot{m}_{wf}$ on right y-axis. Condenser water inlet temperature 50 °C and $\Delta T_{cond,\,sf} = 15$ °C.

It is seen that energy and mass flow rates mainly change until 17 °C, while there are only slight variations at higher temperatures. Compared to the previous series, the range of mass flow rates remains within 10 % of the average value. Results are summarized in Table 3.5 for 8, 17 and 29 °C.

Table 3.5 Condenser heat flow $\dot{Q}_{cond,sf}$, electrical compressor power $P_{comp,el}$, the COP_{sf}, working fluid mass flow rate $\dot{m}_{wf}$, inlet $p_{comp,in}$ and outlet $p_{comp,out}$ pressure of the compressor and pressure ratio π_{comp} along the temperature $T_{comp,in}$ and superheating $T_{superheat}$ for the compressor inlet for $T_{evap,sf,in}$ of 8, 17, and 29 °C. Condenser water inlet temperature 50 °C and $\Delta T_{cond,\ sf} = 15$ °C.

Parameter	Unit	8 °C	17 °C	29 °C
$\dot{Q}_{cond,sf}$	[kW]	2.53	3.12	3.10
$P_{comp,el}$	[kW]	1.00	1.07	1.04
COP_{sf}	[-]	2.52	2.91	2.97
$\dot{m}_{wf}$	[kg/s]	0.00761	0.00971	0.00894
$p_{comp,in}$	[bar]	3.66	4.34	4.04
$p_{comp,out}$	[bar]	17.23	17.39	16.96
π_{comp}	[-]	4.70	4.01	4.20
$T_{comp,in}$	[°C]	7.05	16.30	28.98
$T_{superheat}$	[°C]	2.80	6.59	21.30

It is seen that the condenser heat flow rate is nearly constant for 17 and 29 °C and 19 % lower for 8 °C. The compressor power is barely affected by $T_{evap,sf,in}$ and remains within 5 % around 1.04 kW. Consequently, the COP_{sf} is 13.4 % lower for 8 °C. The mass flow rate and both pressures go through a slight maximum at 17 °C, while the pressure ratio has a minimum at this temperature. The temperature levels at the compressor inlet $T_{comp,in}$ and $T_{superheat}$ increase monotonically. The compressor inlet pressure only changes slightly, which also holds for the evaporation temperature. Thus, a higher $T_{comp,in}$, due to the increasing secondary fluid temperature $T_{evap,sf,in}$, results in a higher superheating (6.59 to 21.30 °C), increasing the temperature difference between the working fluid and the secondary fluid in the evaporator; a higher exergy destruction follows as seen in Fig. 3.11.
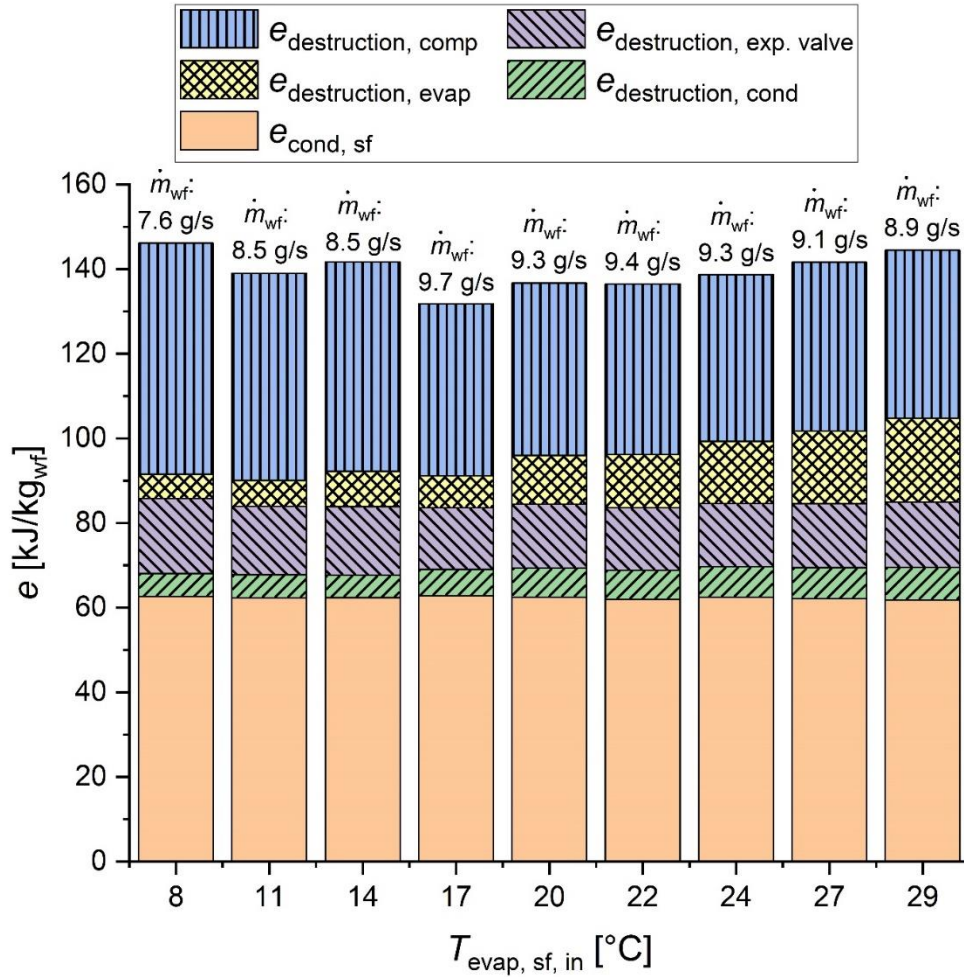
Fig. 3.11 Specific working fluid exergy added to the system and its fate as a function of $T_{evap,sf,in}$. The specific exergy transferred in the condenser and the specific exergy destruction in the compressor, expansion valve, evaporator, and condenser are shown as a function of $T_{evap,sf,in}$. Condenser water inlet temperature 50 °C and $\Delta T_{cond, sf} = 15$ °C.

Here, the sum of the hatched parts in the bars also illustrates the share $e_{destruction,total}$ of the specific working fluid exergy added to the system, which is basically $w_{comp,el}$. From Fig. 3.11 it is recognized that basically two opposite trends counteract, the evaporator's share of the total exergy destruction increases from ca. 5 to 20 kJ/kg to 24 % with $T_{evap,sf,in}$, which is compensated by a reduction of the compressor losses from 55 to 40 kJ/kg. At a lower level, the exergy destruction in the throttle is reduced slightly with evaporator temperature, while the condenser values rise. Both, being indirectly influenced by the evaporator temperatures via the pressure levels and pressure ratios. The total exergy destruction and $w_{comp,el}$ remains relatively constant with a minimum at 17 °C.

The resulting COP_{sf} (left y-axis, circles) and COP_{carnot} (right y-axis, dots) for this variation are plotted in Fig. 3.12.
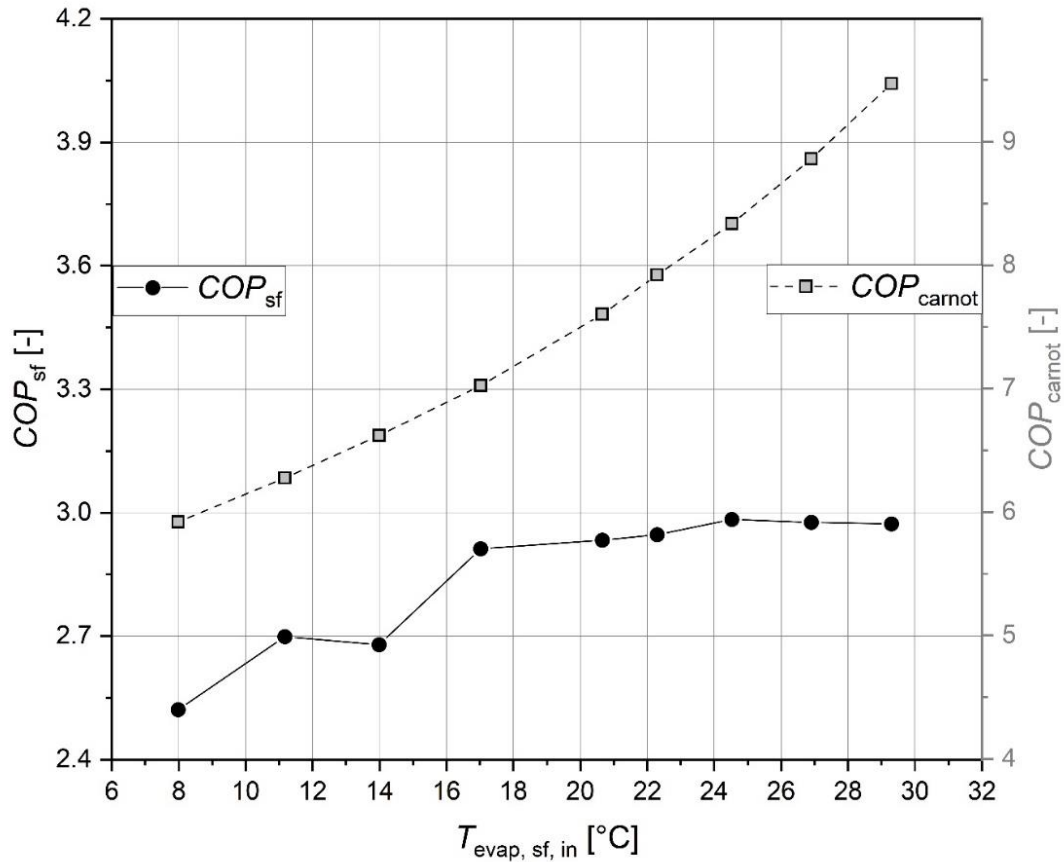
Fig. 3.12 Experimentally measured (left y-axis) and ideal (right y-axis) *COP* as a function of $T_{evap,sf,in}$ with condenser water inlet temperature 50 °C and $\Delta T_{cond,sf} = 15$ °C.

For constant heat rejection temperatures, the reversible COP_{carnot} rises with the temperature levels in the evaporator, because temperature lift is reduced. The COP_{sf} values remain nearly constant in a range of 2.91 to 2.98, with an average of 2.95 for temperatures above 17 °C, with lower values between 8 and 14 °C. For 11 and 14 °C, COP_{sf} values of about 2.7 are approximately 10 % lower; for 8 °C, it is 2.52 and 14.6 % lower. All in all, the results for the evaporator parameter variation support the previous findings that the main influence of the secondary fluid parameters are primarily via the compressor conditions, while the heat exchanger exergy destruction rates are minor here. The compensation of the increasing exergy destruction in the evaporator by reduced exergy losses in the compressor nicely emphasises the importance of the system coupling.

3.6   Conclusion

Experimental results for the influence of the secondary fluid parameters on the performance of a water-water compression heat pump system with higher temperature levels are presented. A piston compressor and a fixed working fluid mixture of isobutane and propane (0.25:0.75; molar[8]) was used. The temperature level for the secondary side of the condenser outlet was 60 to 75 °C. These temperature levels are common for conventional heating systems in houses and also for warm water production, but then the water to be heated would enter at lower temperatures. Heat source temperature levels in the range of 8 to 29 °C were investigated. The performance was evaluated as a function of the mass flow rate and temperature change of the water in the condenser and the water inlet temperature of the evaporator to simulate different heating system scenarios on the test system, especially with respect to heat demand. The heat pump cycle was adapted to the different conditions by changing the throttling, which influences mass flow rate and pressure levels, and thus the operation conditions for each part.

Such zeotropic mixtures are used to reduce the entropy production in the heat exchangers, especially in the condenser. Whether this goal is achieved, also depends on the adaptation of the secondary fluid temperature change and mass flow rate. But if the heat demand varies, again both strategies can be followed, with respect to the secondary fluid, either its mass flow rate can be varied or its temperature change. In both cases the cycle must react, mainly with varying working fluid mass flow rates, which also change the pressure levels and state points. In the present work, this was accomplished by varying the throttling process, alternatively the compressor frequency could be adapted, or storages could be used.

On the condenser side, the heat flow rate is the first determinant, while the variation of the evaporator water inlet temperature demonstrated that the increasing evaporator entropy production with higher temperatures and the increasing compressor efficiency just compensated each other here. The rising water inlet temperatures only resulted in higher superheating and thus exergy destruction in the evaporator, because the working fluid mass flow rate, and consequential, the pressure level and evaporation temperature were not affected.

The adaptation of the working fluid mass flow rate to adapt to a variation in heat demand generally influences the pressure levels and the operation points, respectively the efficiency, of the compressor. This coupling leads to dependencies, beyond the tendencies deduced from

---

[8] This word was added and is, thus, deviating from the submitted manuscript.

reversible cycles or simple cycle calculations with constant efficiencies, which have to be kept in mind and taken to account in the design process. The main difficulty is that these dependencies are normally not provided by the compressor companies, necessitating experimental work. For the investigated system, it appears that within a limited range, a variation of the heat demand by varied throttling is acceptable, but for larger ranges, either a reduced compressor speed or a thermal energy storage, charged with the heat pump running at high speed seems more favourable than strong throttling.

Chapter 4

Heat flux in latent thermal energy storage systems: the influence of fins, thermal conductivity and driving temperature difference

The content of this chapter was published in [121]:

J. Quenel and B. Atakan. Heat flux in latent thermal energy storage systems: the influence of fins, thermal conductivity and driving temperature difference. *Heat and Mass Transfer Volume 58, pages 2085–2096, (2022).* DOI: *10.1007/s00231-022-03220-3*.

Table 4.1 Author contributions for the paper following the CRediT author statement methodology [87].

Category	Quenel	Atakan
Conceptualization	X	X
Methodology	X	
Software	X	X
Validation	X	
Formal analysis	X	
Investigation	X	
Resources		X
Data Curation	X	
Writing - Original Draft	X	
Writing - Review & Editing	X	X
Visualization	X	
Supervision		X
Project administration		X
Funding acquisition		X

Author contributions to this paper

My contribution embraced developing the concept, modelling the computer code, conducting the data analysis, visualization and writing the manuscript. Burak Atakan developed concepts, parts of the initial code and reviewed the results as well as the manuscript.

Introduction and key results of the third paper

The results of the investigated secondary fluid parameters showed that the performance of the heat pump is significantly reduced when it's regulated by strong throttling. With thermal energy storages this could be avoided when the excess energy is used to charge the storage instead of reducing the output of the heat pump. Unfortunately, the promising latent storages tend to have low heat flow rates because most PCM suffer from low thermal conductivity, which is addressed in the literature with heat transfer enhancement methods. However, the detailed investigation of the heat flux change within operation time differentiated by the methods has not been carried out very often previously. Furthermore, the examination whether the enhancement of the heat flux is proportional to the parameter changes within the method is rare. Consequently, these questions are discussed in this work to enable a better evaluation of the latent storage usage in such application cases.

To investigate this, a discharge simulation based on FiPy [122] for a rectangular storage with PCM and fins is carried out. The fin volume fraction, the thermal conductivity of the PCM and the driving temperature gradient is varied and the trend of the heat flux as a function of the discharge time is discussed. The novel dimensionless heat flux M is introduced and aims to illustrate the relation of the heat flux to the driving temperature gradient, the thermal conductivity, and the characteristic length respectively. Thus, the M-level can be used to conclude whether the increasing heat flux is proportional compared to changed discharge parameters.

Overall, some key results of this work can be shortly summarized as follows:

-   The heat flux dropped steeply within the first few minutes of discharging attributable to the insulation of the first layer of solidified PCM.
-   Increasing fin volume fraction was found to be less effective, because the discharge time reduction will be outweighed by the storage capacity losses at a certain volume fraction.
-   In contrast to the heat flux, no steep drop was observed for the stored energy at the beginning of discharging.
-   The increase in thermal conductivity only was effective for less fin volume fractions.
-   The combination of driving temperature gradients and conductivity increase has lead to low M and is less favourable than just applying one method.
-   The exergetic efficiency dropped strongly with increasing driving temperature gradients, showing the trade-off between performance and exergy losses.

4.1   *Abstract*

Phase change materials (PCM) can increase the energy densities in thermal energy storage systems. Heat transfer rates in PCMs are usually limiting, different improvement methods were used previously, such as fins or improved thermal conductivities. Here, the influence of fin geometries, PCM thermal conductivity and discharge temperature of the secondary fluid are investigated by modelling. The analysed outcomes are their influence on stored energy, heat flux and stored exergy. The two-dimensional time dependent energy equation was solved for a rectangular enclosure with a secondary fluid with constant temperature as boundary condition on one side. The modelled PCM data based on a paraffin melting at 44 °C. The different improvement methods increase the heat flux, but the increase is lower than expected according to idealized calculations. The basis for this investigation is the evaluation of a dimensionless heat flux number formed from the heat flux, thermal conductivity, temperature difference from the secondary fluid to the phase change temperature and a characteristic length of the system. The influence of the better thermal conductivity is found to be lower at higher fin volume fractions. The increase of the discharge temperature difference had the strongest impact on the heat flux, but the exergy loss also increased. The exergy loss was also related to the achieved reduction in the discharge time as an indicator for the heat flux. Here, it was seen that the exergy losses outweigh the advantage in discharge time from a higher discharge temperature difference.

4.2   *Introduction*

Energy storages offer the possibility to reduce the temporal discrepancy between demand and supply of energy, which results from the natural fluctuation of renewable energy resources such as sun and wind. Thermal energy storages are one possible choice, and they are often cost-effective and easily implemented.

Latent thermal storage systems store large amounts of thermal energy in a small temperature range, due to their high phase change enthalpies, thus, they are discussed as a more effective way to store energy than sensitive storage systems. The discussed field of application is broad, e.g. in the storage of heat from renewable energy sources, especially solar energy [123,124], in thermal management for buildings [125–127], in industrial applications [128,129] or for cooling electronics [130]. One problem with latent thermal storage is the often limited heat transfer due to the low thermal conductivity of most PCMs.

Therefore, the improvement of heat transfer is the subject of many investigations [64,65,131,132].

The three main improvement methods for the heat transfer are a larger surface area for heat transfer, increasing the driving temperature difference or to increase the thermal conductivity of the PCM. Dispersed substances with better thermal conductivity provide better possibilities for heat transfer in the PCM, which is equivalent to a PCM with higher thermal conductivity. Mostly the systems are compared with respect to the discharge time, the liquid fraction, and the temperature distributions [133–136]. But the heat flux is another crucial process variable. This is not addressed sufficiently in the literature, although most technical applications of thermal storages depend on the achievable heat flow rate. Therefore, the present work investigates the influence of these improvement methods on the heat flux.

Various possibilities for attaching fins were investigated like longitudinal [133,137] or cross fins [134,138]. Different designs, such as plates or wedge-shaped fins, were also compared [139]. Otherwise, the optimisation of fin systems with respect to the number, spacing and dimensioning of the fins is examined [135,138]. Another approach is to optimise the natural convection in the PCM, through suitably irregularly distributed fin geometries [140].

An alternative way to improve the heat transfer properties of the PCM is to disperse substances with better thermal conductivity into the PCM. Nanoparticles are usually used for this. The storage capacity is reduced less compared to fins when dispersed substances are used, but the increase in thermal conductivity is lower [141]. Different types of nanoparticles are considered in the literature such as aluminium oxide [141–144], copper and copper oxide [145,146], titanium dioxide [147], iron oxide [148] and nano graphite [143,149]. Much of the literature evaluates the properties in relation to the proportion of nanoparticles [141,142,145,146]. Other influences, such as the effect of a magnetic field on the PCM [148] are also considered. Furthermore, different enhancement options are combined, such as nanoparticles together with fins [141], or a porous structure [142,145,148].

Lamberg [150] has developed an analytical model to determine the phase boundary and the fin temperatures of a solidification process in a finned two-dimensional PCM storage and compared the results to experimental findings and numerical simulation with the heat capacity method. She found a deviation of 10 % in the analytically determined melting fractions compared to the numerically simulated ones. and found a better agreement for geometric dimensions in the analytical method where the heat conduction can be approximated one-dimensionally. Bauer [151] also developed an analytical method for determining the

solidification time. The analytical results were compared with simulation results and for one case also with experimental work from the literature. Furthermore, he investigated the influence of various dimensionless parameters that represent storage variables such as the thickness, length, number and spacing of the fins. Kamkari and Shokouhmand [136] have experimentally investigated the melting process of a PCM in a rectangular enclosure. This storage was isothermally heated from one side and isolated on the other sides. They investigated different numbers of fins and different wall temperatures They found that with a higher wall temperature and a lower number of fins, the improvement of heat flow through the fins decreases compared to the case with no fins. In this work, the heat flow rates were addressed, but not the exergy losses.

Gunjo et al. [152] investigated the influence of adding 5 % particles of pure copper, copper oxide and aluminium oxide to a paraffin sample. They tested the influence of added particles on the charging and discharging time compared to pure paraffin. For example, copper addition decreased the charging time by a factor of 10 and led to 8 times faster discharging. With their results they calculated thermal conductivities for the mixtures that were about 1 W/(m·K) for paraffin with copper oxide, 2 W/(m·K) for aluminium oxide addition and 20 W/(m·K) for copper addition.

One aspect that is not addressed explicitly is the strong change of charging and discharging heat flux with time and how it is influenced by fins, conductivity, or the driving temperature difference. Further, the relation between the change in heat flux and discharge time and the investigated improvement method remains unclear. Especially larger temperature differences at discharging have the problem that heat flow rates can be increased, but this also leads to larger exergy destruction.

To investigate these issues, a numerical parameter study of the heat transfer from a PCM during the discharge of a rectangular storage is presented, which can be regarded as part of a larger arrangement. The geometry of fins, the thermal conductivity and the discharge temperature were varied. The material data of the used PCM are from RT44 HC, a paraffin with an average melting temperature of 317.15 K from the company Rubitherm [153]. The system is modelled in 2D using the finite volume method to solve the time-dependent heat conduction equation. Due to the small distance between the fins, convection in the PCM is neglected here. The focus of the investigations is the impact on the energetic performance with the heat flux and the energy and exergy stored as a function of discharge time.

4.3   Modelled System

The modelled system is depicted in Fig. 4.1. The rectangular storage shown in part a of Fig. 4.1 is the basis for the investigation. The two surfaces on the right and left are plates, functioning as heat exchangers with water as secondary fluid. The PCM and the vertical aluminium fins are placed at regular intervals between the plate heat exchangers. It is assumed that the temperature distribution is periodic in y-direction and symmetric with the fins being the planes of symmetry. Thus, along the line of symmetry in the y-direction, the system can be reduced in size by applying an adiabatic boundary condition. The same condition can be applied at the central symmetry line in x-direction. The system reduced in this way is shown in Fig. 4.1 in the enlarged view b with the dashed lines as a rectangle. This system is the basis for the simulation as shown in the detailed view in Fig. 4.2
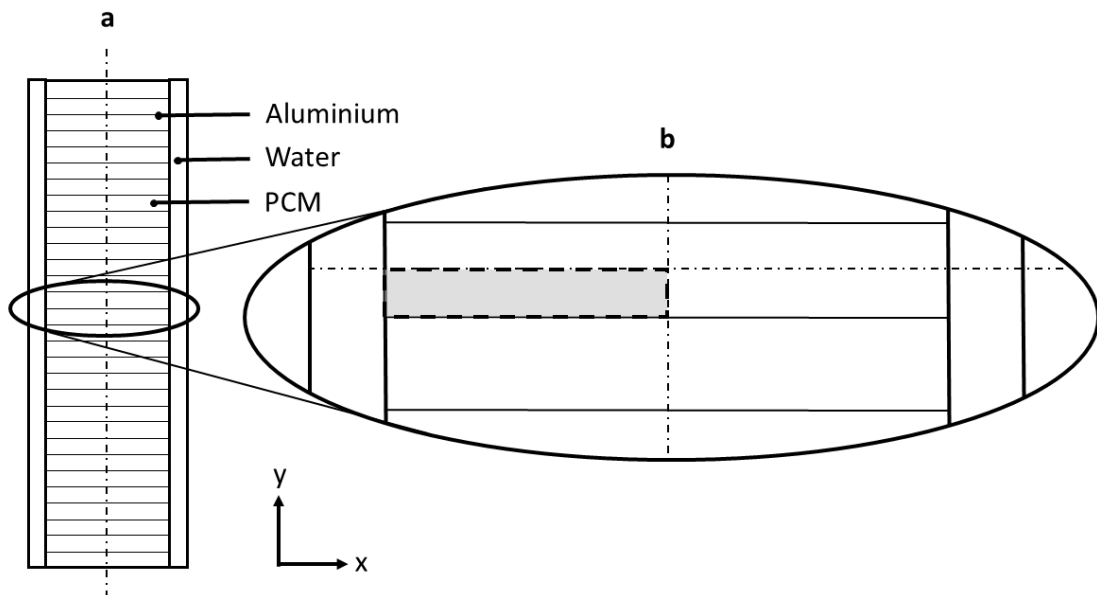
Fig. 4.1 Schematic view of the problem geometry.
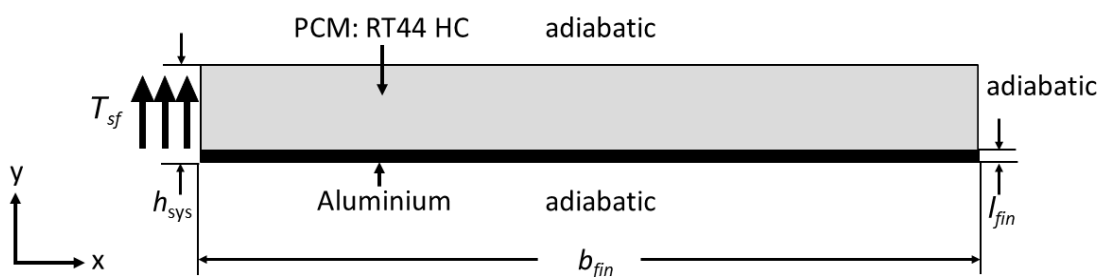
Fig. 4.2 Detailed view of the simulated system.

The height of the simulated system is $h_{sys} = 5$ mm, while the width is $b_{fin} = 50$ mm. The thickness of the aluminium fin is $l_{fin} = 0.5$ mm. Except for the left side of the system, the boundaries of the system are adiabatic. The PCM in the system is shown in grey. For this, the commercially available PCM RT44 HC from Rubitherm [153] was assumed as base system, where the material properties of the PCM as given by the manufacturer are shown in Table 4.2. The used properties for aluminium can be found in Table 4.3 and are based on values in the VDI heat atlas [154, p. 629–637] for AlMg2.5. The temperature dependence of the properties of aluminium was neglected due to the relatively small temperature interval considered here.

Table 4.2 Thermophysical properties of RT44 HC [153].

Property	Value
c_p (liquid)	2 000 J/(K·kg)
c_p (solid)	2 000 J/(K·kg)
ρ (liquid)	800 kg/m^3
ρ (solid)	800 kg/m^3
λ (liquid)	0.3 W/(m·K)
λ (solid)	0.3 W/(m·K)
T_{melt}	317.15 K
h_{melt}	250 000 J/kg

Table 4.3 Thermophysical properties of Aluminium [154, p. 629–637].

Property	Value
c_p	870 J/(K·kg)
ρ	2680 kg/m^3
λ	140 W/(m·K)

For all simulations, an initial temperature of $T_0 = 322.15$ K was used, which corresponds to a difference of 5 K to the phase change temperature T_{melt}. The internal energy is discharged to a secondary fluid, which is assumed to have a constant temperature of T_{sf} (like seen in Fig. 4.2) on the whole left side of the system.

The temperature T_{sf}, the thermal conductivity of the PCM and the type of included fin were varied throughout the simulations. T_{sf} varies from 315.15 K to 302.15 K, which corresponds to a difference of 2 to 15 K to the phase change temperature T_{melt}. To investigate

the influence of thermal conductivity of the PCM, the values were varied from 0.3 to 1 and 1.5 W/(m·K). The used fin geometries are shown in Fig. 4.3.
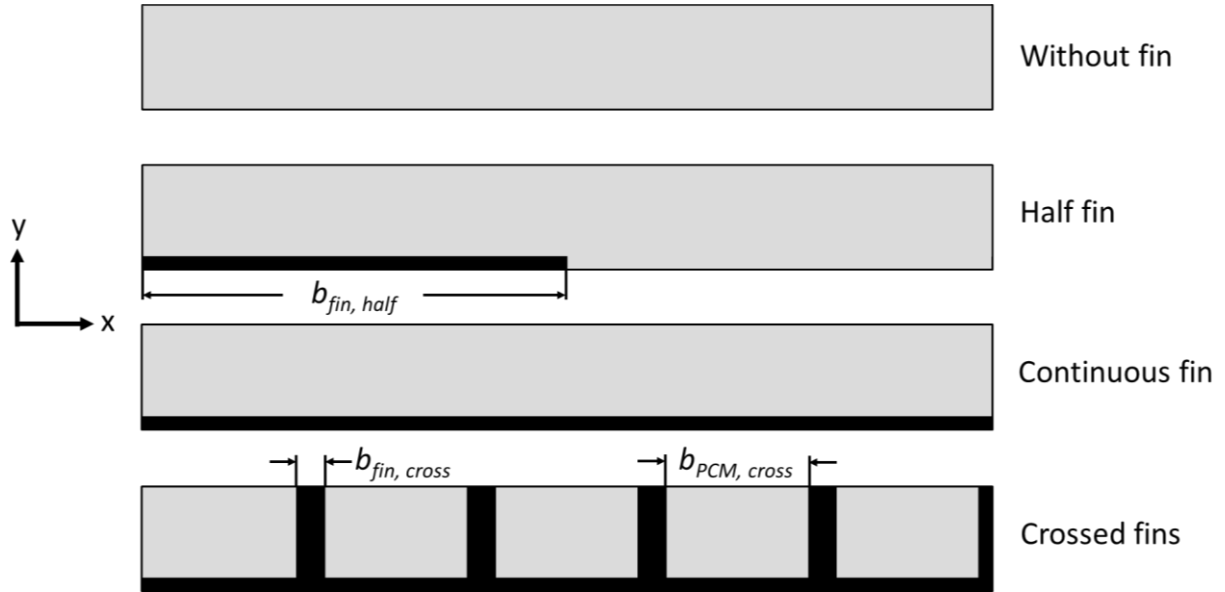
Fig. 4.3[9] Investigated fin cases in the system.

Aluminium is shown in black and the PCM in grey. The fin volume fraction varies for the different systems and increases from top to the bottom in Fig. 4.3. The system with crossed fins has the highest aluminium content; by using vertical fins with $b_{\text{fin, cross}} = 10$ mm that are placed on the horizontal fin. These fins are regularly distributed in the system, resulting in 5 voids with a width of $b_{\text{PCM, cross}} = 9.1$ mm filled with PCM. The aluminium on the right side of the system has only half the thickness of $b_{\text{fin, cross}}$ due to the symmetry of the entire system.

The system with a continuous fin, a temperature in the secondary fluid $T_{\text{sf}} = 312.5$ K and a thermal conductivity of 0.3 W/(m·K) is taken as the reference for the present investigations.

4.4   *Model*

The two-dimensional time dependent energy balance Eq. 4.1 is solved with a finite volume solver, neglecting convection. The rectangular mesh consists of 450 cells in the y-direction and 250 in the x-direction. Regarding to the dimensions of the system this leads to cell edge length of the cells of $d_{\text{cell, y}} = 0.0111$ mm in the y-direction and $d_{\text{cell, x}} = 0.2$ mm in the x-direction. The

---

[9] The x-y dimension of this figure was added and is, thus, deviating from the published manuscript.

heat conduction Eq. 4.1 is solved using the python package FiPy [122] and the time dependent temperature distribution is calculated.

$$\rho \cdot c(T) \cdot \frac{\partial T}{\partial t} = \nabla \left[\lambda(T) \cdot \left(i \cdot \frac{\partial T}{\partial x} + j \cdot \frac{\partial T}{\partial y} \right) \right] \tag{Eq. 4.1}$$

All further quantities of interest, such as the heat flux and the energy can be derived from the cell temperatures and their gradients. For simulating the phase change, the heat capacity method is used. With this method the phase change occurs over a temperature interval and thus a heat capacity can be defined along the phase change. With the normal distribution as a basis, Eq. 4.2 was used for the heat capacity c.

$$c(T) = \frac{1}{\sqrt{2 \cdot \pi \cdot \sigma^2}} * \exp \left\{ \frac{-(T - T_{\text{melt}})^2}{2 \cdot \sigma^2} \right\} \cdot h_{\text{PCM,melt}} + c_{\text{p,liquid}} \tag{Eq. 4.2}$$

The assumed size of the temperature interval for the phase change and thus the value of the heat capacity is determined via the variance σ^2. This value of σ was set to 0.1 K in the present work and leads to a good reproduction of the analytical solidification solution of the one dimensional system without fins, the Stefan-problem [155, p. 203-206].

The energy per cell is calculated with Eq. 4.3 using the properties of the cell material. The sum of the energies of all cells is the current given total internal energy in the system for a certain time.

$$E_{\text{cell}} \begin{cases} d_{\text{cell,x}} \cdot d_{\text{cell,y}} \cdot \rho \cdot \int_{T_{\text{sf}}}^{T_{\text{cell}}} c_{\text{PCM}}, & \text{energy PCM} \\ d_{\text{cell,x}} \cdot d_{\text{cell,y}} \cdot \rho \cdot c \cdot (T_{\text{cell}} - T_{\text{sf}}), & \text{energy aluminium} \end{cases} \tag{Eq. 4.3}$$

At the start of the simulation, all cells have the initial temperature 322.15 K. For the left side of the system, a constant temperature T_{sf} is used as a boundary condition. Starting from this initial condition, the simulation is carried out until each cell has reached the condition $T_{\text{cell}} \leq T_{\text{sf}} + 0.5$ K. In this way, the time required for the simulation is kept within reasonable limits.

4.5   *Discussion and results*

The reference system with a continuous fin, thermal conductivity of 0.3 W/(m·K) and $T_{\text{sf}} = 312.15$ K is analysed, the other systems are then compared to this reference. Figure 4.4 shows the heat flux and the internal energy of the system as a function of the discharging time.
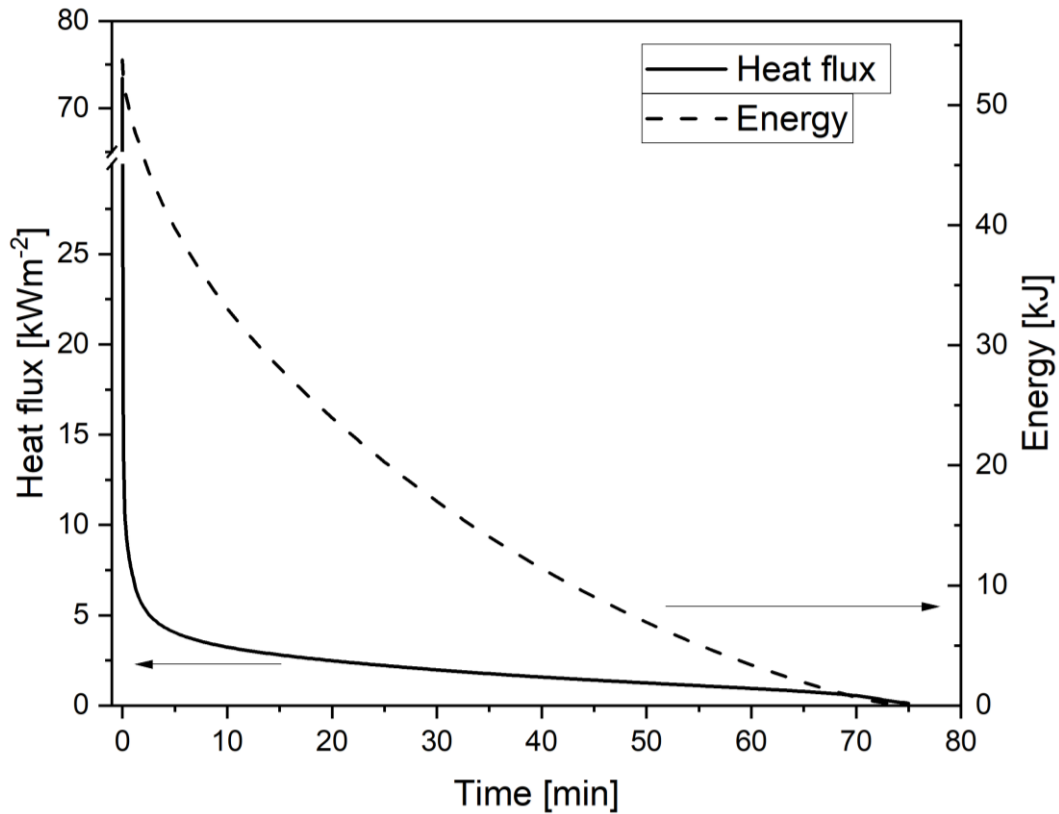
Fig. 4.4 Heat flux and energy as a function of time for reference system with continuous fin, 0.3 W/(m·K) and T_{sf} = 312.15 K.

Figure 4.4 shows the heat flux and the energy over time in minutes. The time to discharge all cells to 0.5 K above the secondary fluid temperature takes 75 min. The heat flux drops steeply from more than 70 kWm^{-2} to 5 kWm^{-2} within the first 3 min. The heat fluxes, as typical for two-dimensional calculations, are for a length of one meter in the orthogonal z-direction. After the first 3 minutes, the drop in heat flux flattens out and there is a continuous reduction over time. Overall, the heat flux is low with values below 5 kWm^{-2} after 3 min. The energy curve is slightly concave, but unlike the heat flux, it does not show an initial steep drop in stored energy.

The reason for the strong decrease of the heat flux at the beginning of the process can be found in the rapid formation of a solidified layer. The formation of this layer can be traced in Fig. 4.5.
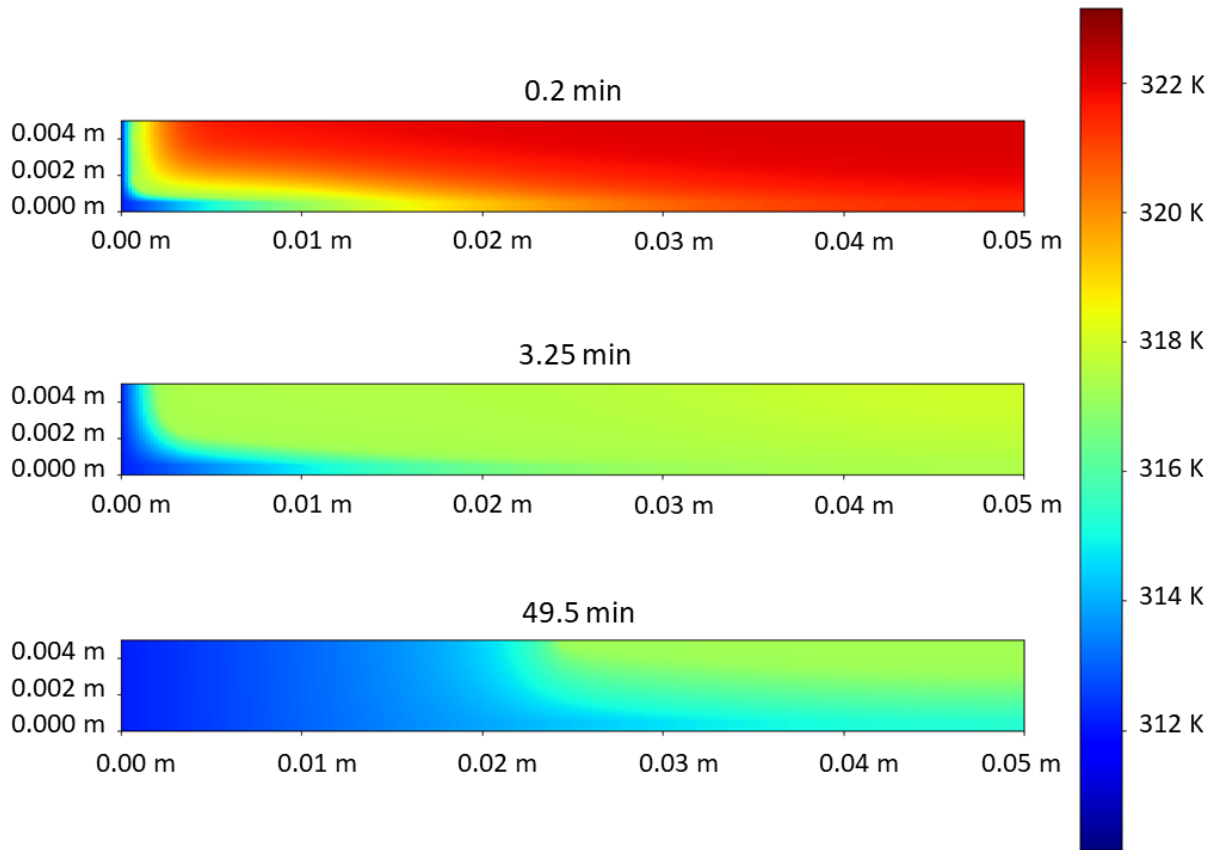
Fig. 4.5 Temperature distributions at 0.2 min, 3.25 min and 49.5 min for the reference system with continuous fin, 0.3 W/(m·K) and $T_{sf} = 312.15$ K.

There, the temperature distributions in the system are shown for 0.2 min, 3.25 min and approximately 50 min graphically. After 0.2 min a solidified layer is seen in dark blue at the left and lower left system side. The distance to the heat transferring left side is short for those cells so that the heat flux is high, as seen in Fig. 4.4 and the PCM solidifies quickly there. The layer starts forming from the left side and at the bottom left corner and lowers the heat flux due to the lower temperature difference to the secondary fluid. It can also be seen that the temperature in the area near the fin drops more quickly along the length of the storage, due to the significantly higher thermal conductivity of the metal which leads to higher temperature gradients in y-direction. It is noticeable that the temperature decreases faster along the fin than in the PCM in x-direction. However, the fin doesn´t reach T_{sf} quickly over the complete length as it could be expected with its higher thermal conductivity. Instead, a curved shape of the phase transition area is observed over the complete discharging time with significant lower fin temperatures for only some mm in x-direction. Furthermore, the amount of the sensible thermal energy in the system after reaching 5 kWm^{-2} is small, because nearly each cell is at least at a

temperature of 317 K, which corresponds to the phase transition temperature. This part of the initial energy of the system can be discharged way quicker than the phase change energy. So, the faster retrievable part of the sensible heat and the formation of the solidified layer as an insulator are responsible for steep drop of heat flux at the beginning of the discharge.

To investigate the influence of different fin geometries on the discharge process, the storage with a continuous fin is compared with systems that have no fin, half a fin or additionally vertical fins, as shown in Fig. 4.3. The heat fluxes over time for the different fin types at reference conditions (0.3 W/(m·K) and T_{sf} = 312.15 K) are shown in Fig. 4.6.
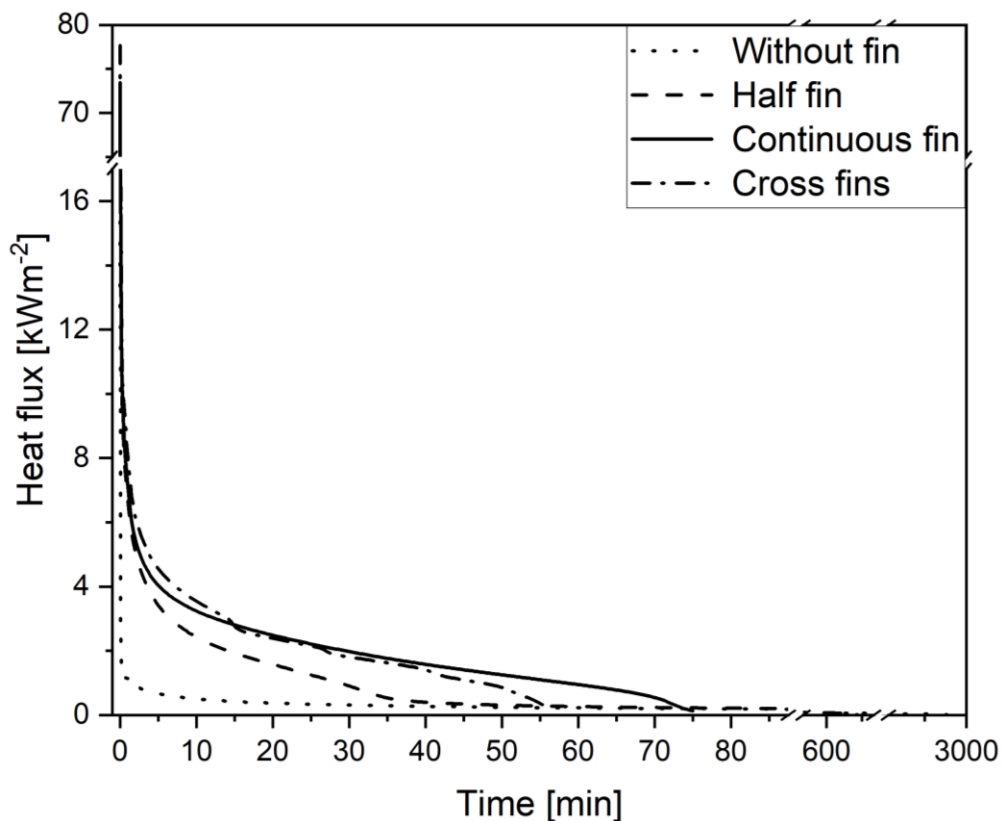
Fig. 4.6 Heat flux and energy over time for systems with different fin geometries, 0.3 W/(m·K) and T_{sf} = 312.15 K.

In Fig. 4.6, the solid line shows the heat flux evolution for the reference case with a continuous fin, the dotted line for a system without fin, the dashed line for a system with a half fin and the dashed-dotted line for the crossed fin system. The initial drop of the heat flux described before also occurs with all fin geometries.

However, a difference in the heat flux evolution is recognized after the steep drop. With increasing fin volume, the heat flux after the initial drop increases. As an example, in the storage without fin after 3.5 min a heat flux of approximately 778 W/m² is found, whereas for the

cross-fin system values of 3.7 to 3 kW/m² between 5 to 7.5 min can be reached. This can be related to the isolating effect of the already solidified PCM. A system with fins provides a larger area over which energy can be transferred vertically from the PCM, which leads to an increase in heat flux even if an isolating layer is formed. The difference in the progress of the phase change can be seen in Fig. 4.7. There, the temperatures in a system without a fin and one with a continuous fin are plotted at reference conditions after 50 min of discharging.
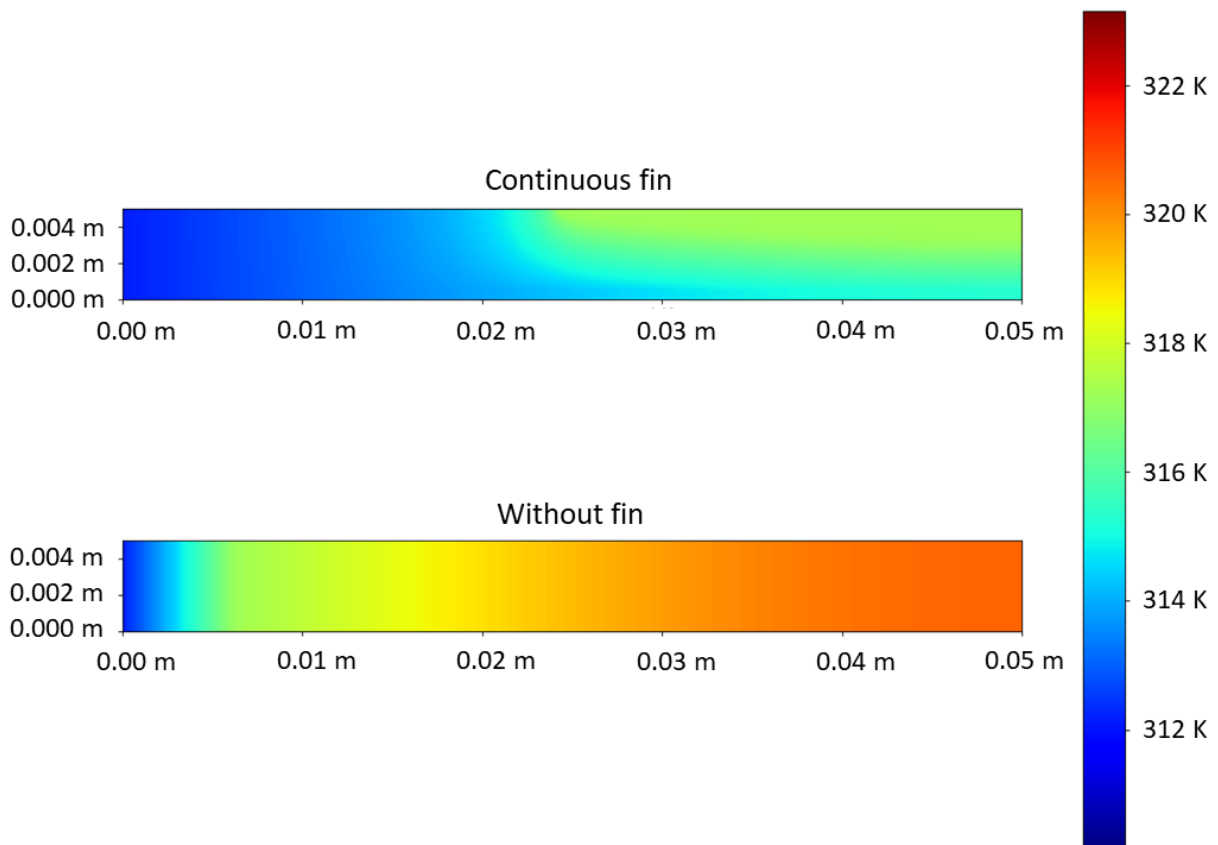
Fig. 4.7 Temperature distributions at 50 min for systems with continuous fin and without fin, 0.3 W/(m·K) and $T_{sf} = 312.15$ K.

It is clearly seen that in the system without fin there is only a temperature gradient in x-direction and the phase change does not progress as fast as in the case with a continuous fin. With an increasing proportion of fins, the advantage in discharge time is smaller. This can be better observed in Fig. 4.8, where the energy for the 4 different systems is plotted against time.
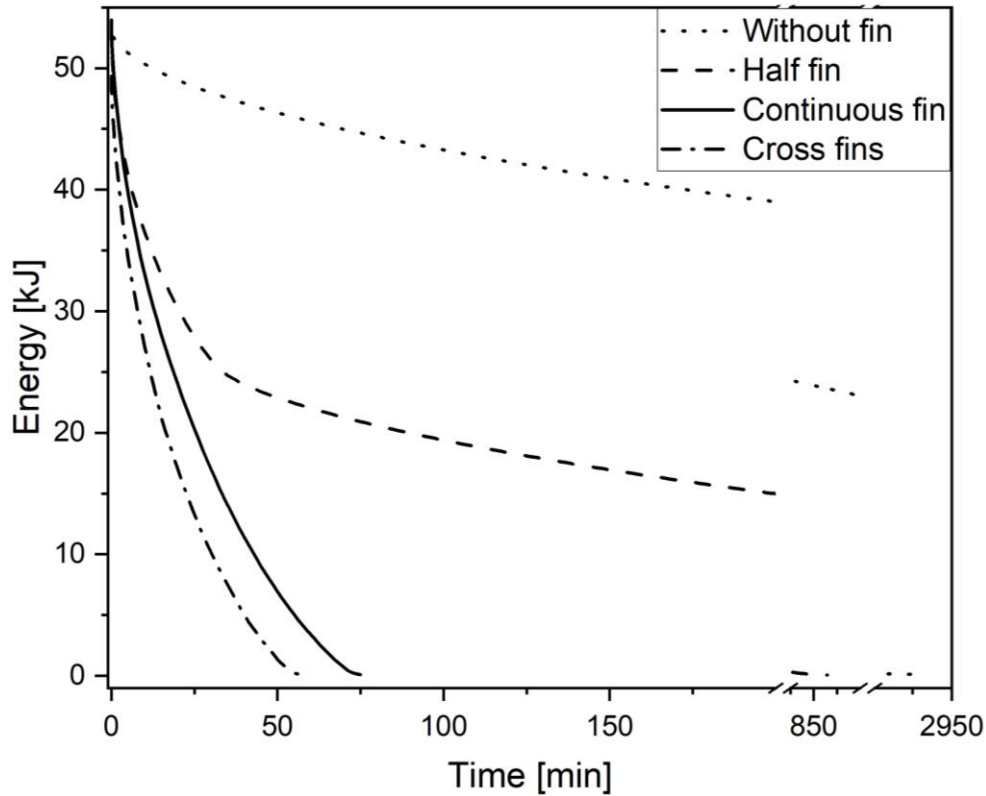
Fig. 4.8 Total amount of energy in the system over time for different fin geometries, 0.3 W/(m·K) and T_{sf} = 312.15 K.

As seen in Fig. 4.8 a storage system with a half fin requires only 29.5 % of the discharge time compared to a system without a fin, whereas a system with cross fins requires 75.7 % of the discharge time of a system with a continuous fin. Thus, the effectiveness of the additional fin material decreases. The possible amount of stored energy and the volume fractions of PCM and aluminium are shown in Table 4.4. The stored energy is calculated with Eq. 4.3; the volume fractions depend on the geometry of the fins and decreases with the PCM volume fraction.

Table 4.4 Volume fraction of PCM and aluminium, and total amount of stored energy at $T_{\text{cell}} = T_0 = 322.15$ K for considered fin geometries.

	Volume fraction PCM	Volume fraction aluminium	Stored energy at T_0 [kJ]
Without fin	1	0	54.00
Half fin	0.95	0.05	51.59
Continuous fin	0.9	0.1	49.18
Cross fins	0.819	0.181	45.28

Because of the low impact of the sensible energy of aluminium on the stored energy, the energy drops nearly as much as the volume fraction of the PCM in the system. A comparison of the stored energy for cross-fin systems to the storages without fins demonstrates the coincidence, at 81.9 % PCM volume fraction the energy storage capacity drops to 83.9 %.

The decrease in stored energy is lower than the decrease of the discharge time with increasing volume fraction of aluminium. The discharge time is 24.3 % lower for crossed fins compared to continuous fins, but the stored energy is only 7.9 % lower. In the considered cases the advantage of a larger fin volume is given. But it can be assumed that the effectiveness of additional fin volume will continue to decrease. So, there will be a point, where the reduction of discharge time with increasing fin volume will be outweighed by the continuous loss of stored energy due to the reduction in PCM volume fraction.

Furthermore, the influence of the thermal conductivity of the PCM on the heat flux is investigated. For this purpose, Fig. 4.9 compares a system with a continuous fin and a system without a fin, whereby the heat flux over time is examined for thermal conductivities of 0.3 W/(m·K), 1 W/(m·K) and 1.5 W/(m·K).
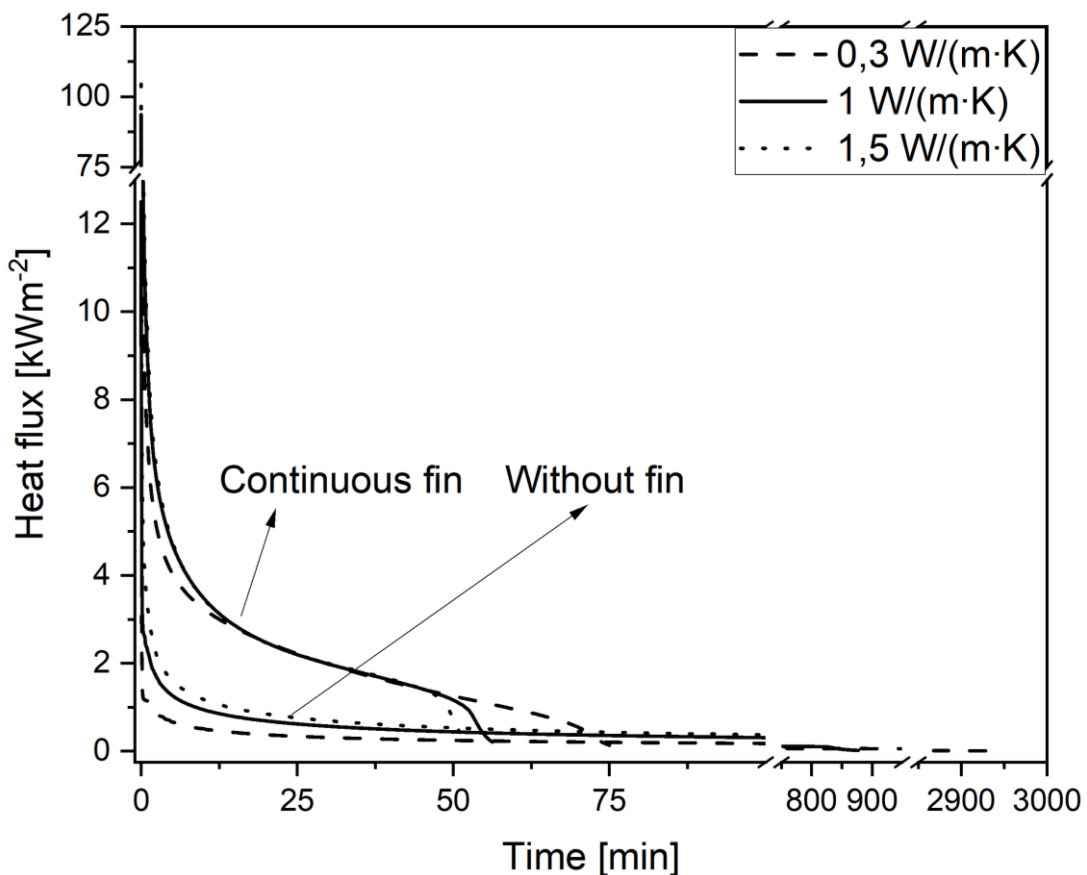
Fig. 4.9 Heat flux as a function of time for thermal conductivities of 0.3 W/(m·K), 1 W/(m·K) and 1.5 W/(m·K) with continuous fin and without fin, $T_{sf} = 312.15$ K.

The upper group of curves in Fig. 4.9 belongs to the system with a continuous fin, while the lower group belongs to the system without a fin. In the system without a fin, a proportional increase of the heat flux with increasing thermal conductivity is observed, while for a system with a continuous fin, the heat flux is increased 10 to 20 % until a discharge time of 15 min. From this point on, the heat fluxes are the same throughout the systems until 48 min. After this the time for full discharge is lower for higher thermal conductivity. This discharge behaviour suggests that the increase in thermal conductivity becomes more ineffective with increasing fin volume fraction and that the impact of the fin on discharge outweighs the effect of increasing thermal conductivity.

For a better comparison of the influence of the heat exchange enhancement methods on the discharge process, a dimensionless heat flux number M is calculated from the heat flux $\dot{q}$, the thermal conductivity of the PCM λ, the initial temperature difference ΔT (between T_0 and T_{sf})[10] and a characteristic length L, as shown in Eq. 4.4.

$$M = \frac{\dot{q}}{\lambda \cdot \frac{\Delta T}{L}}$$
(Eq. 4.4)

Here the length in the y-direction of the system was used as the characteristic length since the phase change is last completed in this direction.

In order to quantify the influence of the increase in thermal conductivity more precisely for the two systems discussed above, Fig. 4.10 shows the dimensionless heat flux number M as a function of the Fourier number for the same thermal conductivities as in Fig 4.9. The characteristic length needed to calculate the Fourier number is also the length in y-direction.

---

[10] The description of the equation parameter was extended and is, thus, deviating from the published manuscript.
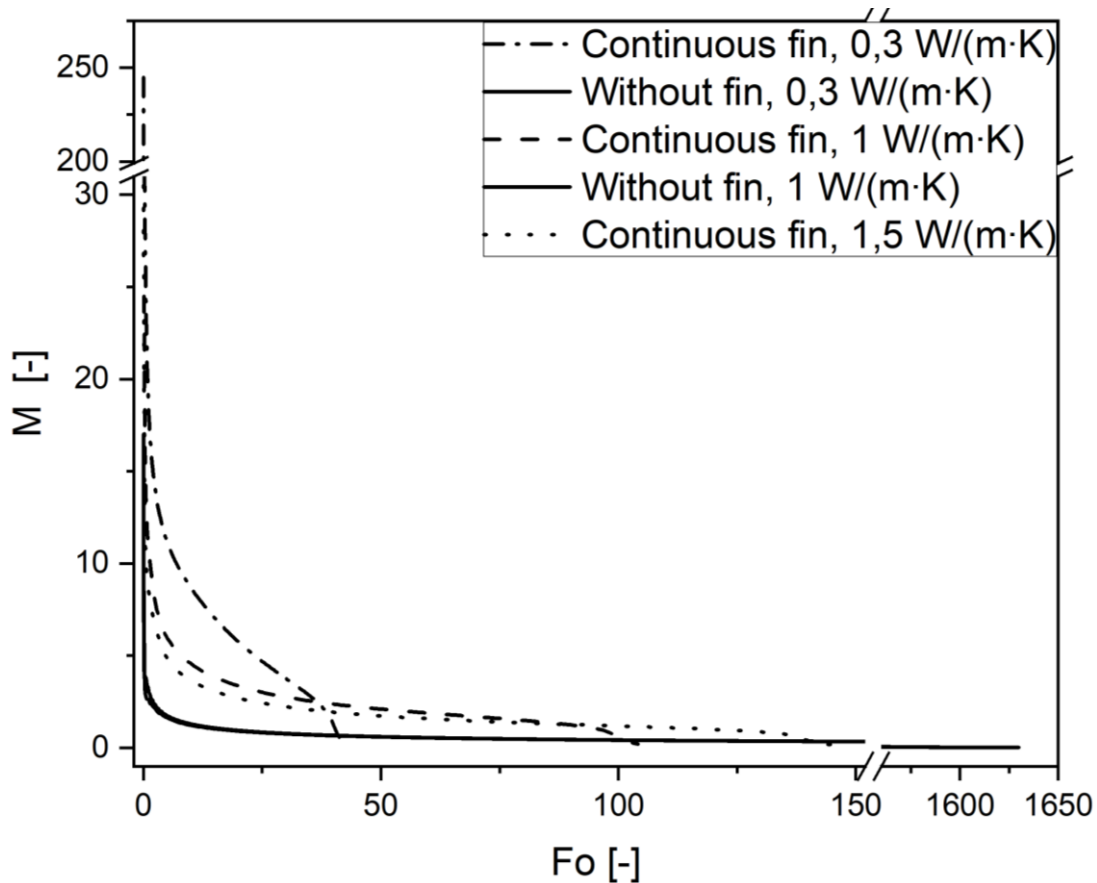
Fig. 4.10 Dimensionless heat flux *M* as a function of the Fourier number for thermal conductivity of 0.3W/(m·K), 1 W/(m·K) and 1.5 W/(m·K) with continuous fin and without fin, $T_{sf} = 312.15$ K.

The curves for the system without a fin are all shown with continuous lines, as these almost overlap indicating that the increase in heat flux is proportional to the increase of the values from the boundary conditions in the denominator. The systems with continuous fins show different results. For this condition the dimensionless heat flux number decreases with increasing thermal conductivity and comes closer to the curve for the system without a fin. This means in contrast to the results of the system without a fin that the increase of heat flux does not increase proportional to the thermal conductivity and increasing the thermal conductivity in systems with fins loses effectiveness and is less needed, as summarized in Table 4.5, where the discharge time of the system is shown depending on the fin geometry and the thermal conductivity.

Table 4.5 Discharge times in min for two thermal conductivities and different fin geometries for T_{sf} = 312.15 K.

λ [W/(m·K)]	Without fin	Half fin	Continuous fin	Cross fins
0,3	2895	865	75	57
1	855	270	56	47
Ratio	0,30	0,31	0,75	0,82

The discharge time decreases with higher thermal conductivity and fin volume fractions. However, the ratio between the discharge time at 0.3 W/(m·K) and 1 W/(m·K), shown in the third row, shows that the discharge time decreases less with increasing fin volume fraction. For a system without fin, the higher thermal conductivity leads to a ratio of 0.30, which means that the discharge is 70 % faster, while with cross fins as the system with the highest fin volume, the discharge is only 18 % faster with a ratio of 0.82 between the two thermal conductivities. Accordingly, the influence of the thermal conductivity decreases significantly with increasing fin volume. Furthermore, Fig. 4.10 shows that the Fourier number increases for the continuous fin with increasing thermal conductivity. This shows that for a system with one specific fin case the decrease in discharge time is not proportional to the increase in thermal conductivity.

The influence of T_{sf} was also investigated, because the heat fluxes can be increased with larger driving temperature differences. The temperature differences to the phase change temperature of 5 K, 10 K and 15 K were investigated. In Fig. 4.11 the time dependence of the heat flux is presented for a system with a continuous fin and a thermal conductivity of 0.3 W/(m·K).
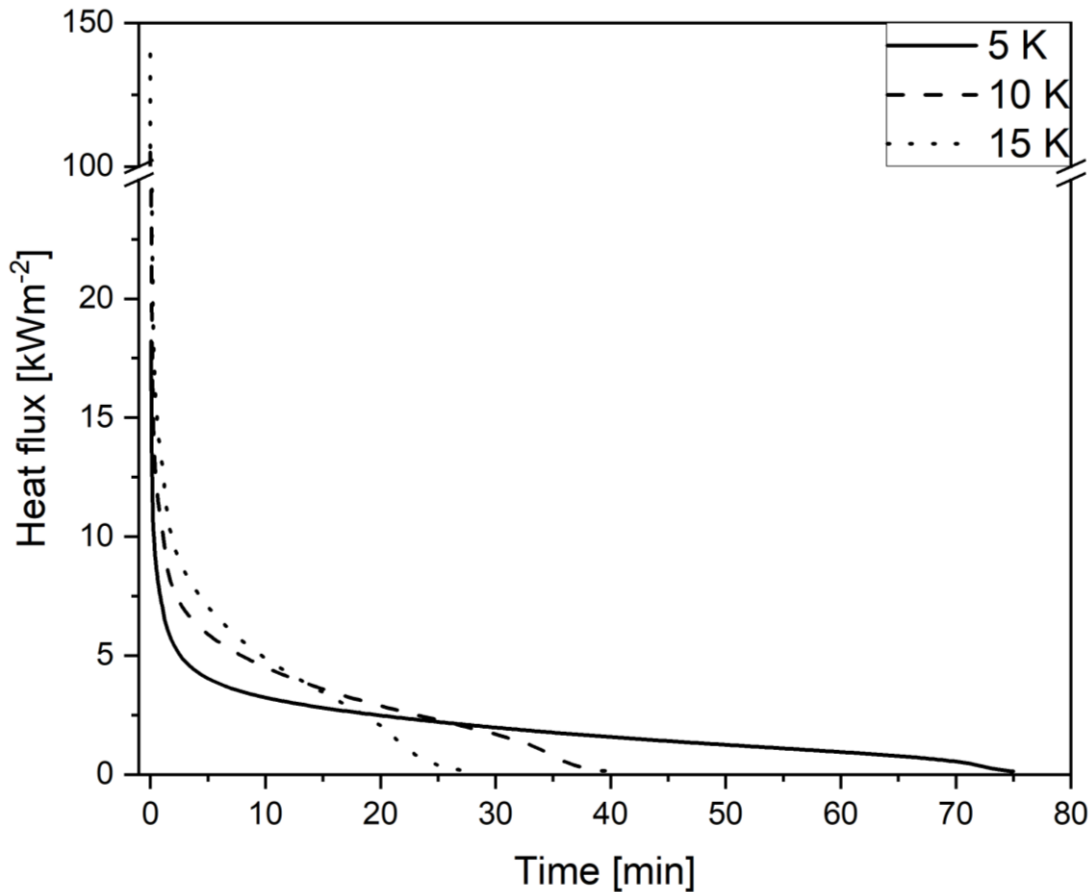
Fig. 4.11 Heat flux as a function of time for temperature differences of 5 K, 10 K and 15 K in a system with continuous fin and 0.3 W/(m·K).

An increase in the heat flux and a reduction in the discharge time of approximately 46 % can be observed comparing the temperature differences (ΔT) of 5 K with the one of 10 K. Thereby, the heat flux at $\Delta T = 10$ K falls below the level of $\Delta T = 5$ K at about 27 min. The heat flux at $\Delta T = 15$ K is for approximately 14 min higher than the heat flux at 10 K. Overall the change in heat flux is higher when changing from 5 K to 10 K than from 10 K to 15 K, as also seen for the discharge times. There the discharge time is lower for higher temperature differences, which leads to the intersection of the curves.

Fig. 4.12 shows the dimensionless heat flux *M* plotted as the function of the Fourier number for the three temperature differences for a continuous fin and a thermal conductivity of 0.3 W/(m·K).
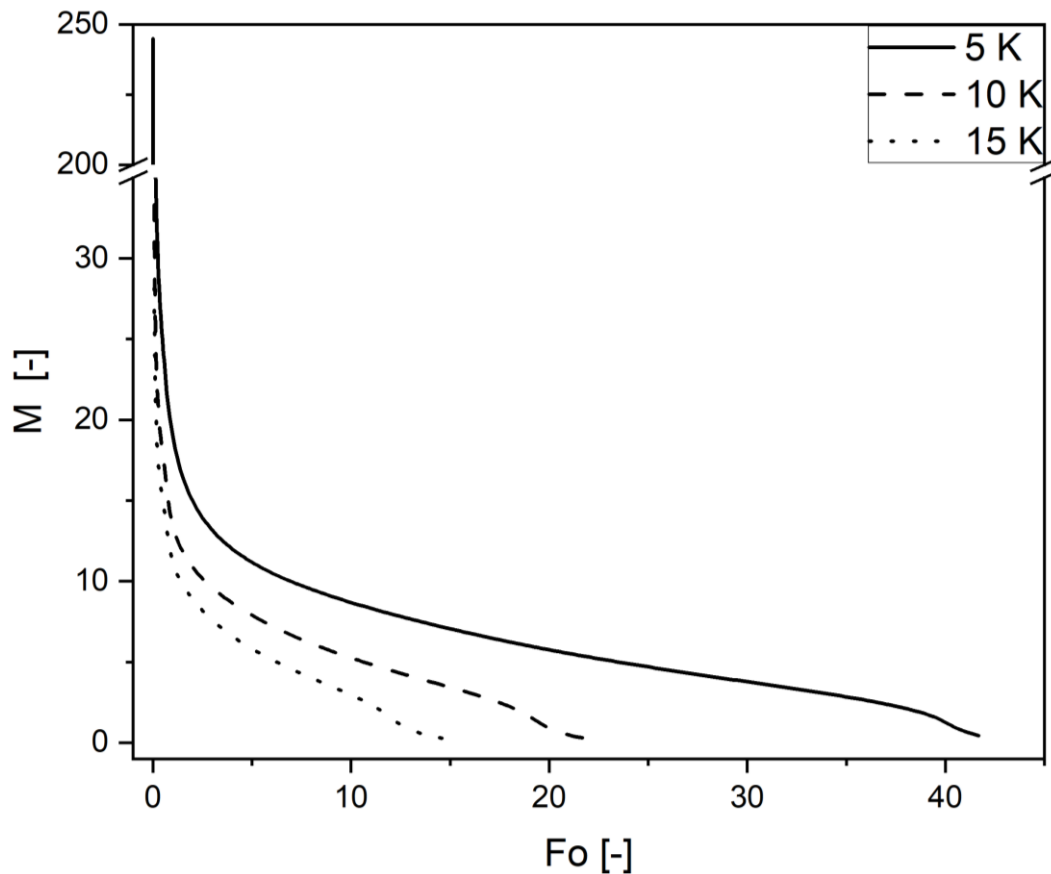
Fig. 4.12 Dimensionless heat flux as a function of the Fourier number for temperature differences of 5 K, 10 K and 15 K for a system with continuous fin and 0.3 W/(m·K).

The level of the dimensionless heat flux decreases with an increasing temperature difference of T_{sf} and the phase change temperature of the PCM. Like also seen in Fig. 4.11, there is a larger drop of the heat flux number from $\Delta T = 5$ to $\Delta T = 10$ K than from 10 to 15 K. Similar to the variation of thermal conductivity, the heat flux is not increased proportionally to the temperature difference to the secondary fluid.

Furthermore, the comparison of the influences of higher thermal conductivity and lower discharge temperatures is of interest. A comparison is seen in Fig. 4.13 for the possible combinations of 0.3 W/(m·K) and 1 W/(m·K) at 5 K and 10 K for a system with a continuous fin.
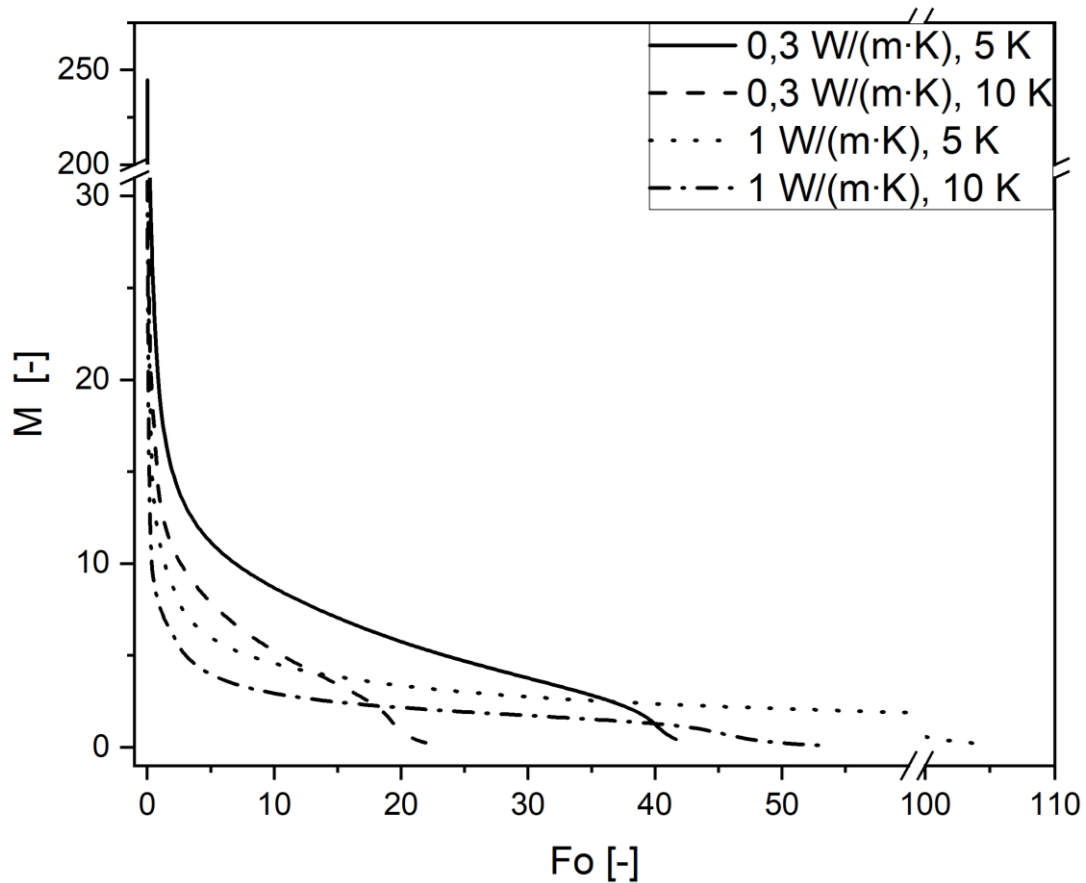
Fig. 4.13 Dimensionless heat flux as a function of Fourier number for temperature differences of 5 K and 10 K with 0.3 W/(m·K) and 1 W/(m·K) for a system with a continuous fin.

In comparison the system with ΔT = 5 K and 0.3 W/(m·K) has the highest dimensionless heat flux for Fo>30, but the second lowest Fourier number at full discharge. The system with a conductivity of 0.3 W/(m·K) and a difference of 10 K has the second highest dimensionless heat flux level as well as the lowest Fourier number at full discharge. The combination of high driving temperature differences and high conductivities leads to quite low dimensionless heat fluxes and is worse than just applying one method to increase the heat flux.

In Fig. 4.10 it was observed that the decrease of discharge time is not proportional to the increase in thermal conductivity. In addition to that, Fig. 4.13 shows that the increase in thermal conductivity has the same influence on the discharge time regardless of the temperature difference. This is seen in the same ratio of the Fourier numbers at full discharge for the systems with equal temperature difference but different thermal conductivities. The ratio of Fo at full discharge for 0.3 W/(m·K) at 5 K and 1 W/(m·K) at 5 K is about 0.4, which is also the ratio for the Fo at 0.3 W/(m·K) and 1 W/(m·K) both at 10 K.

Besides the fact that T_{sf} has the highest influence on the heat flux and the overall discharging time, it has also a huge impact on the exergy. Lowering T_{sf} means that it gets nearer to the ambient temperature $T_{ambient}$ which leads to lower extractable exergies, and it should be considered whether it is reasonable to use lower T_{sf}. For each of the T_{sf}, the exergy of the transferred heat Ex_{trans} is determined according to Eq. 4.5.

$$Ex_{trans} = \left(1 - \frac{T_{ambient}}{T_{sf}}\right) \cdot Q_{trans} \qquad \text{(Eq. 4.5)}$$

Q_{trans} is the heat transferred over the whole discharge time. $T_{ambient}$ was taken as 298.15 K. T_{sf} is constant due to the boundary condition. Thus, the factor before Q_{trans} is constant for a specific temperature difference. In the following it is called *f*. Ex_{trans} can be compared with the exergy Ex_{total} in the storage at the initial temperature. Ex_{total} is the same for each case because the start temperature was not varied. The exergetic efficiency is defined as $\eta_{Ex} = Ex_{trans}/Ex_{total}$. The values for the different considered ΔT can be found in Table 4.6.

Table 4.6 Transferred heat, exergies and exergetic efficiencies for different ΔT. System with continuous fin and 0.3 W/(m·K).

ΔT [K]	f [-]	Q_{trans} [kJm^{-2}]	Ex_{trans} [kJm^{-2}]	Ex_{total} [kJm^{-2}]	η_{Ex}[-]
2	0.0539	52.60	2.84	4.1	0.6927
5	0.0446	53.68	2.41	4.1	0.5872
10	0.0293	55.40	1.62	4.1	0.3959
15	0.0132	57.29	0.76	4.1	0.1845

The transferred heat slightly increases from 52.60 kJ at 2 K to 57.29 kJ at 15 K due to the higher temperature difference and thus a higher sensible heat fraction. In contrast, the transferred exergy decreases from 2.84 kJ to 0.76 kJ. The exergetic efficiency drops from 69.27 % to 18.45 %, as the final temperature approaches $T_{ambient}$. Thus, the exergetic efficiency is already relatively low at a difference of 2 K and drops strongly with increasing ΔT. In contrast to this decreasing η_{Ex} is the decreasing discharge time and with it the increasing heat fluxes. A calculated exergetic efficiency of 0.6927 at 2 K or 0.5872 at 5 K are relatively high for a thermal energy storage like this, but it should be considered that these efficiencies are achieved with the condition of an isothermal secondary fluid. Overall, there is a trade-off between the efficiency and the discharge time because a high exergy efficiency with very long discharge times is just as unsuitable for applications as a fast discharging, with high exergy losses.

For a comparison, Ex_{trans} and the discharge time t are listed in Table 4.7 for temperature differences of 2 to 15 K for a system with a continuous fin and 0.3 W/(m·K). Furthermore, the transferred exergy and the discharge time are calculated relative to the values for $\Delta T = 2$ K. The relative exergy and relative discharge time are shown in Fig. 4.14.

Table 4.7 Absolute and relative transferred exergy and discharge time for different ΔT in a system with a continuous fin and 0.3 W/(m·K).

ΔT [K]	Ex_{trans} [kJm^{-2}]	t [min]	Ex_{trans} / $Ex_{trans,2K}$ [-]	t /t_{2K} [-]
2	2.84	179	1	1
3	2.70	122	0.95	0.68
4	2.55	93	0.904	0.52
5	2.41	75	0.845	0.42
6	2.26	63	0.80	0.35
7	2.10	55	0.74	0.31
8	1.95	49	0.69	0.27
9	1.78	44	0.63	0.24
10	1.62	40	0.57	0.22
11	1.45	36	0.51	0.20
12	1.29	34	0.45	0.19
13	1.11	31	0.39	0.18
14	0.94	30	0.33	0.17
15	0.76	28	0.27	0.16
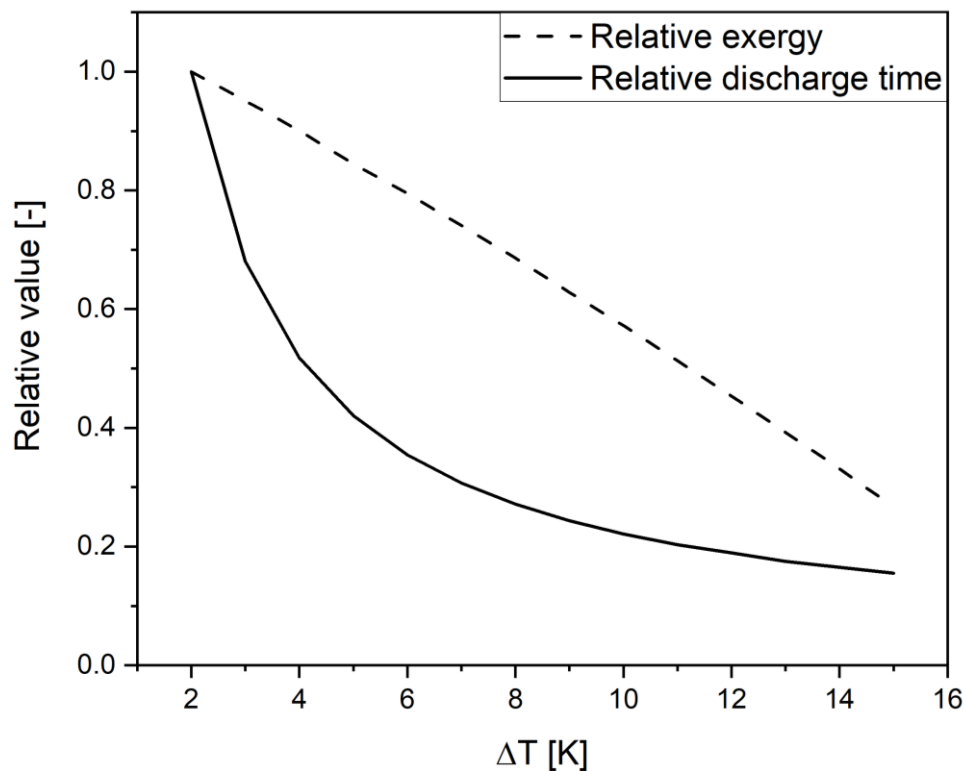
Fig. 4.14 Relative exergy and relative discharge time from Table 2.7 as a function of ΔT for a system with continuous fin and 0.3 W/(m·K).

In Fig. 4.14 it is seen that the relative exergy decreases nearly linearly with increasing ΔT, while the relative discharge time decreases fast at first, but with higher ΔT the slope decrease. The comparison of these two curves shows the trade-off in exergy efficiency and lower discharge times with higher temperature differences. First the relative discharge time decreases faster than the exergy loss until a ΔT of around 6 K, which means that it is beneficial to use higher ΔT until this driving temperature difference, if discharge time is the crucial parameter. But with higher temperature differences than 6 K, the transferred exergy is 20 % lower than for 2 K and decreases for higher ΔT, which can outweigh the reduction in discharge time for some applications. Considering this it can be concluded that increasing the temperature difference is only reasonable up to a certain point and the trade-off between exergy loss and lower discharge times should be weighed carefully for every system and application.

4.6   Conclusion

Methods to improve heat transfer in latent thermal storage systems were investigated by modelling. The considered cases were the introduction of fins into the system, increasing the thermal conductivity of the PCM and a greater temperature difference between the secondary fluid and the phase change temperature of the material. A section of a larger rectangular storage was regarded, in which convection within the material was neglected and where the temperature of the secondary fluid was considered constant.

The study investigated the influence of the fin geometry, the thermal conductivity and the driving temperature difference on the heat flux and discharge time. For this purpose, the absolute data as well as a dimensionless heat flux was considered. Furthermore, the proportionality of the heat flux and discharge time to the growing heat transfer improvement and the trade-off between exergy loss and higher driving temperature differences were investigated.

It was shown that the heat fluxes drop steeply in the first few minutes due to the solidified PCM layer as an isolator. After that, discharging takes place with moderate heat fluxes. With increasing fin volume, the general level of heat flux increased after the initial drop, but the advantage decreased with increasing fin volume. For the thermal conductivity a value of 0.3 W/(m·K), typical for a paraffin as PCM, was compared with better values of 1 and 1.5 W/(m·K). it was observed that the influence decreases with larger fin volumes and the discharge time does not decrease proportional with higher thermal conductivity. This was

reflected in the decreasing dimensionless heat flux number, less decreasing discharge times and higher Fourier numbers at full discharge. The increase in the temperature difference brought the greatest advantage for the heat flux of the considered improvement methods, but there was also a decreasing dimensionless heat flux number and thus a decreasing benefit at higher driving temperature differences. The combination of lower discharge temperatures and increasing thermal conductivity turned out to be the worst variant in the comparison. This was shown by lower dimensionless heat flux numbers for this case than for using only one enhancement method. Within the scope of the investigations for the discharge temperature, the exergetic side was also evaluated. It was shown that higher driving temperature differences were advantageous at first, but the benefit of lower discharge time decreased until an ΔT of around 6 K after which the decreasing slope of the relative discharge time was lower than for the exergy loss. Thus, the trade-off between the extractable exergy and the reduction of discharge time for increasing ΔT is important and should be considered in addition to the relation between the change in heat flux and discharge time for different latent thermal energy storage improvement methods.

Chapter 5

The latent thermal energy storage: from simulation to first experiments

In the previous chapters, research questions 1 to 3 were examined with experimental investigations of heat pump operations and simulation-based insights into the discharge performance of a latent thermal storage system. For this storage system, the validation of these prior theoretical findings and their relevance across different temperature levels remains unresolved. A higher temperature level is crucial, given the broader application potential and increased energy value, such as exergy, associated with higher storage temperatures. Additionally, the charging dynamics of the storage must be considered in a combined system with a heat pump, as the charging is directly connected to the heating system. In contrast, the discharge behaviour heavily depends on the specific application context of the storage, like a hot water reservoir or heating buffer, and isn't always directly linked to the heat pump itself. Consequently, the considered control parameters are the mass flow rate and inlet temperature into the storage, rather than a specific outlet temperature. Similar to the previous simulations, it must be investigated whether alterations in these parameters correspond proportionally to changes in heat flux. Once again, the dimensionless heat flux, represented by M, serves as a valuable parameter for this evaluation.

As previously concluded in chapter 3 and addressed in research question 5, it is furthermore interesting to consider when the combination of the heat pump and thermal storage is more advantageous than only adapting the heat pump to a changed heat demand. Chapter 3 demonstrated that maximizing the load of the heat pump, particularly the compressor, leads to enhanced performance. Hence, the combined system is an approach to reduce regulation losses by maintaining continuous operation at full load and use the excess energy to charge the thermal storage. However, this necessitates designing the system to effectively use the energy from the storage, but sufficient opportunities can be found here, such as preheating water streams in hot water preparation. In such a scenario, the exact heat flow rate from the storage becomes less critical, because even if the desired water temperature is not reached by discharging, the electrical heater power consumption is reduced directly by the heat flow rate. Therefore, it is required to evaluate the energy savings achieved through regulating the heat pump during the

experiment and determine whether these are outweighed by the possible charging heat flow rate of the excess water flow at full load.

The formulated research questions are experimentally investigated here using a latent thermal storage, with the dimensions of the modelled system in chapter 4. Therefore, the secondary fluid condenser outlet of the previously used heat pump system is connected to the storage inlet, enabling variations in water mass flow rate and inlet temperature into the storage by adjusting the heat sink parameters. For experiments at a lower temperature level and validation of the prior simulation model, a PCM with a melting point of 47 °C was selected. Subsequently, the investigation of a PCM with a higher melting point of 60 °C enables higher discharge temperatures and is suitable for the targeted temperature level of heating systems, still allowing a moderate initial temperature gradient for charging. For this temperature level, the combined system is exemplarily discussed by comparing the reduction in compressor power with the heat flow rate to the storage under similar conditions in the experiments.

The results of this chapter, although not published in a journal, constitute additional findings that continue the studies presented in earlier chapters. In summary, the key results of this chapter can be briefly outlined as follows:

- The previous theoretical model was experimentally validated for discharging RT47 with sufficient agreement and an observed dependence of the used model parameters. Particularly, the thermal conductivity of the PCM and the variance of the modelled phase change (heat capacity method) had the highest influence on the simulated heat flux.
- In experiments with RT47, higher initial temperature gradients are less advantageous, especially during the charging process, as indicated by the M-levels.
- At the elevated temperature level of RT60, the effect of increasing initial temperature gradients on the M-level differs for charging and discharging with yet unclear reason. An increase of the M-level is observed for discharging, while there is a decrease for charging.
- The heat flux remains nearly constant for varying water mass flow rates, which can be attributed to the low thermal conductivity of the PCM.
- For the investigated test systems, the combined system is energetically more advantegeous than the adjustment of the heat pump process in response to decreasing heat demand. In the example discussed, the decrease in electrical compressor power was surpassed by the heat flow rate to the thermal storage using the excess mass flow rate for charging.

5.1 Experimental setup

The rectangular thermal energy storage and fins used in this setup are constructed entirely from AlMg2.5 Within the storage unit, 29 vertically positioned plates function as fins, effectively creating 30 sections filled with PCM. Plate heat exchangers are realised by water flowing on both sides of the system. Fig. 5.1 provides a schematic top-down view (x-y section) of the system, with blue denoting water and yellow representing the PCM. The water circulates from the bottom to the top of the storage unit (z-direction) to ensure a more consistent flow.
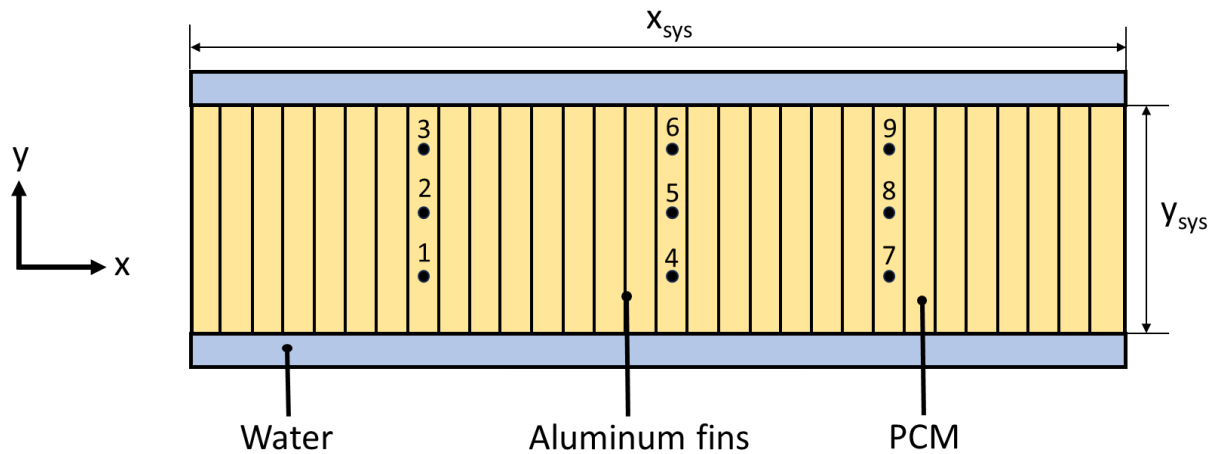
Fig. 5.1 Schematic top-down view of the used thermal energy storage system (z-direction as third, not shown, dimension).

The system measures a total length of 30 cm in the x-direction (x_{sys}) and 10 cm in the y-direction (y_{sys}). Each fin has a thickness of 1 mm, resulting in a spacing of 9 mm for PCM sections. An image showing the top-down view of the system as observed in the laboratory is provided in the appendix (Fig. A.1). The inlet of the thermal storage unit is connected to the secondary fluid outlet of the heat pump, while the water flows to a reservoir after passing the storage. Additionally, the plate heat exchangers are divided into 3 sections for a better flow. This configuration is illustrated in Fig. 5.2, which shows the front view (x-z section) of the system.
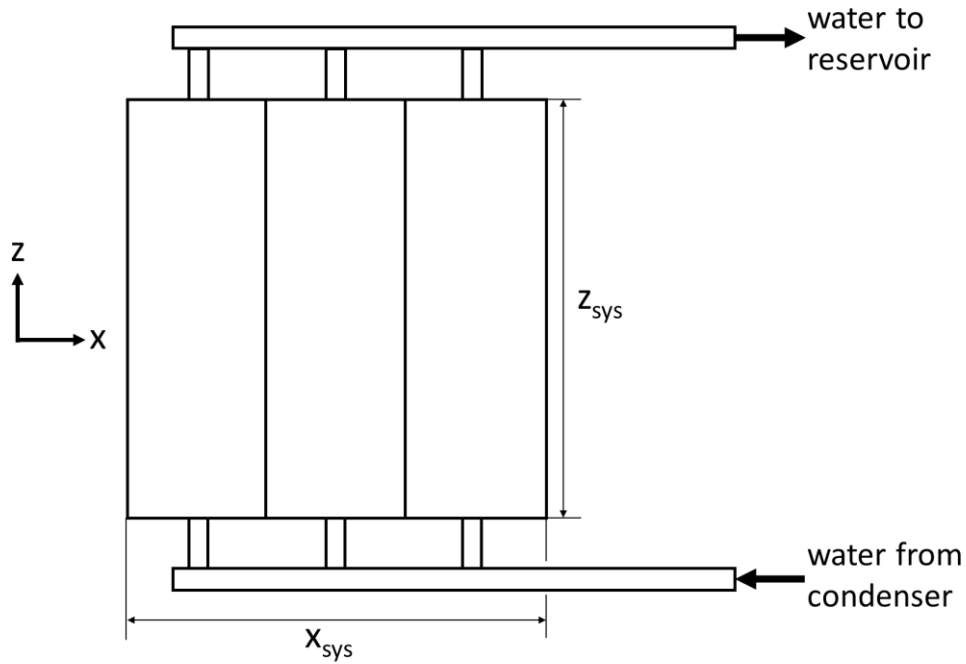
Fig. 5.2 Schematic front-view of the used thermal energy storage system.

An image of the system from that perspective, as observed in the laboratory, is included in the appendix (Fig. A.2). The height of the storage unit in the z-direction (z_{sys}) is 30 cm. Each heat transfer surface extends in dimensions of x_{sys} and z_{sys}, resulting in a combined surface area, A_{sys}, of 0.18 m^2. Additionally, for improved clarity, a sectional side cut view (y-z section) of the system is depicted in Fig. 5.3, with water represented in blue and PCM in yellow.
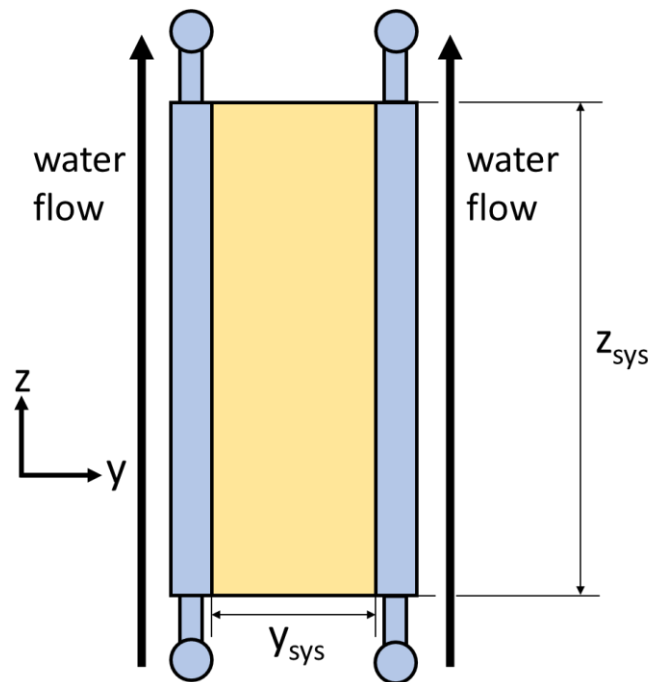
Fig. 5.3 Schematic side cut view of the used thermal energy storage system.

On the water side of the system, Pt-1000 temperature sensors are located at the inlet and outlet of the storage, one pair for each plate heat exchanger. Subsequently, these temperatures are averaged during analysis, with the resulting mean temperature used as either the inlet or outlet temperature. As for the PCM side, 9 temperature sensors are positioned through holes in the cover, systematically arranged along the x and y-axis to ensure uniform temperature distribution recording. The positions of these sensors are indicated as black dots (1-9) in Fig 5.1. All temperature sensors record data at a frequency of 1 Hz.

The used PCMs were RT47 [156] and RT60 [157], both manufactured by Rubitherm. These materials have nominal melting points of 47 and 60 °C, respectively. Selected specifications for the PCMs, according to the manufacturer's data, are summarized in Table 5.1.

Table 5.1 Thermophysical properties of RT47 and RT60 as provided by Rubitherm [156,157].

Parameter	Unit	RT47	RT60
Melting range	°C	41-48	55-61
Solidification range	°C	48-41	61-55
Storage capacity (in temperature range)	kJ/kg	160 (39 - 54 °C)	160 (53 - 68 °C)
Specific heat capacity	kJ/(kg·K)	2	2
Density (solid)	kg/l	0.88	0.88
Density (liquid)	kg/l	0.77	0.77
Thermal conductivity	W/(m·K)	0.2	0.2

The mass flow rate of water is measured and recorded using the flow meter of the heat pump system. It is varied and investigated up to 7.5 kg/min for charging and 9.3 kg/min for discharging. This mass flow can be heated up to 75 °C with the heat pump and used for either charging or discharging. Operation points are regulated for both water mass flow rate and inlet temperature, as these parameters are primarily associated with heat pump application scenarios. To enhance comparability with practical applications and the results from chapter 4, the storage material is initially preheated to a uniform temperature, set either 10 °C above or below the melting point. After achieving this initial condition, a driving temperature gradient of 5, 10, or 15 °C from water inlet to nominal melting temperature is applied to ensure consistency with previous findings. Additionally, the experiment is ended when there is a temperature difference

of 2 °C at all PCM temperature measurement points compared to the water inlet temperature. This approach ensures that the duration of each experiment remains manageable, given that the heat flux is already very low at this point.

5.2   Data evaluation

Given the simple structure of the storage has a simple structure, the studies presented here primarily concentrate on water for a practical approach, although PCM temperatures are also recorded. The heat flow rate $\dot{Q}_{sf}$ transferred to or from the water is determined by the averaged inlet ($T_{sf,in}$) and outlet ($T_{sf,out}$) temperatures:

$$\dot{Q}_{sf} = \dot{m}_{sf} \cdot c_{p,water} \cdot \left(T_{sf,out} - T_{sf,in}\right) \qquad \text{(Eq. 5.1)}$$

In this equation, the specific standard heat capacity of water $c_{p,water}$ is assumed to be 4.1819 kJ/(kg·K). The mass flow rate of water $\dot{m}_{sf}$ is a known and regulated parameter. With the heat transfer area A_{sys} and $\dot{Q}_{sf}$, the heat flux $\dot{q}_{sf}$ can be calculated at any given time. As introduced in Chapter 4, the dimensionless heat flux M can be determined from this:

$$M = \frac{\dot{q}_{sf}}{\lambda_{PCM} \cdot \frac{\Delta T_{melt-sf}}{L}} \qquad \text{(Eq. 5.2)}$$

In this approach, $\dot{q}_{sf}$ is related to the thermal conductivity of the PCM material λ_{PCM}, the inital temperature gradient $\Delta T_{melt-sf}$ (from nominal melting temperature to water inlet temperature), and a characteristic length L. The distance between 2 fins (9 mm) is selected as L since it represents the direction with the slowest melting rate. Consequently, only the change in the temperature gradient affects M in the experiments.

5.3   Discussion and results

The following discussion will first validate the simulation results from Chapter 4. For the same model, new simulations were conducted using data for RT47 (see Table 5.1), which was used in the experiment.

5.3.1 Comparison simulation and experiment

To initially evaluate the overall accuracy of the simulation results, the heat flux obtained from experimental data (light red) is compared with the simulated results using manufacturer-provided parameters (shown in Table 5.1 and represented by the solid line) in Fig. 5.4. This

comparison is conducted for a discharge scenario with an initial temperature of 57 °C, a discharge temperature $T_{discharge}$ of 47 °C, and a water mass flow rate of 9.3 kg/min. This high mass flow rate was selected to closely approximate the assumption of a constant discharge temperature in the simulations.
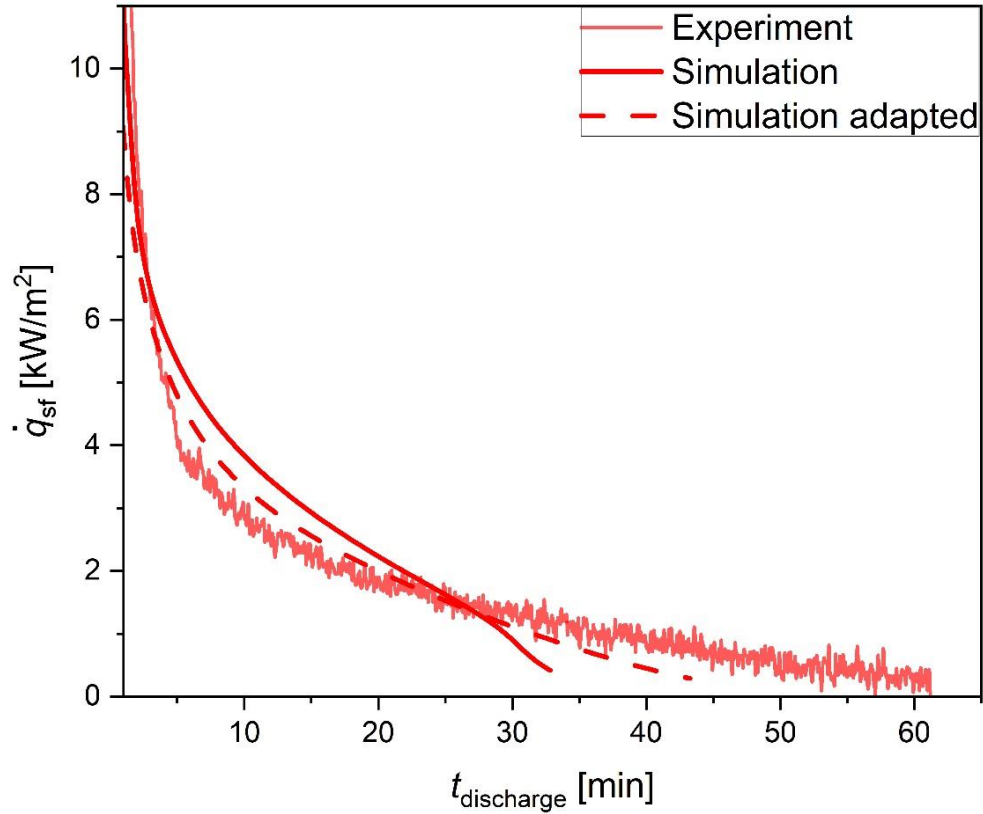
Fig. 5.4 Comparison of heat flux $\dot{q}_{sf}$: experimental data (RT47), simulation (manufacturer values RT47) and simulation (adapted manufacturer values) for $T_{discharge}$ of 37 °C as a function of time. Thermal conductivity of 0.12 W/m·K and variance of 0.5 for adapted simulation and water mass flow rate of 9.3 kg/min for the experiment.

At first, it is evident that the simulation with the manufacturer parameters is within a comparable range of the experiment, offering a fundamentally reliable prediction of experimental outcomes. However, the simulation tends to overestimate the heat flux for the first 15 to 20 min, leading to a considerable underestimation of discharge time. In the experimental setting, the discharge took approximately 61 min, whereas the simulation ended after 33 min.

To enhance the prediction of this model and gain deeper insights into the disparities between simulation and experiment, adjustments were made to the model parameters. Generally, improvements in simulation accuracy were achieved by increasing the variance (from 0.1 to 0.5), reducing the thermal conductivity (from 0.2 to 0.12 W/m·K), and adopting

the specific enthalpy distribution depending on the PCM temperature provided by the manufacturer [156]. In contrast, variation in the specific heat capacity showed negligible impact and was thus maintained at 2 kJ/kg·K. The simulation with these adjusted parameters is illustrated in Fig. 5.4 as dashed line.

These adjusted parameters led to enhanced prediction accuracy in the simulation. Specifically, the initial heat transfer was less overestimated, and the simulated discharge time of 44 min more closely matched experimental observations. Moreover, the decrease in heat flux towards the end of discharge was less steep with the adapted parameters. Consequently, the accuracy of the manufacturer specifications, which may be adequate for technical purposes, has a considerable influence on the more sensitive simulations. Further refinement of model parameters and boundary conditions, such as addressing convection within the storage material, may offer opportunities to enhance accuracy in future iterations.

After the comparison of simulated and experimental data revealed sufficient agreement, the identified trends from Chapter 4 should be verified within the experimental setup while investigating the storage performance for lower temperature levels. Thus, in Fig. 5.5, the discharging heat fluxes $\dot{q}_{sf}$ are depicted for $T_{discharge}$ of 42, 37 and 32 °C, while maintaining a constant water mass flow rate of 9.3 kg/min.
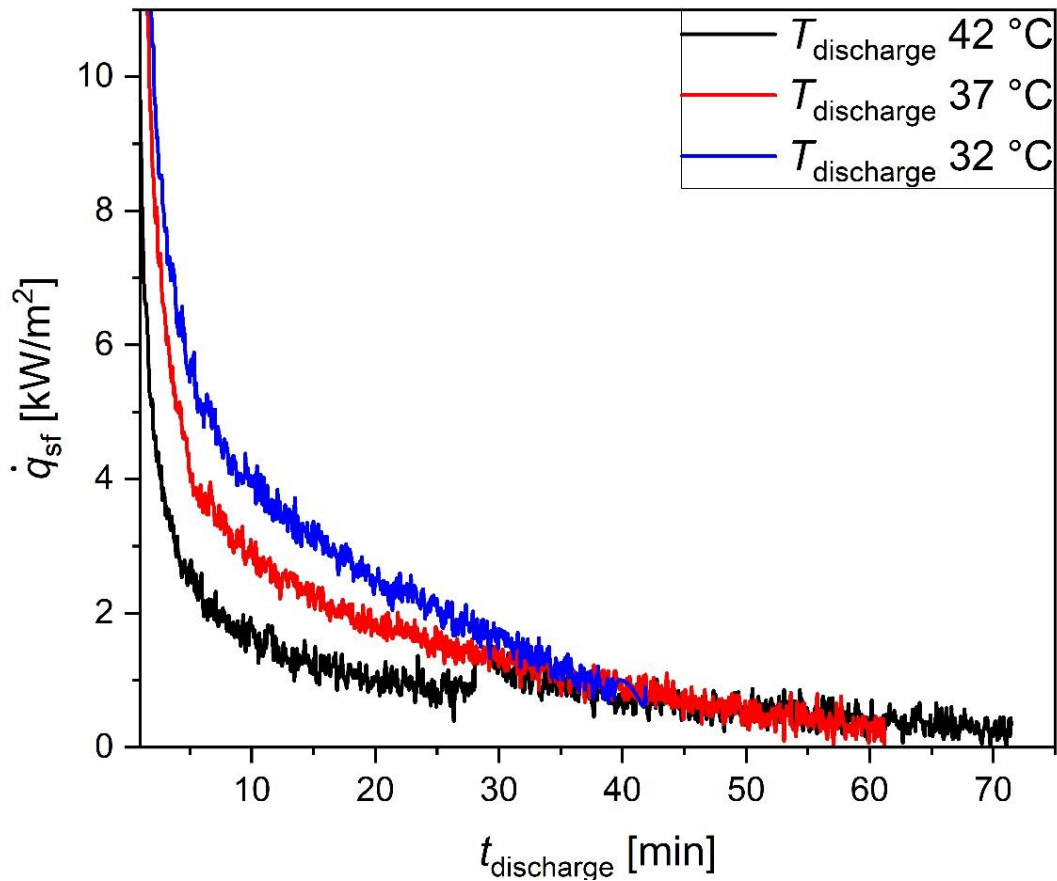
Fig. 5.5 Discharging RT47: heat flux $\dot{q}_{sf}$ for $T_{discharge}$ of 42, 37 and 32 °C as a function of time with water mass flow rate of 9.3 kg/min.

Here, it can be observed that lower discharge temperatures lead to an increase in heat flux, resulting in a decrease in discharge time. After initially high values for the heat flux, there is a sharp drop to a few kW/m^2 within the first minutes. Subsequently, the decrease in the heat flux gets less steep. For example, this occurs after approximately 5 min for a discharge temperature of 42 °C. In chapter 4, this was attributed to the quick formation of an insulating layer of solidified PCM. This formation can be observed in the experiment, as depicted in the top-down view of a PCM-section during a discharge process with $T_{discharge}$ of 37 °C and water mass flow rate of 9.3 kg/min after 10 min, shown in Fig 5.6.
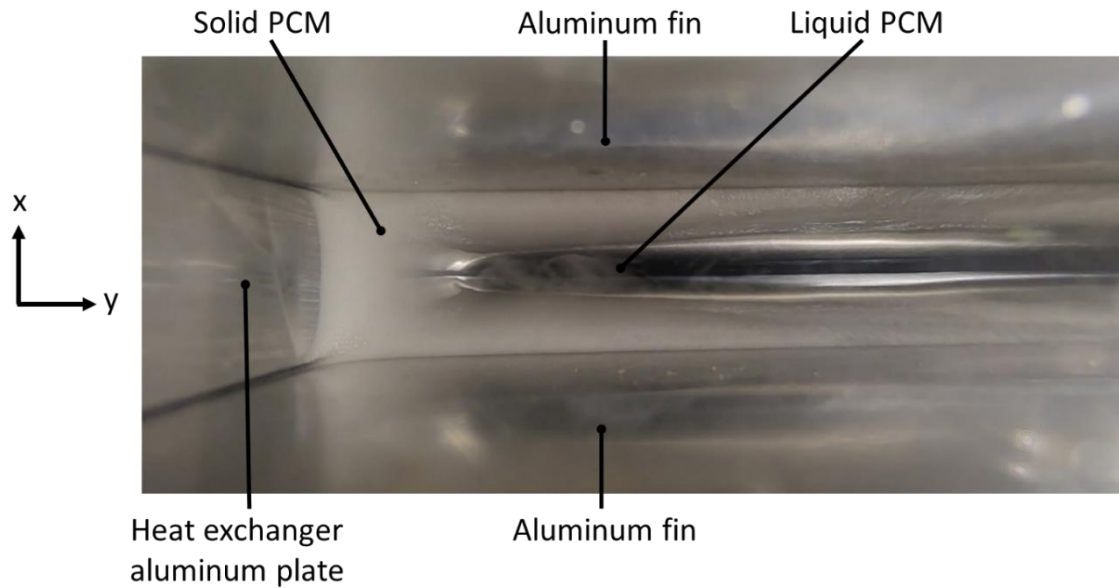
Fig. 5.6 Top-down view on PCM-section (RT47) after 10 min of discharging with $T_{\text{discharge}}$ of 37 °C and water mass flow rate of 9.3 kg/min.

The insulating layer of solidified PCM (white) is visible at the surface area of the heat exchanger plate on the left and the fins on top and bottom of the image. Meanwhile, the remaining liquid PCM is in the middle of the section. Given that this picture was captured after 10 min of discharging, the rapid formation of the insulating layer of PCM matches the simulations.

Moreover, the dimensionless heat flux can be calculated (according to Eq. 5.2) for the heat flux in Fig. 5.5 and the resulting *M* is depicted in Fig. 5.7.
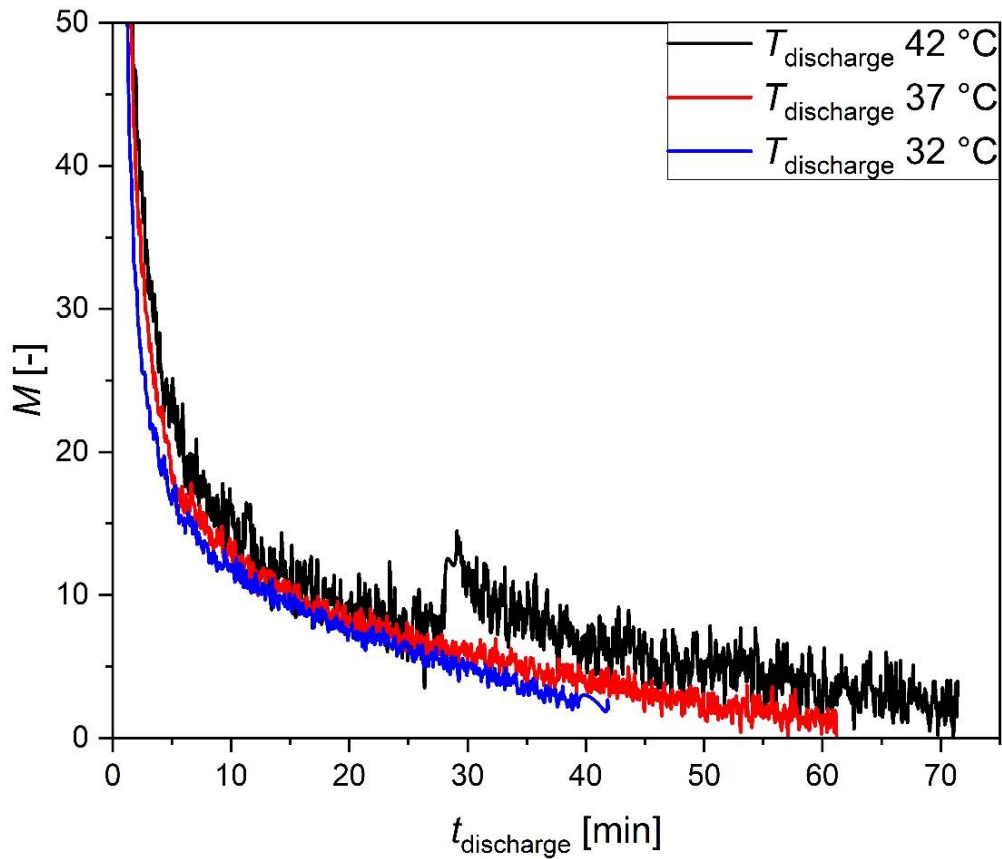
Fig. 5.7 Discharging RT47: dimensionless heat flux M for $T_{\text{discharge}}$ of 42, 37 and 32 °C as a function of time with water mass flow rate of 9.3 kg/min.

It becomes evident that as $T_{\text{discharge}}$ decreases, the M-levels slightly decrease as well. Consequently, $\dot{q}_{\text{sf}}$ increases non-proportionally with lower discharge temperatures (and therefore, higher $\Delta T_{\text{sf-melt}}$). This observation fundamentally aligns with the results in chapter 4 and experimentally demonstrates the lesser benefit of lower discharge temperatures. However, the decrease in M-levels observed here is less pronounced compared to the simulation in chapter 4. This suggests that some model parameters or conditions, whose influences differ especially at different temperature levels, are not fully considered, and the simulation has potential for improvement.

In combination with heat pumps, the charging process is essential for thermal energy storages, as mentioned in the introduction. Consequently, charging was also performed here, aiming to investigate whether the decreasing effect of higher $\Delta T_{\text{sf-melt}}$ occurs. To examine this, Fig. 5.8 shows $\dot{q}_{\text{sf}}$ on the left y-axis and also the resulting M with a slight transparency on the right y-axis for faster correlation. The considered charge temperatures are 52, 57 and 62 °C

with a water mass flow rate of 4.5 kg/min. This flow rate is used because it is more typical for heating systems than the 9 kg/min used for discharging.

Fig. 5.8 Charging RT47: heat flux $\dot{q}_{sf}$ on left y-axis and dimensionless heat flux M on right y-axis for T_{charge} of 52, 57 and 62 °C as a function of time with water mass flow rate of 4.5 kg/min.

As T_{charge} increases, the heat flux also rises for the charging process. For example, after 20 min $\dot{q}_{sf}$ is approximately 2.2 kW/m² for 52 °C, whereas it increases by 63 % to 3.6 kW/m² for charging the same duration with 62 °C. Additionally, the required charging time is reduced; it decreases from approximately 74 min for 52 °C to 47 min for 62 °C. In contrast, the M-level decreases with higher charging temperatures. Thus, the benefit of the increased heat flux for raising T_{charge} decreases noticeably, especially compared to the results for the discharge in Fig. 5.7. In conclusion, charging is less affected by increasing $\Delta T_{sf\text{-}melt}$ than discharging, which should be examined more detailed in future work to investigate the reason for this observed difference.

5.3.2 Transition to a higher temperature level – RT60 as PCM

Following the validation of simulations and low-temperature performance studies using RT47, focus shifts to a higher temperature level suitable for heating and hot water systems. Consequently, RT60 was selected, with a nominal melting point of 60 °C, as it enables the storage to be charged by a typical conventional heating system (temperatures up to 70 °C) and can provide discharge temperature levels suitable for hot water production.

Initially, the discharge process will be examined for selected discharge temperatures of 20, 45, 50, and 55 °C. This approach considers both smaller and larger $\Delta T_{\text{sf-melt}}$ for different potential applications. In Fig. 5.9, the heat flux is shown with the left y-axis, while M is plotted with the right y-axis, both for the mentioned $T_{\text{discharge}}$. The water mass flow rate was set to 3 kg/min, which is more realistic and suitable for the dimension of this thermal storage.

Fig. 5.9 Discharging RT60: heat flux $\dot{q}_{\text{sf}}$ on left y-axis and dimensionless heat flux M on right y-axis for $T_{\text{discharge}}$ of 55, 50, 45 and 20 °C as a function of time with water mass flow rate of 3 kg/min.

It can be observed that with lower discharge temperatures, the heat flux significantly increases, while the discharge time mostly decreases. For instance, the discharge is completed after approximately 75 min for 50 °C, whereas for 20 °C, it takes only 22 min. Notably, the discharge time for 5 °C is less compared to 10°C and 15°C. This can be attributed to the used end criterion, as the experiment is finished upon reaching a temperature of 57 °C in the PCM (a 2 °C difference to $T_{\text{discharge}}$). Due to the non-isothermal phase change in practice and the resulting distribution of the phase change energy in a wider temperature range, a portion of the total storage capacity of 160 kJ/kg remains unused when the experiment is completed at 57 °C. According to the datasheet of RT60 [157], the temperature range from 56 to 52 °C accounts for 62 kJ/kg (about 39 %) of the 160 kJ/kg total capacity. Consequently, the storage capacity is lower for this experiment than for the discharge with 50 or 45 °C, as the complete phase change energy is used for these two. This results in a longer discharge time for 50 and 45 °C compared to 55 °C, despite a higher heat flux.

Once again, the dimensionless heat flux provides further insight. It is evident that the M-levels for the lower $T_{\text{discharge}}$ are closely clustered, whereas for 55 °C, it is noticeably reduced. Thus, in contrast to the results for discharge with RT47, the increase in $\Delta T_{\text{sf-melt}}$ is slightly advantageous here. Particularly, the high observed M-level for 20 °C contrasts with the previous results. The reason for this is not yet clear, but it might be attributed to the difference in the water mass flow rates used for RT47 and RT60.

In chapter 3, it was considered for the heat pump that charging a thermal storage could circumvent the disadvantages of strong throttling to adapt to a changing heat demand in the condenser. Therefore, RT60 in such a scenario is investigated next using T_{charge} of 65, 70, and 75 °C. These temperatures correspond to the heat pump temperature levels in Chapter 3 as well as to the previous thermal storage investigations with $\Delta T_{\text{sf-melt}}$ of 5, 10, and 15 °C, respectively. The heat flux and the dimensionless heat flux for this variation and a water mass flow rate of 4.5 kg/min are shown in Fig. 5.10.
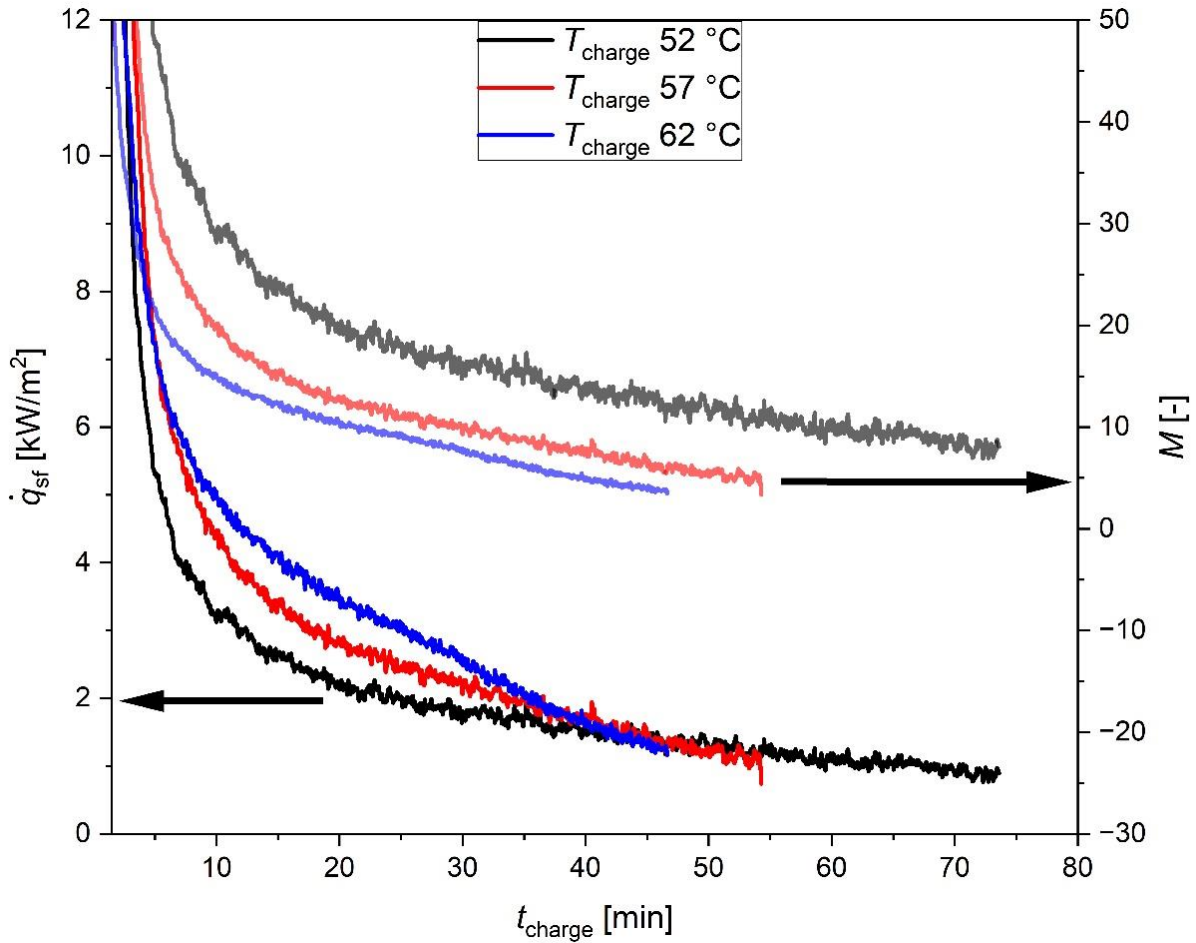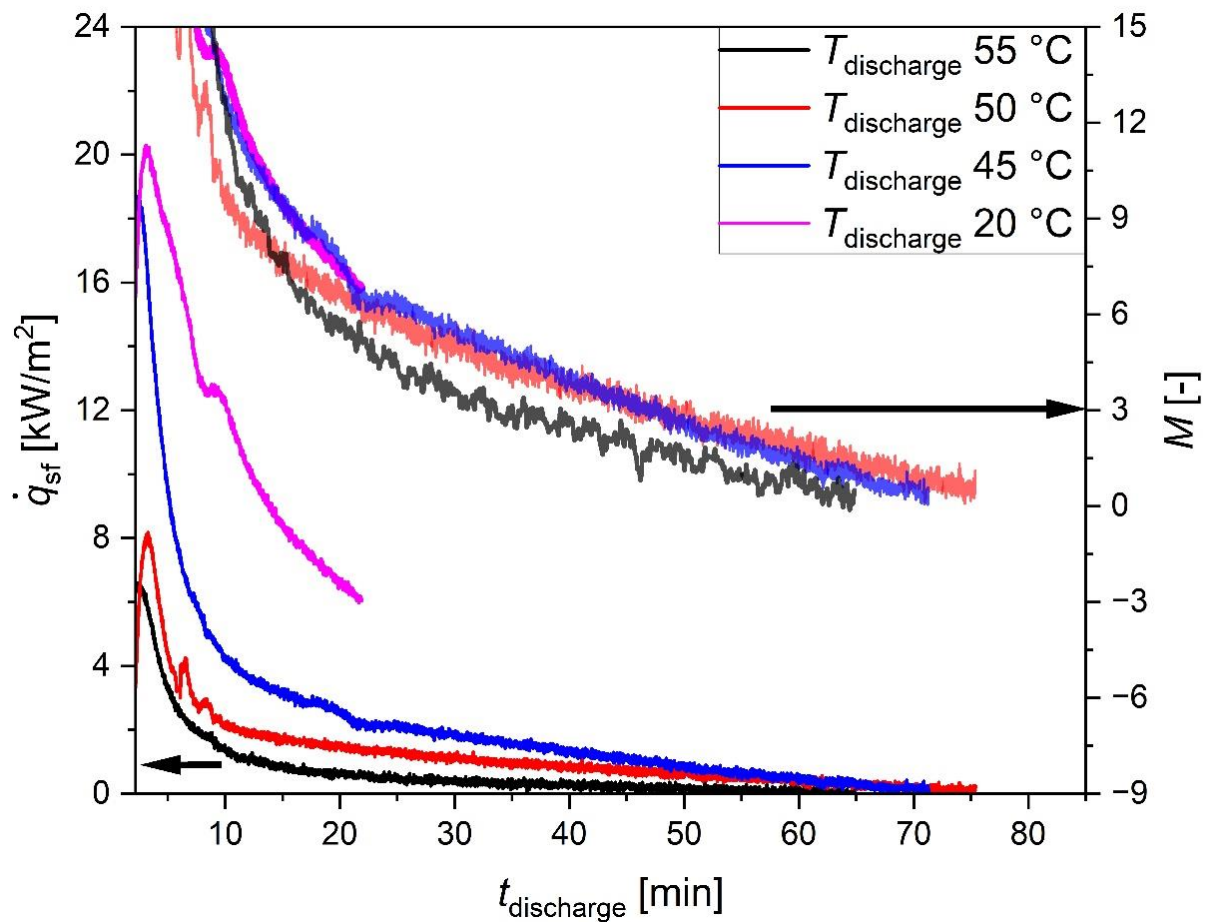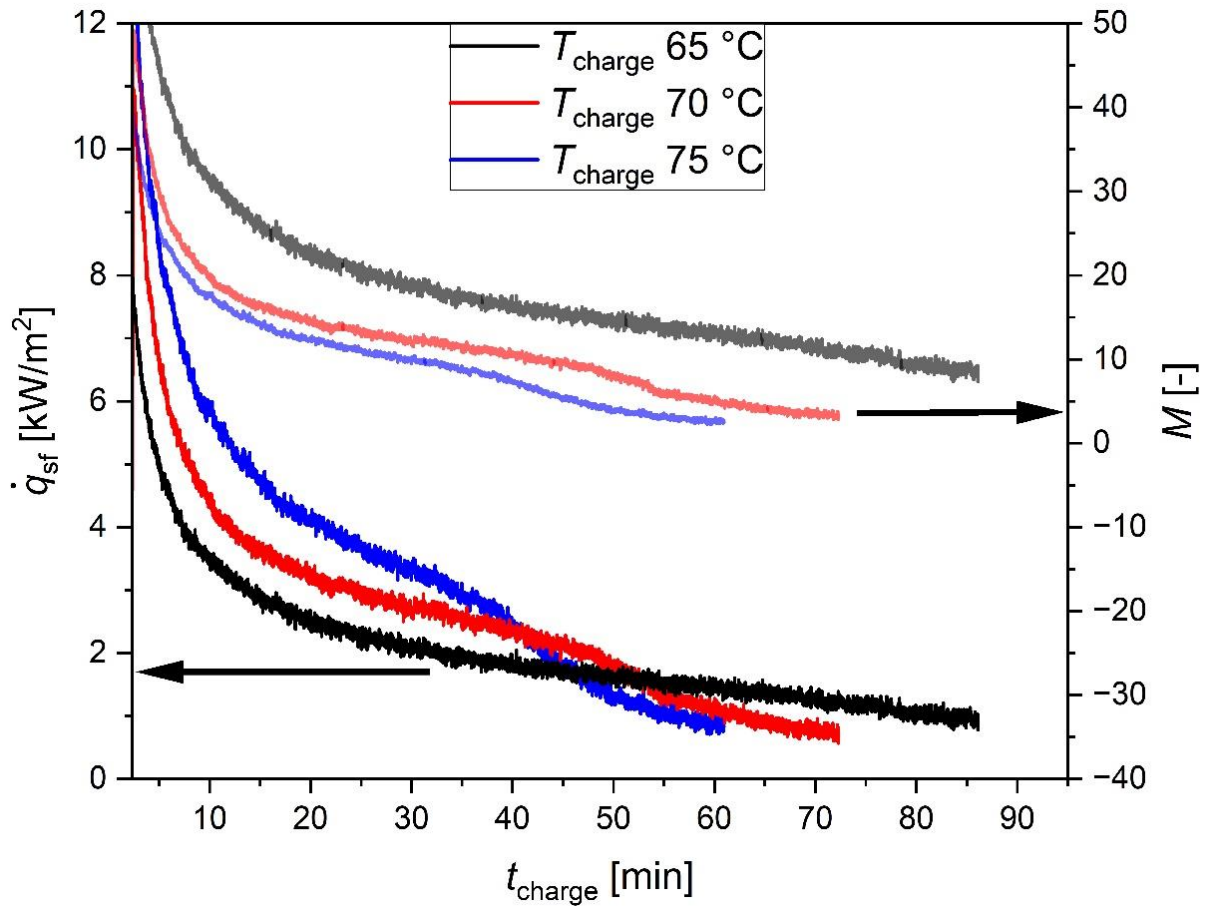
Fig. 5.10 Charging RT60: heat flux $\dot{q}_{sf}$ on left y-axis and dimensionless heat flux M on right y-axis for T_{charge} of 65, 70 and 75 °C as a function of time with water mass flow rate of 4.5 kg/min.

Additionally, alongside the increasing heat flux with higher charging temperatures, a noticeable decline in heat flux towards the end of the process is evident. For instance, at a T_{charge} of 75 °C, this decline occurs approximately after 40 min. Based on observations during the experiment, it marks the point at which the PCM is completely liquid. In its liquid state, the PCM temperature increases faster, leading to a more pronounced decrease in the driving temperature gradient and consequently in heat flux. For lower $\Delta T_{sf\text{-}melt}$, this decline occurs less and over a shorter duration. Furthermore, the M-level decreases for higher charging temperatures. Thus, similar trends to RT47 are observed, indicating that lower charging temperatures are advantageous when the time for the process is not limited.

In conclusion, the influence of the initial temperature difference on the heat flux varies for charging and discharging at the higher temperature level of RT60. The reason for this

remains unclear, but it may be related to differences typical for liquid and solid phases during the process, such as convection or volume changes.

In addition to the temperature level, the circulating mass flow rate represents a significant parameter for heating systems as it is changed frequently due to user regulation. This directly affects the heat pump outlet parameters and subsequently the thermal storage. For this reason, the influence of the water mass flow rate on charging the storage is examined for a similar parameter range as in chapter 3 for the condenser of up to 6 kg/min. The heat flux for water mass flow rates of 3, 4.5 and 6 kg/min are shown in Fig. 5.11. A T_{charge} of 65 °C was selected due to its highest M-level in the previous variation, but a separate examination of M for the mass flow rate is not informative, as it is not influenced by it.
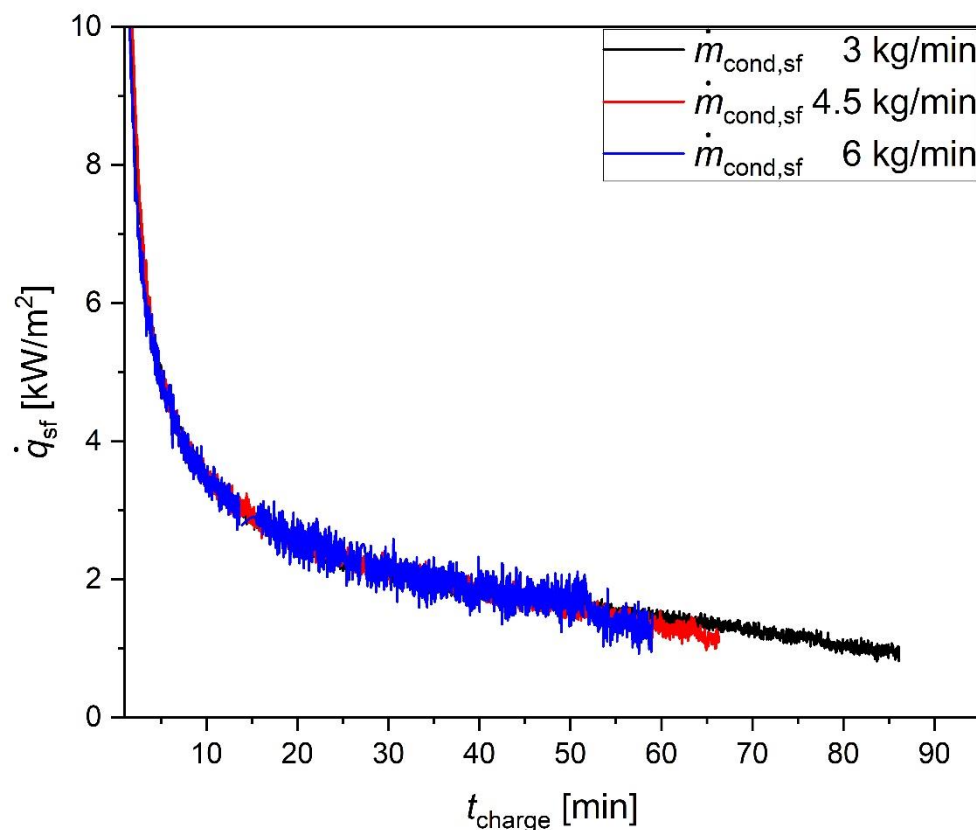
Fig. 5.11 Charging RT60: heat flux $\dot{q}_{\text{sf}}$ for water mass flow rate of 3, 4.5 and 6 kg/min as a function of time with T_{charge} of 65 °C.

In Fig. 5.11, it is evident that $\dot{q}_{\text{sf}}$ remains nearly constant for an increasing water mass flow rate. This observation appears contradictory since a higher water mass flow rate typically implies a higher heat capacity flow of the water. According to Eq. 5.3, an influence on the heat flux would be expected:

$$\dot{q}_{\text{sf}} = \frac{\dot{Q}_{\text{sf}}}{A_{sys}} = \dot{m}_{\text{sf}} \cdot c_{\text{p,water}} \cdot \left(T_{\text{sf,out}} - T_{\text{sf,in}}\right) \cdot A_{\text{sys}}^{-1} \qquad (\text{Eq. 5.3})$$

Given that the specific heat capacity of water, the heat transfer surface area, and the water inlet temperature are controlled parameters, the water outlet temperature $T_{\text{sf,out}}$ is expected to vary. This is illustrated in Fig. 5.12.
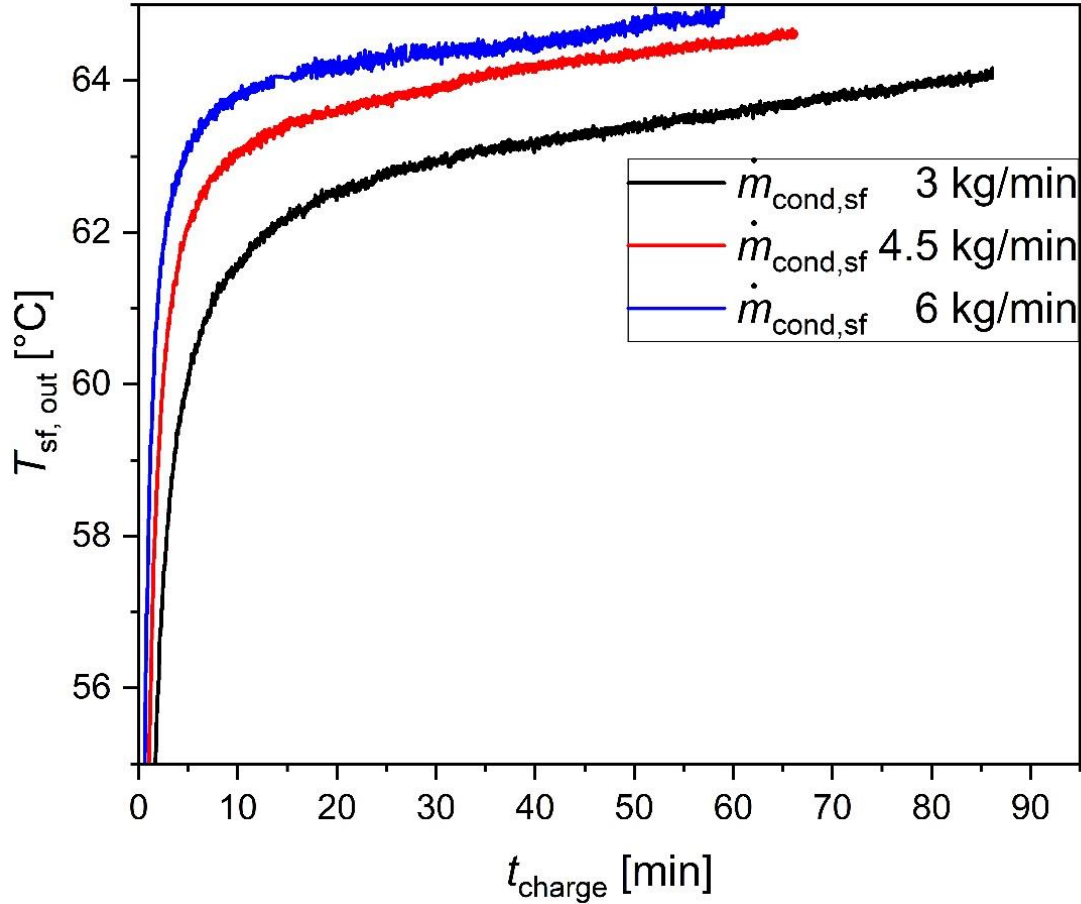
Fig. 5.12 Charging RT60: water outlet temperature $T_{\text{sf,out}}$ for water mass flow rate of 3, 4.5 and 6 kg/min as a function of time with T_{charge} of 65 °C.

The trend of increasing $T_{\text{sf,out}}$ with higher water mass flow rates becomes evident; for example, the outlet temperature exceeds 64 °C after 15 min with a flow rate of 6 kg/min, compared to 45 min with a flow rate of 4.5 kg/min. This suggests that changes in water mass flow rate and outlet temperature directly directly compensate each other, resulting in a constant heat flux. herefore, it appears that heat exchange is limited on the PCM side, possibly due to its low thermal conductivity.

Subsequently, the reduction in charging time with higher water mass flow rates observed in Fig. 5.11 and 5.12 becomes apparent. For instance, the required time decreases from 86 min

for 3 kg/min to approximately 59 min for 6 kg/min. To illustrate this, the required charging time is plotted as a function of the water mass flow rate in Fig. 5.13, supplemented with the required time for 1.5 kg/min.
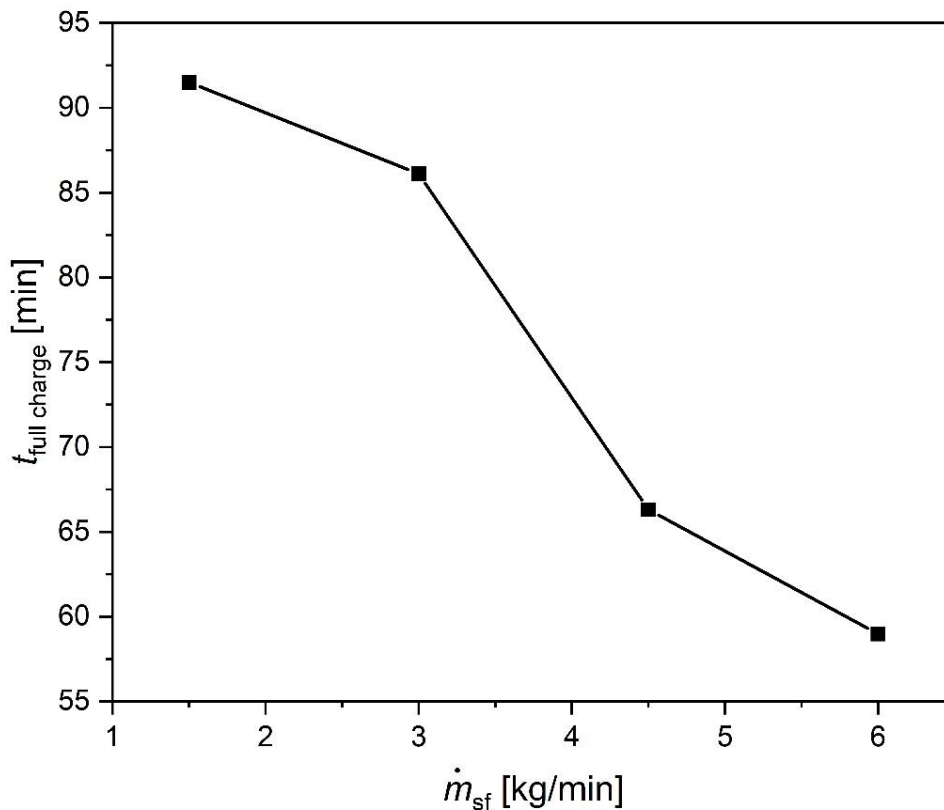
Fig. 5.13 Charging RT60: time until full charge $t_{full\ charge}$ for water mass flow rate of 1.5, 3, 4.5 and 6 kg/min with T_{charge} of 65 °C.

There is an almost linear reduction in charging time with increasing water mass flow rates. This reduction is primarily due to the size of the storage unit. With a storage capacity of approximately 1 MJ, even slight changes in the heat flow rate (20 to 30 W) can noticeably affect the charging time, despite these changes being small compared to the observed total heat flow rate of a few hundred watts. Similar observations were made with RT47, and corresponding diagrams are included in the appendix (Fig. A.3 to A.5). After examining the charging and discharging behaviour of the storage, the last remaining question is the discussion of the advantages arising from the combination of the heat pump and thermal storage test system. Due to the experimental setup with a reservoir for the secondary fluid, the two systems are decoupled from each other for discharging. Additionally, the storage capacity and heat transfer surface area of the thermal storage system are not optimally sized for the heat pump. Nevertheless, an energetic assessment of the combined test setups provides initial insights that can be further investigated in the future.

5.3.3 Charging the storage or regulating the heat pump

In general, heat demand within heating systems fluctuates due to user needs, primarily regulated through adjustments to radiator valves, which in turn affects the water mass flow rate. For instance, valves automatically close once the desired room temperature is reached or when manually adjusted by users. When using a heat pump, these fluctuations affect the required heat flow rate on the secondary side of the condenser to maintain the target outlet temperature, necessitating considerations on system adaptation. Two potential solutions could be the regulation of the heat flow rate provided by the process or using the arising excess water mass flow to charge a thermal storage.

To regulate the provided heat flow rate, adjustments to the working fluid mass flow rate are necessary, achievable through increased throttling via the expansion valve or reduced compressor speed. While both methods decrease the required compressor power, they also result in decreased *COP* at higher temperature levels, as previously discussed in this work. For example, a compressor speed reduction of 30 % at a condenser outlet temperature level of 70 °C led to a *COP* decrease of up to 10 % in chapter 2. Similarly, in chapter 3, reducing the condenser water mass flow rate from 4.5 to 2 kg/min resulted in a *COP* decrease of 37.5 %.

The alternative option of charging a thermal storage with the excess water mass flow requires the split of the water flow after the heat pump. One covering the heat demand, while the other charges the storage, and thus with flexibility for adjustment based on requirements. This approach allows adaptation to changing heat demand without reduced efficiencies due to regulated heat flow rate. Although in this scenario compressor power requirements remain constant and thus higher compared to the first option, the stored energy can be used elsewhere in the building. For instance, it could be used for preheating water for hot water production via an electrical heater. In this context, the exact heat flow rate from the storage becomes less critical, because even if the desired water temperature is not reached by the discharge, the electrical heater power consumption is reduced directly by this heat flow rate.

Consequently, the reduced compressor power and the heat flow rate to the thermal storage should be compared to assess whether a combination of these systems is more advantageous than only regulating the heat pump as they represent the benefits of both options, directly impacting electricity consumption and operational costs.

To investigate this within the test system, operation points for increased throttling (as seen in chapter 3.5.1) and reduced compressor speed (from chapter 2.5), under similar operating

conditions, are examined again. Key values are summarized in Table 5.2, with all operation points maintaining a condenser water inlet temperature of 60 °C, a temperature change of 10 °C, and an evaporator water inlet temperature of 20 °C.

Table 5.2 Condenser mass flow rate $\dot{m}_{cond,sf}$, compressor speed n_{comp}, condenser heat flow rate $\dot{Q}_{cond,sf}$, electrical compressor power $P_{comp,el}$ and the COP_{sf}, for the variations of increased throttling and reduced compressor speed. Condenser water inlet temperature 60 °C, $\Delta T_{cond,sf} = 10$ °C and $T_{evap,sf,in} = 20$ °C for all operation points.

Parameter	Unit	Increased Throttling		Reduced compressor speed	
$\dot{m}_{cond,\ sf}$	kg/min	4.5	2	3.9	2.5
n_{comp}	min^{-1}	1500	1500	1500	1050
$\dot{Q}_{cond,sf}$	kW	3.1	1.4	2.69	1.77
$P_{comp,el}$	kW	1.125	0.804	1.103	0.756
COP_{sf}	-	2.77	1.73	2.44	2.34

For increased throttling of the process, the heat flow rate (thus, the heat demand) decreases from 3.1 to 1.4 kW due to the reduction in water mass flow rate of 2.5 kg/min, which would be the excess water mass flow. The compressor power drops from 1.125 to 0.804 kW, resulting in a decrease in COP_{sf} from 2.77 to 1.73 (37.5 %). For the reduced compressor speed, the change in heat demand is less significant, with $\dot{Q}_{cond,sf}$ dropping from 2.69 to 1.77 kW. However, the required compressor power has a similar reduction, from 1.103 to 0.756 kW, as observed during increased throttling, resulting in a less pronounced decrease in COP_{sf} of 4.1 %.

Thus, the heat flow rate to the storage using the excess water mass flow must be higher than these power reductions for the compressor of 347 W (reduced compressor speed) and 321 W (increased throttling) to be considered more advantageous than regulating the heat pump. To examine this, Fig. 5.14 depicts the heat flow rate to the storage $\dot{Q}_{sf}$, considering a charging temperature of 70 °C and water mass flow rate of 3 kg/min (approximately matching the reduction of $\dot{m}_{cond,sf}$ in Table 5.2 for increased throttling). The compressor power reduction of 321 W for this is represented by a red line in this figure.
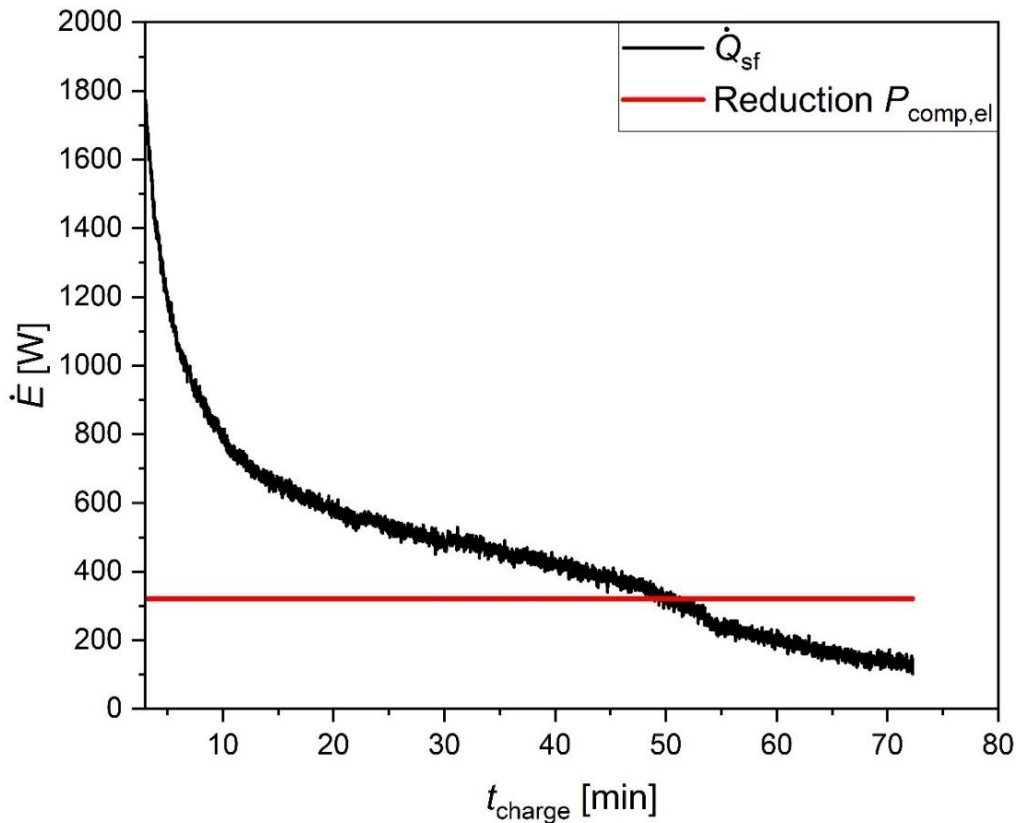
Fig. 5.14 Charging RT60: heat flow rate $\dot{Q}_{sf}$ as a function of time for a water mass flow rate of 3 kg/min with T_{charge} of 70 °C. Reduction of $P_{comp,el}$ for heat pump process with increased throttling shown as red line.

It becomes evident that the heat flow rate exceeds 321 W for approximately 50 min, implying that the storage can be considered fully charged because the phase change is completed and the average temperature within the storage material is around 65 °C. This state of the storage can be compared to the conditions of the previously investigated discharge in Fig. 5.9, where a heat flux of several kW/m^2 indicates a valuable use of the stored energy within this 50 min period. Consequently, the use of the excess water mass flow to charge the thermal storage proves to be more beneficial than regulating the heat pump through increased throttling. This can be assumed for the reduced compressor speed as well, despite the differing excess water mass flow rate (1.4 kg/min instead of 2.5 kg/min), because the decreases in the required compressor power were similar for both variations and varying water mass flow rates had no significant influence on the heat flux to the storage, as observed in chapter 5.3.2.

In conclusion, the investigated heat pump process should be adapted to changing heat demands by operating at full load and being combined with thermal storage. Given that both are non-optimized lab-scale systems, it's reasonable to expect even higher benefits from this combination with improved design in terms of storage capacity and heat transfer area.

Chapter 6

Conclusion and future perspectives

6.1   Conclusion

Throughout this thesis, the primary aim was to expand the understanding of the thermodynamic influences on heat pump systems at residential heating temperature levels, addressing the challenges of such systems in existing buildings. To overcome these, a reasonable *COP* must be achieved at heat sink temperature levels of up to 70 °C, making it feasible to replace conventional heating systems without extensive investments. This would support the increased use of fully electric heating in buildings, consequently reducing CO_2-emissions in this sector.

Therefore, condenser outlet temperatures of 50 and 70 °C were examined experimentally in a compression heat pump bridging the gap between floor heating and conventional house heating. Isobutane and propane were investigated as zeotropic working fluid mixtures, with the aim to use the temperature glide of such mixtures to reduce the exergy destruction in the heat exchangers, thereby improving the process performance dependent of the mixture composition. The *COP* of the test system ranged from 2.54 to 3.73 at 50 °C, indicating suitable efficiencies for a non-optimized system, being within the economically viable *COP* range of around 3. However, at the desired higher temperature of 70 °C, the *COP* only ranged from 1.28 to 2.29, which would be insufficient for practical use. Nonetheless, valuable insights can be drawn from these results for further optimisations and understanding.

In practical applications, the influence of zeotropic working fluid composition on performance is found to be less advantageous than theoretical expectations, particularly at higher temperature levels. Only a maximum *COP* increase of approximately 5 % compared to the pure fluid was achieved, observed at an isobutane mole fraction of 0.25, shifting from the maximum temperature glide occurring at a mole fraction of 0.5. This discrepancy is attributed to the low impact of heat exchangers on total exergy destruction, thereby limiting the potential of zeotropic working fluids to reduce these losses. Moreover, at higher temperature levels, the reduction is more limited as the losses of the compressor increase.

The compressor is the most influential component, having the highest share on total exergy destruction and overall process performance. Consequently, changes in the operating behaviour of the compressor directly affects the entire process. Therefore, composition of the mixture with the maximum *COP* is shifted from the one with the highest temperature glide, as

increased isobutane mole fraction decreases the pressure in the evaporator, resulting in a higher compressor pressure ratio. High pressure ratios increase the forces and losses in the compressor, consequently primarily reducing its electro-mechanical efficiency and subsequently the process performance.

Therefore, the current studies suggest that while the use of zeotropic working fluids is advantageous for all temperature levels, the improvement of the *COP* is moderate for the piston compressor used and decreases at higher temperatures. It could be assumed that the temperature glide could have a higher influence on systems with other compressor types, making them better suited for operation with zeotropic mixtures. Moreover, operating the system within a temperature level suitable for heating systems is generally reasonable; however, there is still potential for improvement, with particular attention to be paid to the influence on the compressor.

Such an influence occurs with changing external parameters through the secondary fluid. Especially the change in heat demand is a crucial parameter that is strongly dependent on the requirements of users in heating systems. In such a system, the inlet temperature and mass flow rate of the condenser are directly affected by this change. To investigate this within realistic ranges for conventional heating systems, mass flow rates up to 6 kg/min and inlet temperatures up to 60 °C were selected in the presented experiments.

There, it is observed that the influence on the process of varying these two parameters is similar, and with changes in heat demand, the heat transfer in the condenser adjusts accordingly. The working fluid mass flow rate must be adapted, which is realised through increased throttling when the compressor speed is fixed (corresponding to on-off operation in practice). Consequently, this affects the pressure and temperature levels, particularly in the evaporator as a phase change occurs therein, making these two interdependent. This leads to an influence on the inlet and outlet pressure of the compressor, and since the inlet pressure is generally low, the change there is significantly more pronounced than in the outlet pressure. Thus, the compressor pressure ratio and subsequently the electro-mechanical efficiency changes.

The influence of the heat source, represented by the evaporator water inlet temperature, is less than for the condenser. Here, the pressure level in the evaporator remains unchanged due to the not affected working fluid mass flow rate. This results in a constant evaporation temperature and unchanging pressure ratio, only resulting in higher superheating of the working fluid and exergy losses.

Based on the results, it is also evident that the sizing of the compressor is crucial for the process, because oversizing would from the beginning lead to a lower utilization and with decreasing working fluid mass flow rates to even lower compressor loads. Such a reduced compressor load is less favourable because the ratio between the power to only drive the compressor and the power transferred to the working fluid decreases. Comparing the *COP* of the process with the ideal *COP* again reveals the importance of the compressor, as the measured performance improves with higher heat demand regardless of the theoretically expected tendencies. For instance, when the mean temperature in the condenser, and thus temperature lift, was increased, the ideal *COP* decreased while the measured one increased due to a higher compressor load.

The results indicate that achieving high utilization of the heat pump for as long as possible is desirable. A thermal energy storage is an option to support this when it is charged by the heat pump at full speed instead of regulating to adjust to lower heat demand. For latent thermal storages, the low thermal conductivity of the PCM limits the heat transfer. Increasing this heat transfer is necessary and was simulated here using fins, a higher thermal conductivity and higher driving temperature gradients as a function of discharge time.

During discharge, the heat flux decreases significantly, especially in the first few minutes. For example, in this work, it drops from several kW/m^2 to a few 100 W/m^2. This can be attributed to the rapid formation of an insulating layer of solidified PCM and discharge of the initial sensitive energy section. After this steep drop, the heat flux declines moderately over time due to the decreasing driving temperature gradient.

For the investigated heat transfer enhancement methods (fins, higher thermal conductivities of the PCM and raising driving temperature gradients), the level of heat flux during operation increased, but the trade-off between these improvements and the disadvantages, for example reduced storage capacity or exergy, must be considered. The novel dimensionless heat flux *M* relates the heat flux to the thermal conductivity, initial driving temperature gradient, and characteristic length and demonstrates that the heat flux does not increase as the changed enhancement method imply.

Furthermore, the combination of different improvement methods is disadvantageous compared with individual ones. For instance, increasing thermal conductivity with higher fin volume fractions in the storage or higher driving temperature gradients is less effective than just the increased thermal conductivity.

Additionally, increasing the driving temperature gradient has a trade-off with exergy and is only valuable up to a certain temperature gradient. Until this, the effect on heat flux and discharge time outweighs the decrease in exergy. For example, this temperature gradient was 6°C in this work, and with higher gradients the exergy drop outweighed the influence on heat flux and discharge time.

If sufficient heat transfer of the latent storage is ensured with those methods, it can be used in combination with a heat pump. For this purpose, charging and discharging at different temperature levels must be investigated, with the influencing factors being the driving temperature gradient and the water mass flow rate.

For lower temperature level of RT47, the simulated results of the varied initial temperature gradient apply to both charging and discharging. Here, with increasing temperature gradient, the *M*-level gets lower and thus the benefit decreases, being more pronounced for charging than for discharging. In contrast, the effect for the higher temperature level with RT60 is inconsistent. During charging, the increase in heat flux is declining, while the *M*-level slightly increases during discharging and thus has a favourable impact. However, with larger increases in temperature difference, this beneficial effect is significantly less pronounced.

Increasing the charging mass flow rate does not lead to an increase in heat flux, as this only affects the water side. The limitation here is on the PCM side due to the low thermal conductivity.

For the combination of a heat pump and a thermal energy storage, it is important to determine when this is more valuable than adjusting the heat pump to the heat demand by by increased throttling or reduced compressor speed. The saved compressor power represents the economic advantage in practice, as this electrical energy typically needs to be purchased externally. If the charging heat flow rate exceeds this saving from the compressor, the combination of both systems can be considered valuable, for example when the storage is used to reduce the required power in hot water production. In this work, even the non-optimal systems prove that this is feasible. With optimisations regarding storage capacity or heat transfer surface area, even better results could be achieved.

In conclusion, based on the results of this study, the use of heat pumps in heating systems with higher residential temperature levels is optimizable but feasible, thus potentially replacing climate harmful ones in existing buildings like gas boilers. This would support the reduction of the CO_2-emissions in the building sector. Additionally, understanding the influences on such a system and optimization capabilities through urgently needed experiments were demonstrated,

whereas charging a thermal energy storage instead of regulating the heat pump appears promising for energy savings. Nevertheless, there are still unanswered research questions that leave room for future investigations.

6.2   Future perspectives

The investigations demonstrated that the secondary fluid parameters have an influence on the performance of the heat pump when the compressor operating conditions are affected. In this study, only a fixed compressor speed was considered for this variation whereas also modulating heat pumps are investigated in literature. Consequently, it remains unclear how the variation of these parameters affects the process when the speed is variable, and a comparison with the regulation via throttling should also be drawn. Since modulating the compressor speed also changes the circulating working fluid flow rate, the pressure and temperature levels in the evaporator could similarly be influenced, resulting in the same influences on the compressor.

Furthermore, the examined system researched only a piston compressor, making further investigations with other compressor types interesting. As the mechanical operation principle differs, the effects on the compressor or their significance on the entire process could also change. Particularly through the examination of the compressors proportion of exergy losses, it should be determined whether shifts in importance for the process occur with different compressor types.

Regarding the investigated latent thermal energy storage, the question remains open why the influence of changing the initial temperature difference is inconsistent at a higher temperature level of RT60. There might be a connection with the respective properties of the forming phase, but this needs further investigation and validation. Insights gained here could potentially be transferred to other PCMs leading to more accurate simulations.

Lastly, the presented considerations on the combination of heat pump and storage are still fundamental and only address the charging. Even though the discharging is notably more situational than charging, it could be included in future investigations at least through assumptions, thus bringing them closer to practice. Besides the necessary inclusion of the economic component of such storage, practical experiments must be conducted to identify and subsequently resolve any challenges in the control of such systems.

Appendix
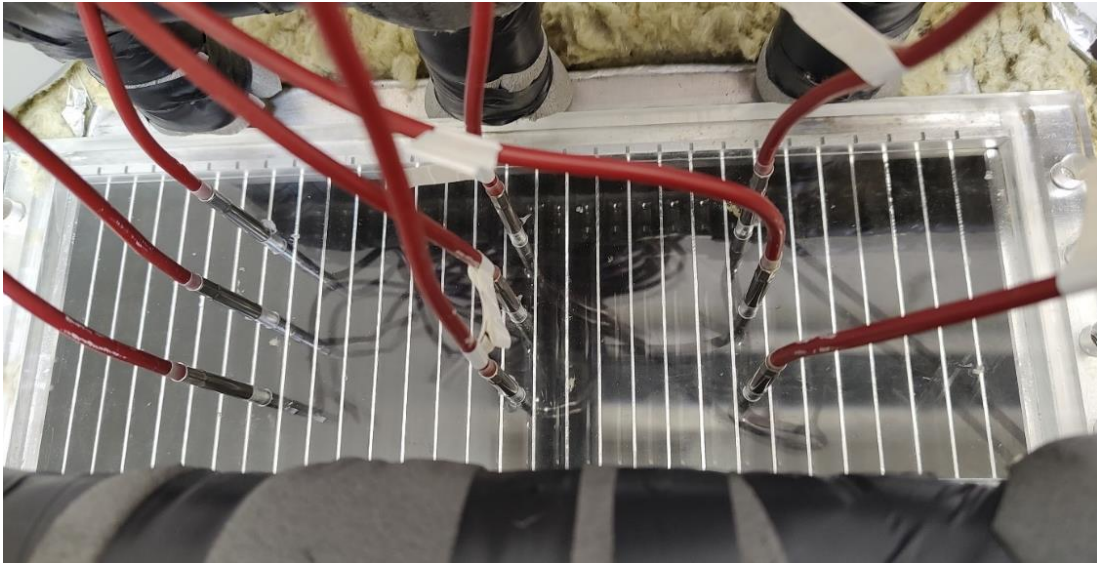
Fig. A.1 Top-down view of the used thermal energy storage system
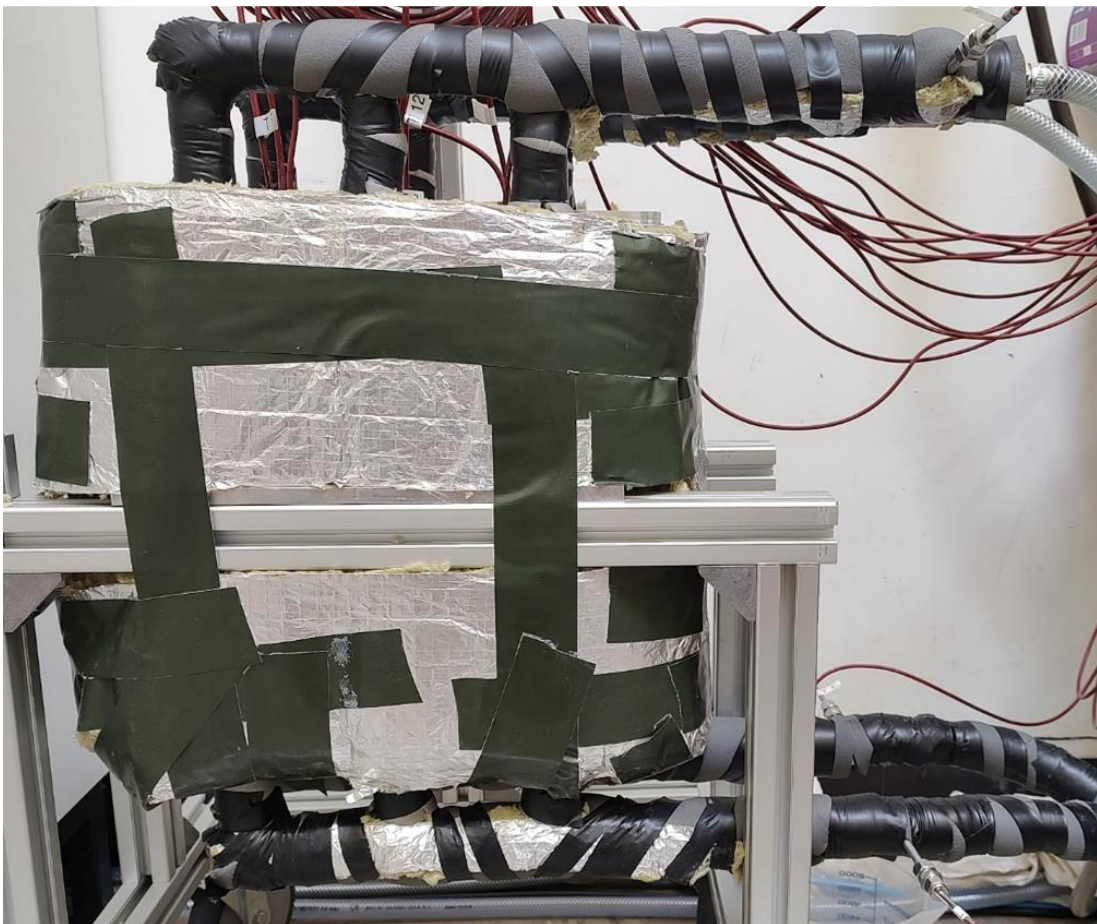
Fig. A.2 Side-view of the used thermal energy storage system
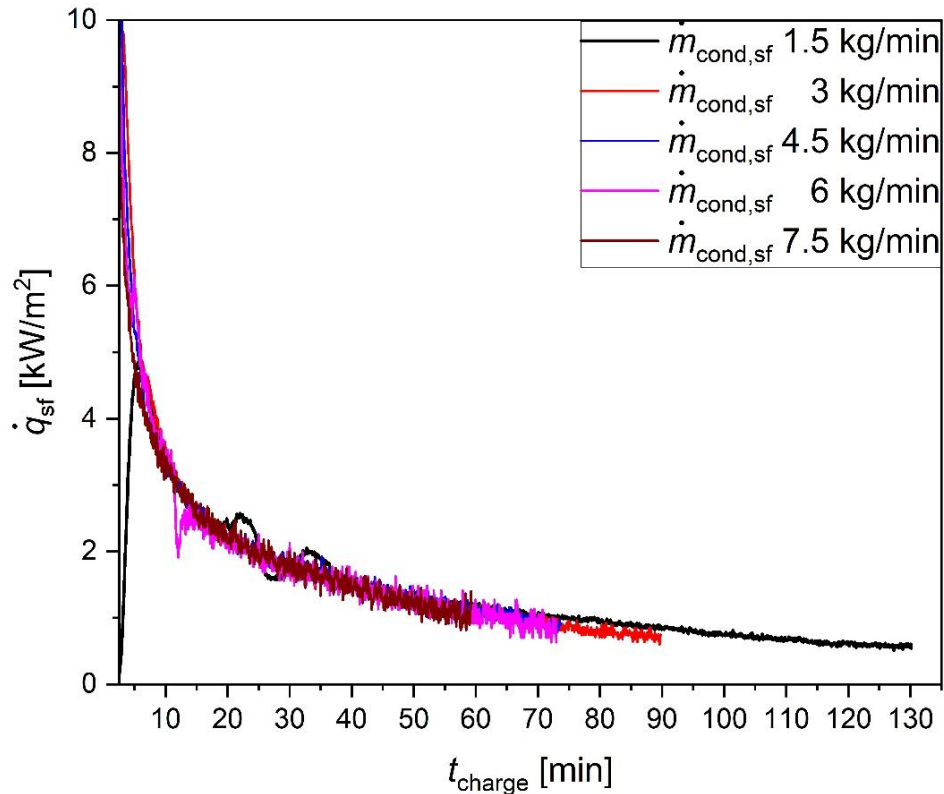
Fig. A.3 Charging RT47: heat flux $\dot{q}_{sf}$ for water mass flow rate of 1.5 to 7.5 kg/min as a function of time with T_{charge} of 52 °C.
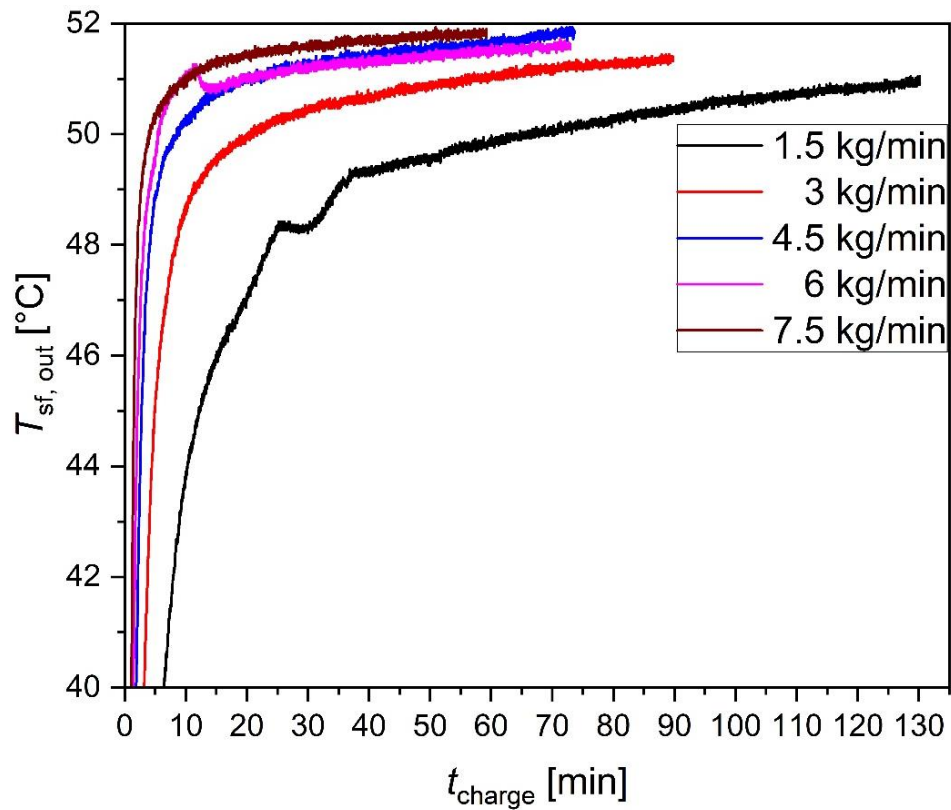
Fig. A.4 Charging RT47: water outlet temperature $T_{sf,out}$ for water mass flow rate of 1.5 to 7.5 kg/min as a function of time with T_{charge} of 52 °C.
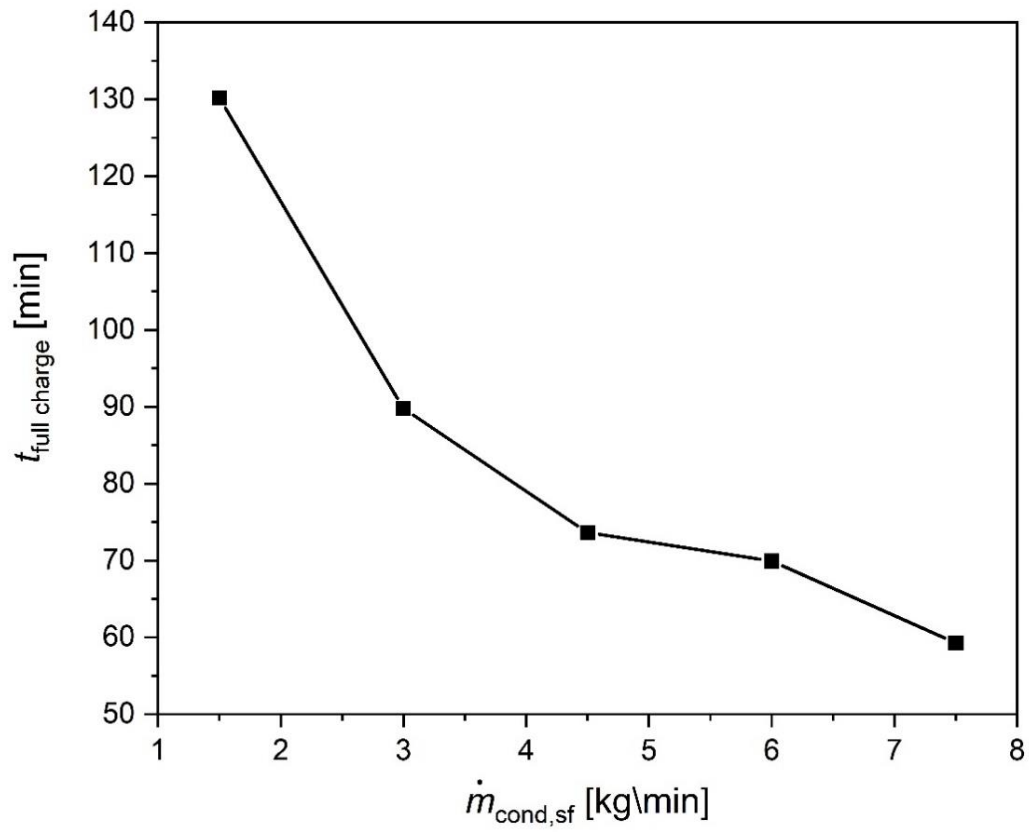
Fig. A.5 Charging RT47: time until full charge $t_{\text{full charge}}$ as a function of water mass flow rate with T_{charge} of 52 °C.

References

[1] ARD. Persönliche Wahrnehmung zum Beitrag des Klimaschutzes. [March 03, 2024]; Available from: https://www.tagesschau.de/multimedia/video/video-1295898.html.

[2] IPCC. Climate Change 2023 Synthesis Report; Available from: https://www.ipcc.ch/report/ar6/syr/.

[3] Henrike Kolletzki. Warum die Appelle nicht ankommen. [March 03, 2024]; Available from: https://www.tagesschau.de/wissen/klima/doku-klimaschutz-100.html.

[4] Oliver Sallet. Expertenrat kritisiert Klimapolitik der Ampel. [March 03, 2024]; Available from: https://www.tagesschau.de/inland/innenpolitik/expertenrat-klima-ampel-regierung-100.html.

[5] Universität Koblenz. Vom Klimastreik zur Klimapolitik. Die gesellschaftliche Unterstützung der „Fridays for Future"-Bewegung und ihrer Ziele; Available from: https://kops.uni-konstanz.de/server/api/core/bitstreams/57d15510-3114-4fdd-9070-4f43ba6d5b43/content.

[6] Bundesregierung Deutschland. Wie steht es um unser Klima? [March 03, 2024]; Available from: https://www.bundesregierung.de/breg-de/schwerpunkte/klimaschutz/bericht-des-weltklimarates-2172568.

[7] Bundesministerium für Wirtschaft und Klimaschutz. Klimaschutzplan 2050. [March 03, 2024]; Available from: https://www.bmwk.de/Redaktion/DE/Publikationen/Industrie/klimaschutzplan-2050.html.

[8] Bundesministerium der Justiz. Gesetz zur Einsparung von Energie und zur Nutzung erneuerbarer Energien zur Wärme- und Kälteerzeugung in Gebäuden. [March 01, 2024]; Available from: https://www.gesetze-im-internet.de/geg/.

[9] EU-Parliament. Schlussfolgerungen zum Thema „Ein klimaresilientes Europa aufbauen – die neue EU-Strategie für die Anpassung an den Klimawandel. [March 01, 2024]; Available from: https://www.consilium.europa.eu/de/press/press-releases/2021/06/10/council-endorses-new-eu-strategy-on-adaptation-to-climate-change/.

[10] EU-Parliament. EU nature restoration regulation: Setting binding targets for healthy ecosystems. [March 01, 2024]; Available from: https://www.europarl.europa.eu/thinktank/de/document/EPRS_BRI(2022)738183.

[11] Bundesministerium für Wirtschaft und Klimaschutz. Klimaschutz in Zahlen. [March 03, 2024]; Available from: https://www.bmwk.de/Redaktion/DE/Publikationen/Klimaschutz/klimaschutz-in-zahlen.pdf?__blob=publicationFile&v=4.pdf%3F__blob%3DpublicationFile%26v%3D4&usg=AOvVaw3DAH1nd6omGHAexNmUUTo6&opi=89978449.

[12] 57 % der im Jahr 2022 gebauten Wohngebäude heizen mit Wärmepumpen. [March 03, 2024]; Available from: https://www.destatis.de/DE/Presse/Pressemitteilungen/2023/06/PD23_N034_31121.html#:~:text=Meist%20handelt%20es%20sich%20auch,als%20primäre%20Heizung%20zum%20Einsatz.

[13] V. Pawlik. Beheizungsstruktur des Wohnungsbestandes in Deutschland in den Jahren 1995 bis 2022. [March 03, 2024]; Available from: https://de.statista.com/statistik/daten/studie/162218/umfrage/beheizungsstruktur-des-wohnbestandes-in-deutschland-seit-1975/.

[14] Focus Online. Wer jetzt eine neue Heizung will, ist mit Gas besser dran als mit Wärmepumpe. [March 05, 2024]; Available from: https://www.focus.de/immobilien/wohnen/wer-jetzt-eine-neue-heizung-will-ist-mit-gas-besser-dran-als-mit-waermepumpe_id_190712012.html.

[15] Tim Stobbe. Wie sinnvoll ist es, vor 2024 noch schnell eine Gasheizung einzubauen? [March 05, 2024]; Available from: https://www.swr.de/swraktuell/rheinland-pfalz/faq-hohe-nachfrage-gasheizung-rlp-leere-lager-100.html.

[16] Tobias Kisling. Wärmepumpen: Dieses große Problem bremst die Heizungswende. [March 05, 2024]; Available from: https://www.morgenpost.de/wirtschaft/article237831359/waermepumpen-deutschland-energiewende-probleme.html.

[17] Statistisches Bundesamt. Gas- und Strompreise für Haushalte im 1. Halbjahr 2023 deutlich gestiegen. [March 05, 2024]; Available from: https://www.destatis.de/DE/Presse/Pressemitteilungen/2023/09/PD23_388_61243.html.

[18] Abbasi MH, Abdullah B, Ahmad MW, Rostami A, Cullen J. Heat transition in the European building sector: Overview of the heat decarbonisation practices through heat pump technology. Sustainable Energy Technologies and Assessments 2021;48:101630.

[19] Alhuyi Nazari M, Rungamornrat J, Prokop L, Blazek V, Misak S, Al-Bahrani M et al. An updated review on integration of solar photovoltaic modules and heat pumps towards decarbonization of buildings. Energy for Sustainable Development 2023;72:230–42.

[20] Borge-Diez D, Icaza D, Trujillo-Cueva DF, Açıkkalp E. Renewable energy driven heat pumps decarbonization potential in existing residential buildings: Roadmap and case study of Spain. Energy 2022;247:123481.

[21] Kim B-J, Kim S, Go M, Joo H-J, Jeong J-W. Applicability performance evaluation of cascade heat pump for building electrification in winter. Journal of Building Engineering 2024;82:108406.

[22] Jarre M, Noussan M, Poggio A, Simonetti M. Opportunities for heat pumps adoption in existing buildings: real-data analysis and numerical simulation. Energy Procedia 2017;134:499–507.

[23] Osterman E, Stritih U. Review on compression heat pump systems with thermal energy storage for heating and cooling of buildings. Journal of Energy Storage 2021;39:102569.

[24] Klein K, Huchtemann K, Müller D. Numerical study on hybrid heat pump systems in existing buildings. Energy and Buildings 2014;69:193–201.

[25] Saffari M, Keogh D, Rosa M de, Finn DP. Technical and economic assessment of a hybrid heat pump system as an energy retrofit measure in a residential building. Energy and Buildings 2023;295:113256.

[26] Vattenfall. Wärmepumpen amortisieren sich innerhalb weniger Jahre. [March 08, 2024]; Available from: https://www.vattenfall.de/infowelt-energie/nachhaltig-heizen/waermepumpe-amortisation#:~:text=Die%20Amortisationszeit%20einer%20Wärmepumpe%20hängt,von%20zehn%20Jahren%20bezahlt%20machen.

[27] Gasag. Amortisation einer Wärmepumpe berechnen – so geht's! [March 08, 2024]; Available from: https://www.gasag.de/magazin/nachhaltig/amortisation-waermepumpe.

[28] Arpagaus C, Bless F, Uhlmann M, Schiffmann J, Bertsch SS. High temperature heat pumps: Market overview, state of the art, research status, refrigerants, and application potentials. Energy 2018;152:985–1010.

[29] Bamigbetan O, Eikevik TM, Nekså P, Bantle M, Schlemminger C. The development of a hydrocarbon high temperature heat pump for waste heat recovery. Energy 2019;173:1141–53.

[30] Cui Q, Wei D, Gao E, Zhang X. Compressor control strategy for CO2 heat pump toward efficient and stable domestic hot water production: An experimental investigation. Thermal Science and Engineering Progress 2023;38:101681.

[31] Leonzio G, Fennell PS, Shah N. Air-source heat pumps for water heating at a high temperature: State of the art. Sustainable Energy Technologies and Assessments 2022;54:102866.

[32] Ganesan P, Eikevik TM, Hamid K, Wang R, Yan H. Thermodynamic analysis of cascade high-temperature heat pump using new natural zeotropic refrigerant mixtures: R744/R600 and R744/R601. International Journal of Refrigeration 2023;154:215–30.

[33] Bagarella G, Lazzarin R, Noro M. Sizing strategy of on–off and modulating heat pump systems based on annual energy analysis. International Journal of Refrigeration 2016;65:183–93.

[34] Pinamonti M, Beausoleil-Morrison I, Prada A, Baggio P. Water-to-water heat pump integration in a solar seasonal storage system for space heating and domestic hot water production of a single-family house in a cold climate. Solar Energy 2021;213:300–11.

[35] Harby K. Hydrocarbons and their mixtures as alternatives to environmental unfriendly halogenated refrigerants: An updated overview. Renewable and Sustainable Energy Reviews 2017;73:1247–64.

[36] Bai M, Zhao L, Zhao R. Review on Applications of Zeotropic Mixtures. J. Therm. Sci. 2022;31(2):285–307.

[37] Bamigbetan O, Eikevik TM, Nekså P, Bantle M. Review of vapour compression heat pumps for high temperature heating using natural working fluids. International Journal of Refrigeration 2017;80:197–211.

[38] Modi A, Haglind F. A review of recent research on the use of zeotropic mixtures in power generation systems. Energy Conversion and Management 2017;138:603–26.

[39] Roskosch D, Venzik V, Schilling J, Bardow A, Atakan B. Beyond Temperature Glide: The Compressor is Key to Realizing Benefits of Zeotropic Mixtures in Heat Pumps. Energy Tech 2021;9(4):2000955.

[40] Valerius Venzik. Experimentelle Untersuchung des Fluideinflusses auf die Thermodynamik der Wärmepumpe: Kohlenwasserstoffe und deren Gemische. Dissertationsschrift. Duisburg; 2019.

[41] Zühlsdorf B, Jensen JK, Cignitti S, Madsen C, Elmegaard B. Analysis of temperature glide matching of heat pumps with zeotropic working fluid mixtures for different temperature glides. Energy 2018;153:650–60.

[42] Liu J, Zhou F, Lyu N, Fan H, Zhang X. Analysis of low GWP ternary zeotropic mixtures applied in high-temperature heat pump for waste heat recovery. Energy Conversion and Management 2023;292:117381.

[43] Liu J, Zhou L, Lin Z, Zhang X. Performance evaluation of low GWP large glide temperature zeotropic mixtures applied in air source heat pump for DHW production. Energy Conversion and Management 2022;274:116457.

[44] Venzik V, Roskosch D, Atakan B. Propene/isobutane mixtures in heat pumps: An experimental investigation. International Journal of Refrigeration 2017;76:84–96.

[45] Bagarella G, Lazzarin RM, Lamanna B. Cycling losses in refrigeration equipment: An experimental evaluation. International Journal of Refrigeration 2013;36(8):2111–8.

[46] Dongellini M, Morini GL. On-off cycling losses of reversible air-to-water heat pump systems as a function of the unit power modulation capacity. Energy Conversion and Management 2019;196:966–78.

[47] Pieper H, Krupenski I, Brix Markussen W, Ommen T, Siirde A, Volkova A. Method of linear approximation of COP for heat pumps and chillers based on thermodynamic modelling and off-design operation. Energy 2021;230:120743.

[48] Xu Z, Li H, Shao S, Xu W, Wang Z, Wang Y et al. A semi-theoretical model for energy efficiency assessment of air source heat pump systems. Energy Conversion and Management 2021;228:113667.

[49] Xu Z, Sun X, Li X, Wang Z, Xu W, Shao S et al. On-off cycling model featured with pattern recognition of air-to-water heat pumps. Applied Thermal Engineering 2021;196:117317.

[50] Aprea C, Mastrullo R, Renno C. Experimental analysis of the scroll compressor performances varying its speed. Applied Thermal Engineering 2006;26(10):983–92.

[51] Boahen S, Anka SK, Ohm T in, Cho Y, Choi JW, Kim H-Y et al. Capacity control of a cascade multi-purpose heat pump using variable speed compressor. Renewable Energy 2023;205:945–55.

[52] Dengiz T, Jochem P, Fichtner W. Demand response with heuristic control strategies for modulating heat pumps. Applied Energy 2019;238:1346–60.

[53] Shao S, Shi W, Li X, Chen H. Performance representation of variable-speed compressor for inverter air conditioners based on experimental data. International Journal of Refrigeration 2004;27(8):805–15.

[54] Madani H, Claesson J, Lundqvist P. Capacity control in ground source heat pump systems. International Journal of Refrigeration 2011;34(6):1338–47.

[55] Madani H, Claesson J, Lundqvist P. Capacity control in ground source heat pump systems part II: Comparative analysis between on/off controlled and variable capacity systems. International Journal of Refrigeration 2011;34(8):1934–42.

[56] Dannemand M, Perers B, Furbo S. Performance of a demonstration solar PVT assisted heat pump system with cold buffer storage and domestic hot water storage tanks. Energy and Buildings 2019;188-189:46–57.

[57] Moreno P, Solé C, Castell A, Cabeza LF. The use of phase change materials in domestic heat pump and air-conditioning systems for short term storage: A review. Renewable and Sustainable Energy Reviews 2014;39:1–13.

[58] Renaldi R, Kiprakis A, Friedrich D. An optimisation framework for thermal energy storage integration in a residential heat pump heating system. Applied Energy 2017;186:520–9.

[59] Yu M, Li S, Zhang X, Zhao Y. Techno-economic analysis of air source heat pump combined with latent thermal energy storage applied for space heating in China. Applied Thermal Engineering 2021;185:116434.

[60] Zhu N, Hu P, Xu L, Jiang Z, Lei F. Recent research and applications of ground source heat pump integrated with thermal energy storage systems: A review. Applied Thermal Engineering 2014;71(1):142–51.

[61] Gu H, Chen Y, Yao X, Huang L, Zou D. Review on heat pump (HP) coupled with phase change material (PCM) for thermal energy storage. Chemical Engineering Journal 2023;455:140701.

[62] Choure BK, Alam T, Kumar R. A review on heat transfer enhancement techniques for PCM based thermal energy storage system. Journal of Energy Storage 2023;72:108161.

[63] Ghosh D, Ghose J, Datta P, Kumari P, Paul S. Strategies for phase change material application in latent heat thermal energy storage enhancement: Status and prospect. Journal of Energy Storage 2022;53:105179.

[64] Al-Maghalseh M, Mahkamov K. Methods of heat transfer intensification in PCM thermal storage systems: Review paper. Renewable and Sustainable Energy Reviews 2018;92:62–94.

[65] Tao YB, He Y-L. A review of phase change material and performance enhancement method for latent heat storage system. Renewable and Sustainable Energy Reviews 2018;93:245–59.

[66] Eslami M, Khosravi F, Fallah Kohan HR. Effects of fin parameters on performance of latent heat thermal energy storage systems: A comprehensive review. Sustainable Energy Technologies and Assessments 2021;47:101449.

[67] Rawat P, Ashwni, Sherwani AF. A numerical study on the impact of fin length arrangement and material on the melting of PCM in a rectangular enclosure. International Journal of Heat and Mass Transfer 2023;205:123932.

[68] Safari V, Abolghasemi H, Kamkari B. Experimental and numerical investigations of thermal performance enhancement in a latent heat storage heat exchanger using bifurcated and straight fins. Renewable Energy 2021;174:102–21.

[69] Shukla A, Kant K, Biwole PH, Pitchumani R, Sharma A. Melting and solidification of a phase change material with constructal tree-shaped fins for thermal energy storage. Journal of Energy Storage 2022;53:105158.

[70] Joybari MM, Haghighat F, Seddegh S, Al-Abidi AA. Heat transfer enhancement of phase change materials by fins under simultaneous charging and discharging. Energy Conversion and Management 2017;152:136–56.

[71] Morimoto T, Kumano H. Flow and heat transfer characteristics of phase change emulsions in a circular tube: Part 1. Laminar flow. International Journal of Heat and Mass Transfer 2018;117:887–95.

[72] Wang F, Fang X, Zhang Z. Preparation of phase change material emulsions with good stability and little supercooling by using a mixed polymeric emulsifier for thermal energy storage. Solar Energy Materials and Solar Cells 2018;176:381–90.

[73] Zhang GH, Zhao CY. Synthesis and characterization of a narrow size distribution nano phase change material emulsion for thermal energy storage. Solar Energy 2017;147:406–13.

[74] Wang F, Zhang C, Liu J, Fang X, Zhang Z. Highly stable graphite nanoparticle-dispersed phase change emulsions with little supercooling and high thermal conductivity for cold energy storage. Applied Energy 2017;188:97–106.

[75] Chen J, Zhang P. Preparation and characterization of nano-sized phase change emulsions as thermal energy storage and transport media. Applied Energy 2017;190:868–79.

[76] Atinafu DG, Dong W, Huang X, Gao H, Wang G. Introduction of organic-organic eutectic PCM in mesoporous N-doped carbons for enhanced thermal conductivity and energy storage capacity. Applied Energy 2018;211:1203–15.

[77] Cheng F, Wen R, Zhang X, Huang Z, Huang Y, Fang M et al. Synthesis and characterization of beeswax-tetradecanol-carbon fiber/expanded perlite form-stable composite phase change material for solar energy storage. Composites Part A: Applied Science and Manufacturing 2018;107:180–8.

[78] Yang J, Tang L-S, Bao R-Y, Bai L, Liu Z-Y, Xie B-H et al. Hybrid network structure of boron nitride and graphene oxide in shape-stabilized composite phase change materials with enhanced thermal conductivity and light-to-electric energy conversion capability. Solar Energy Materials and Solar Cells 2018;174:56–64.

[79] Galazutdinova Y, Vega M, Grágeda M, Cabeza LF, Ushak S. Preparation and characterization of an inorganic magnesium chloride/nitrate/graphite composite for low temperature energy storage. Solar Energy Materials and Solar Cells 2018;175:60–70.

[80] Qian Z, Shen H, Fang X, Fan L, Zhao N, Xu J. Phase change materials of paraffin in h-BN porous scaffolds with enhanced thermal conductivity and form stability. Energy and Buildings 2018;158:1184–8.

[81] Yu Q, Romagnoli A, Al-Duri B, Xie D, Ding Y, Li Y. Heat storage performance analysis and parameter design for encapsulated phase change materials. Energy Conversion and Management 2018;157:619–30.

[82] Wu X, Fan M, Cui S, Tan G, Shen X. Novel Na 2 SO 4 @SiO 2 phase change material with core-shell structures for high temperature thermal storage. Solar Energy Materials and Solar Cells 2018;178:280–8.

[83] Sami S, Sadrameli SM, Etesami N. Thermal properties optimization of microencapsulated a renewable and non-toxic phase change material with a polystyrene shell for thermal energy storage systems. Applied Thermal Engineering 2018;130:1416–24.

[84] Lashgari S, Reza Mahdavian A, Arabi H, Ambrogi V, Marturano V. Preparation of acrylic PCM microcapsules with dual responsivity to temperature and magnetic field changes. European Polymer Journal 2018.

[85] Şahan N, Paksoy H. Novel shapeable phase change material (PCM) composites for thermal energy storage (TES) applications. Solar Energy Materials and Solar Cells 2018;174:380–7.

[86] Quenel J, Anders M, Atakan B. Propane-isobutane mixtures in heat pumps with higher temperature lift: An experimental investigation. Thermal Science and Engineering Progress 2023;42:101907.

[87] Allen L, O'Connell A, Kiermer V. How can we ensure visibility and diversity in research contributions? How the Contributor Role Taxonomy (CRediT) is helping the shift from authorship to contributorship. Learned Publishing 2019;32(1):71–4.

[88] United Nations Environment Programme. Montreal Protocol on Substances that deplete the Ozone Layer; 1987.

[89] Mateu-Royo C, Arpagaus C, Mota-Babiloni A, Navarro-Esbrí J, Bertsch SS. Advanced high temperature heat pump configurations using low GWP refrigerants for industrial waste heat recovery: A comprehensive study. Energy Conversion and Management 2021;229:113752.

[90] Höges C, Roskosch D, Brach J, Vering C, Venzik V, Müller D. Investigation of the Interactions between Refrigerant, Flowsheet, and Compressor in Residential Heat Pumps. Energy Tech 2023;11(2):2201295.

[91] Bamigbetan O, Eikevik TM, Nekså P, Bantle M, Schlemminger C. Theoretical analysis of suitable fluids for high temperature heat pumps up to 125 °C heat delivery. International Journal of Refrigeration 2018;92:185–95.

[92] Chen R, Wu J, Duan J. Performance and refrigerant mass distribution of a R290 split air conditioner with different lubricating oils. Applied Thermal Engineering 2019;162:114225.

[93] Bamigbetan O, Eikevik TM, Nekså P, Bantle M, Schlemminger C. Experimental investigation of a prototype R-600 compressor for high temperature heat pump. Energy 2019;169:730–8.

[94] Guo H, Gong M, Qin X. Performance analysis of a modified subcritical zeotropic mixture recuperative high-temperature heat pump. Applied Energy 2019;237:338–52.

[95] Zhang J, Wang RZ, Wu JY. System optimization and experimental research on air source heat pump water heater. Applied Thermal Engineering 2007;27(5-6):1029–35.

[96] Chaichana C, Aye L, Charters W. Natural working fluids for solar-boosted heat pumps. International Journal of Refrigeration 2003;26(6):637–43.

[97] Chang Y, Kim M, Ro S. Performance and heat transfer characteristics of hydrocarbon refrigerants in a heat pump system. International Journal of Refrigeration 2000;23(3):232–42.

[98] Park K-J, Seo T, Jung D. Performance of alternative refrigerants for residential air-conditioning applications. Applied Energy 2007;84(10):985–91.

[99] Mota-Babiloni A, Mateu-Royo C, Navarro-Esbrí J, Molés F, Amat-Albuixech M, Barragán-Cervera Á. Optimisation of high-temperature heat pump cascades with internal heat exchangers using refrigerants with low global warming potential. Energy 2018;165:1248–58.

[100] Zühlsdorf B, Meesenburg W, Ommen TS, Thorsen JE, Markussen WB, Elmegaard B. Improving the performance of booster heat pumps using zeotropic mixtures. Energy 2018;154:390–402.

[101] Eric W. Lemmon, Marcia L. Huber, Mark O. McLinden. NIST Standard Reference Database 23: NIST Reference Fluid Thermodynamic and Transport Properties - REFPROP Version 9.1; 2013.

[102] Y. Sumida, T. Okazaki, T. Kasai, Y. Ueno. Development of the Circulating Composition Sensing Circuit for a Multiple Split Type Air Conditioner with R-407C. [June 22, 2023]; Available from: https://docs.lib.purdue.edu/cgi/viewcontent.cgi?article=1387&context=iracc.

[103] Johansson A, Lundqvist P. A method to estimate the circulated composition in refrigeration and heat pump systems using zeotropic refrigerant mixtures. International Journal of Refrigeration 2001;24(8):798–808.

[104] Kunz O. The GERG-2004 wide-range equation of state for natural gases and other mixtures. Düsseldorf: VDI-Verl; 2007.

[105] Roskosch D, Venzik V, Atakan B. Thermodynamic model for reciprocating compressors with the focus on fluid dependent efficiencies. International Journal of Refrigeration 2017;84:104–16.

[106] Kristensen AS, Sørensen EK, Madsen C, Kristófersson J, Forooghi P. Performance analysis of heat pumps with zeotropic mixtures at different load conditions. International Journal of Refrigeration 2023;145:264–75.

[107] Abedini H, Vieren E, Demeester T, Beyne W, Lecompte S, Quoilin S et al. A comprehensive analysis of binary mixtures as working fluid in high temperature heat pumps. Energy Conversion and Management 2023;277:116652.

[108] Fernández-Moreno A, Mota-Babiloni A, Giménez-Prades P, Navarro-Esbrí J. Optimal refrigerant mixture in single-stage high-temperature heat pumps based on a multiparameter evaluation. Sustainable Energy Technologies and Assessments 2022;52:101989.

[109] Eppinger B, Zigan L, Karl J, Will S. Pumped thermal energy storage with heat pump-ORC-systems: Comparison of latent and sensible thermal storages for various fluids. Applied Energy 2020;280:115940.

[110] Cao Y, Dhahad HA, Mohamed AM, Anqi AE. Thermo-economic investigation and multi-objective optimization of a novel enhanced heat pump system with zeotropic mixture using NSGA-II. Applied Thermal Engineering 2021;194:116374.

[111] Guth T, Atakan B. Semi-empirical model of a variable speed scroll compressor for R-290 with the focus on compressor efficiencies and transferability. International Journal of Refrigeration 2023;146:483–99.

[112] Li C, Jiang P, Zhu Y. Optimal compressor discharge pressure and performance characteristics of transcritical CO2 heat pump for crude oil heating. International Journal of Refrigeration 2022;144:99–107.

[113] Ishaque S, Siddiqui MIH, Kim M-H. Effect of heat exchanger design on seasonal performance of heat pump systems. International Journal of Heat and Mass Transfer 2020;151:119404.

[114] Sim J, Lee H, Jeong JH. Optimal design of variable-path heat exchanger for energy efficiency improvement of air-source heat pump system. Applied Energy 2021;290:116741.

[115] Diniz HAG, Resende SIdM, Luz AP, Machado L, Oliveira RN de. Energetic, exergetic, environmental and economic (4E) analysis of a direct-expansion solar-assisted heat pump with low GWP refrigerant. International Journal of Refrigeration 2023;154:84–98.

[116] Guth T, Atakan B, Schädlich S. A validated model for variable-speed multi-chillers to assess different operation modes. International Journal of Refrigeration 2024.

[117] Huang Y, Chen J, Chen Y, Luo X, Liang Y, He J et al. Performance explorations of a novel high temperature heat pump with multi-adjusted compositions of zeotropic mixture. Applied Thermal Engineering 2023;235:121409.

[118] Kosmadakis G, Meramveliotakis G, Bakalis P, Neofytou P. Waste heat upgrading with high-temperature heat pumps for assisting steam generation in ships: Performance, cost and emissions benefits. Applied Thermal Engineering 2024;236:121890.

[119] Vieren E, Demeester T, Beyne W, Arteconi A, Paepe M de, Lecompte S. The thermodynamic potential of high-temperature transcritical heat pump cycles for industrial processes with large temperature glides. Applied Thermal Engineering 2023;234:121197.

[120] Zhao X, Huang S, Xie N, Wang L, Li H. Simultaneous optimization of working fluid and temperature matching for heat pump assisted geothermal cascade heating system. Case Studies in Thermal Engineering 2023;41:102685.

[121] Quenel J, Atakan B. Heat flux in latent thermal energy storage systems: the influence of fins, thermal conductivity and driving temperature difference. Heat Mass Transfer 2022;58(12):2085–96.

[122] Guyer JE, Wheeler D, Warren JA. FiPy: Partial Differential Equations with Python. Comput. Sci. Eng. 2009;11(3):6–15.

[123] Hübner S, Eck M, Stiller C, Seitz M. Techno-economic heat transfer optimization of large scale latent heat energy storage systems in solar thermal power plants. Applied Thermal Engineering 2016;98:483–91.

[124] Manfrida G, Secchi R, Stańczyk K. Modelling and simulation of phase change material latent heat storages applied to a solar-powered Organic Rankine Cycle. Applied Energy 2016;179:378–88.

[125] Delgado JM, Martinho JC, Vaz Sá A, Guimarães AS, Abrantes V. Thermal Energy Storage with Phase Change Materials: A Literature Review of Applications for Buildings Materials. Cham: Springer International Publishing; 2019.

[126] Tyagi VV, Kaushik SC, Tyagi SK, Akiyama T. Development of phase change materials based microencapsulated technology for buildings: A review. Renewable and Sustainable Energy Reviews 2011;15(2):1373–91.

[127] Kenisarin M, Mahkamov K. Passive thermal control in residential buildings using phase change materials. Renewable and Sustainable Energy Reviews 2016;55:371–98.

[128] Khouya A, Draoui A. Computational drying model for solar kiln with latent heat energy storage: Case studies of thermal application. Renewable Energy 2019;130:796–813.

[129] Merlin K, Soto J, Delaunay D, Traonvouez L. Industrial waste heat recovery using an enhanced conductivity latent heat thermal energy storage. Applied Energy 2016;183:491–503.

[130] Ren Q, Guo P, Zhu J. Thermal management of electronic devices using pin-fin based cascade microencapsulated PCM/expanded graphite composite. International Journal of Heat and Mass Transfer 2020;149:119199.

[131] Li G. Energy and exergy performance assessments for latent heat thermal energy storage systems. Renewable and Sustainable Energy Reviews 2015;51:926–54.

[132] Reddy KS, Mudgal V, Mallick TK. Review of latent heat thermal energy storage for improved material stability and effective load management. Journal of Energy Storage 2018;15:205–27.

[133] Kazemi M, Hosseini MJ, Ranjbar AA, Bahrampoury R. Improvement of longitudinal fins configuration in latent heat storage systems. Renewable Energy 2018;116:447–57.

[134] Murray RE, Groulx D. Experimental study of the phase change and energy characteristics inside a cylindrical latent heat energy storage system: Part 1 consecutive charging and discharging. Renewable Energy 2014;62:571–81.

[135] Biwole PH, Groulx D, Souayfane F, Chiu T. Influence of fin size and distribution on solid-liquid phase change in a rectangular enclosure. International Journal of Thermal Sciences 2018;124:433–46.

[136] Kamkari B, Shokouhmand H. Experimental investigation of phase change material melting in rectangular enclosures with horizontal partial fins. International Journal of Heat and Mass Transfer 2014;78:839–51.

[137] Liu C, Groulx D. Experimental study of the phase change heat transfer inside a horizontal cylindrical latent heat energy storage system. International Journal of Thermal Sciences 2014;82:100–10.

[138] Kim MH, Duong XQ, Chung JD. Performance enhancement of fin attached ice-on-coil type thermal storage tank for different fin orientations using constrained and unconstrained simulations. Heat Mass Transfer 2017;53(3):1005–15.

[139] Abdulateef AM, Abdulateef J, Mat S, Sopian K, Elhub B, Mussa MA. Experimental and numerical study of solidifying phase-change material in a triplex-tube heat exchanger with longitudinal/triangular fins. International Communications in Heat and Mass Transfer 2018;90:73–84.

[140] Pizzolato A, Sharma A, Maute K, Sciacovelli A, Verda V. Design of effective fins for fast PCM melting and solidification in shell-and-tube latent heat thermal energy storage through topology optimization. Applied Energy 2017;208:210–27.

[141] Mahdi JM, Nsofor EC. Solidification enhancement of PCM in a triplex-tube thermal energy storage system with nanoparticles and fins. Applied Energy 2018;211:975–86.

[142] Al-Jethelah MS, Tasnim SH, Mahmud S, Dutta A. Melting of nano-phase change material inside a porous enclosure. International Journal of Heat and Mass Transfer 2016;102:773–87.

[143] Tang Y, Di Su, Huang X, Alva G, Liu L, Fang G. Synthesis and thermal properties of the MA/HDPE composites with nano-additives as form-stable PCM with improved thermal conductivity. Applied Energy 2016;180:116–29.

[144] Colla L, Fedele L, Mancin S, Danza L, Manca O. Nano-PCMs for enhanced energy storage and passive cooling applications. Applied Thermal Engineering 2017;110:584–9.

[145] Tasnim SH, Hossain R, Mahmud S, Dutta A. Convection effect on the melting process of nano-PCM inside porous enclosure. International Journal of Heat and Mass Transfer 2015;85:206–20.

[146] Elbahjaoui R, El Qarnia H, El Ganaoui M. Numerical study of the melting of Nano-PCM in a rectangular storage unit heated by upward heat transfer fluid. Energy Procedia 2017;139:86–91.

[147] Sami S, Etesami N. Improving thermal characteristics and stability of phase change material containing TiO 2 nanoparticles after thermal cycles for energy storage. Applied Thermal Engineering 2017;124:346–52.

[148] Kohyani MT, Ghasemi B, Raisi A, Aminossadati SM. Melting of cyclohexane–Cu nano-phase change material (nano-PCM) in porous medium under magnetic field. Journal of the Taiwan Institute of Chemical Engineers 2017;77:142–51.

[149] Saeed RM, Schlegel JP, Castano C, Sawafta R. Preparation and enhanced thermal performance of novel (solid to gel) form-stable eutectic PCM modified by nano-graphene platelets. Journal of Energy Storage 2018;15:91–102.

[150] Lamberg P, Lehtiniemi R, Henell A-M. Numerical and experimental investigation of melting and freezing processes in phase change material storage. International Journal of Thermal Sciences 2004;43(3):277–87.

[151] Bauer T. Approximate analytical solutions for the solidification of PCMs in fin geometries using effective thermophysical properties. International Journal of Heat and Mass Transfer 2011;54(23-24):4923–30.

[152] Gunjo DG, Jena SR, Mahanta P, Robi PS. Melting enhancement of a latent heat storage with dispersed Cu, CuO and Al 2 O 3 nanoparticles for solar thermal application. Renewable Energy 2018;121:652–65.

[153] Rubitherm. Technical Datasheet RT44 HC; Available from: https://www.rubitherm.eu/media/products/datasheets/Techdata_-RT44HC_DE_09102020.PDF.

[154] VDI-Wärmeatlas: Mit 320 Tabellen. 11th ed. Berlin: Springer Vieweg; 2013.

[155] Baehr HD, Stephan K. Wärme- und Stoffübertragung. 9th ed. Berlin, Heidelberg: Springer Vieweg; 2016.

[156] Rubitherm. Technical Datasheet RT47. [February 07, 2024]; Available from: https://www.rubitherm.eu/media/products/datasheets/Techdata_-RT47_EN_09102020.PDF.

[157] Rubitherm. Technical Datasheet RT60. [February 07, 2024]; Available from: https://www.rubitherm.eu/media/products/datasheets/Techdata_-RT60_EN_09102020.PDF.